CONTRIBUTIONS TO GLOBAL AND REGIONAL RADIONAVIGATION ROBUSTNESS

A Dissertation

Presented to the Faculty of the Graduate School

of Cornell University

in Partial Fulfillment of the Requirements for the Degree of

Doctor of Philosophy

by

Tunc Ertan

December 2017

© 2017 Tunc Ertan

ALL RIGHTS RESERVED

CONTRIBUTIONS TO GLOBAL AND REGIONAL RADIONAVIGATION ROBUSTNESS

Tunc Ertan, Ph.D.

Cornell University 2017

Three research efforts are presented which develop systems to increase radionavigation robustness. These three efforts constitute stand-alone chapters. The first of these describes an alternative position and navigation system that estimates absolute aircraft position and velocity based on time-series of accumulated delta range measurements from Distance Measuring Equipment (DME) ground transponders. The second presents a method to mitigate multipath in GNSS signals that rely on an antenna array. The developed method can be used as part of an anti-spoofing system. The third discusses a novel radionavigation system based on passive reflectors in orbit and ground transmitters. The proposed system's ability to change the signal broadcast relatively easily in case the system comes under attack provides a robust navigation system.

BIOGRAPHICAL SKETCH

Tunc Ertan was born in Eskisehir, Turkey on May 26, 1989. He graduated from Robert College in Istanbul, Turkey. He received a Bachelor of Science degree from Cornell University, majoring in Mechanical Engineering. He started his Ph.D program in Mechanical Engineering in the fall of 2012 under the guidance of Professor Mark L. Psiaki.

For my dear parents Erdinç and Engin, and my loving sister Çağla who have been extremely supportive of me, despite thousands of miles separating us. Sizsiz yapamazdım.

ACKNOWLEDGEMENTS

Many thanks to my advisors, Professors Mark L. Psiaki, Mark Campbell, and David L. Hysell.

TABLE OF CONTENTS

LIST OF TABLES

LIST OF FIGURES

CHAPTER 1

INTRODUCTION

Global Navigation Satellite Systems (GNSS) such as the Global Positioning System (GPS) have attained widespread use for Position, Navigation, and Timing (PNT) services. Attacks against GPS users in the form of jammers have increasingly been noted as a result of this widespread use. Another threat is that of spoofers. Although no "in the wild" spoofing attacks have been verified, one has been claimed [1], and several controlled spoofing tests have produced alarming results [2–4]. In recent years, the vulnerabilities of GPS have become a challenge, and navigation robustness has moved to the center of discussion.

In light of this challenge, proposed solutions can be seperated into two categories. The first category of solutions seeks to mitigate the effects of the vulnerabilities of GPS on navigation by designing methods that can detect and remove the effects of attackers on users. The second category of solutions involves abandoning the use of GPS in favor of alternative PNT services.

A novel method that estimates absolute aircraft position and velocity has been analyzed as a possible alternative PNT method when operating aircraft over the Continental US (CONUS) and similar areas. This method is based on time-series of accumulated delta range measurements from Distance Measuring Equipment (DME) ground transponders. This method is designed to be implementable with the current infrastructure. The design of an Extended Kalman filter that processes the measurements for the proposed method and the likely filter performance in representative scenarios are described in detail in Chapter 2.

A method that detects multipath in GNSS signals by considering accumulation-type

measurements in an antenna array has been developed as part of a method that seeks to counteract the effects of spoofers to provide robust GNSS PNT services. The system mitigates multipath effects by exploiting direction-of-arrival and polarization difference in the multipath. A novel test statistic is developed to determine the number of multipath signals present. The design of a batch filter that estimates signal characteristics and the filter's performance in truth-model simulations are discussed in Chapter 3. Though the method is intended to mitigate multipath, it can also be used to detect a spoofer and mitigate its effects on a user receiver.

An alternative radionavigation system based on passive reflector satellites and ground transmitters has been developed as another possible alternative PNT method with the potential for global operation. The goal is to develop an alternate to GPS that is adaptable to attacks. The designed system's use of ground transmitters in place of satellite transmitters enables rapid change of the broadcast signal in the event of a system compromise. Such a system has the potential to re-secure its signals in days or even hours or minutes. Current GNSS constellations, by contrast, require a decade or more to adapt their signals because existing satellites must be replaced with new ones in order to broadcast signals with new characteristics. The design specifics of the system and performance metrics are presented in Chapter 4.

The systems described in Chapter 2 and 4 belong to the group of proposed solutions to GPS vulnerability that rely on designing alternative systems. The method presented in Chapter 3, on the other hand, represents a mitigation approach.

CHAPTER 2

ALTERNATIVE POSITION AND NAVIGATION BASED ON DME ACCUMULATED DELTA RANGE

2.1 Abstract

A method that estimates absolute aircraft position and velocity based on time-series of accumulated delta range measurements from Distance Measuring Equipment (DME) ground transponders is analyzed. This method provides an Alternative Position and Navigation – but not quite Timing – (APNT) system for use in airplanes as a back-up to a Global Navigation Satellite System (GNSS) such as GPS. The results show that a steady-state accuracy level better than 0.025 nautical miles is achievable for the whole duration of a simulated flight trajectory with the tracking of 4 DME ground stations when aided by sporadic absolute range measurements. The system with only accumulated delta range measurements is challenged in low speed cases; however, this system exhibits convergence times of about 340 and 130 seconds, respectively, for an aircraft speed of 200 and 500 kts when tracking 5 DME ground stations.

2.2 Introduction

Position, Navigation, and Timing (PNT) services are vital to many essential applications worldwide. In particular, the Global Positioning System (GPS) has been increasingly adopted into civilian use, and GPS will become the primary, and increasingly the only, system supporting navigation services for the U.S. civilian airspace. However, GPS has been shown to be vulnerable to spoofing and jamming in recent years. In light

of the vulnerability of GPS, the Federal Aviation Administration (FAA) has started an Alternative Position, Navigation, and Timing (APNT) program that seeks to provide back-up navigation services in the National Airspace even in the event of GPS service degradation or outage [5].

Enhanced use of the existing Distance Measuring Equipment (DME) ground transponder network has been proposed for this purpose. DME determines the slant range between an aircraft and the ground transponder by round-trip two-way ranging. The total time from an aircraft radio interrogation to the arrival of a ground-transponder reply is measured and converted to a distance measurement. This process is visualized in Fig. 2.1 by the top diagram, in which the blue arrow represents the aircraft interrogation, and the red arrow stands for the transponder reply.

One of the proposed APNT methods is active aircraft interrogation of multiple DME transponders to achieve aircraft position. In this method, the aircraft interrogates all the DME transponders in view, and its flight management system filters the multiple range data to solve for its position. The use of existing infrastructure is the main attraction of this method. Because a DME transponder has to respond to interrogation by multiple aircraft in order for all of them to get a range measurement, this method has a system capacity limited by the response rate of the DME transponder and the fact that the DME transponder can only reply to one interrogation at a time. Therefore, the effective number of available ground stations at an instant is reduced from its theoretical maximum of the total number of ground stations in view.

A second proposed method is DME-based passive ranging [6]. This method replaces the active interrogation of the previous method with on-ground pseudo interrogators. Each DME ground station transmits a response to its pseudo interrogator as if being interrogated by an aircraft. Unlike in the previous method, the DME response is usable

by all aircraft in view because the pseudo interrogator sets up a pseudorandom sequence that can be used to identify it and to time its transmission and arrival times. This eliminates one of the main problems with the previous method, that of system overload. Moreover, the power consumption on the aircraft is significantly reduced due to the passivity of the aircraft part of the system. However, since the method relies on calculating a pseudorange from the response using the broadcast time, it requires good absolute time at the pseudo interrogator. In addition, unlike in the previous method, an upgrade to the existing DME network in the form of the pseudo interrogators is needed. The DME-based passive ranging method is visualized in Fig. 2.1 by the middle diagram, in which the aircraft interrogation is replaced by the blue arrow on the left, representing the pseudo interrogation.

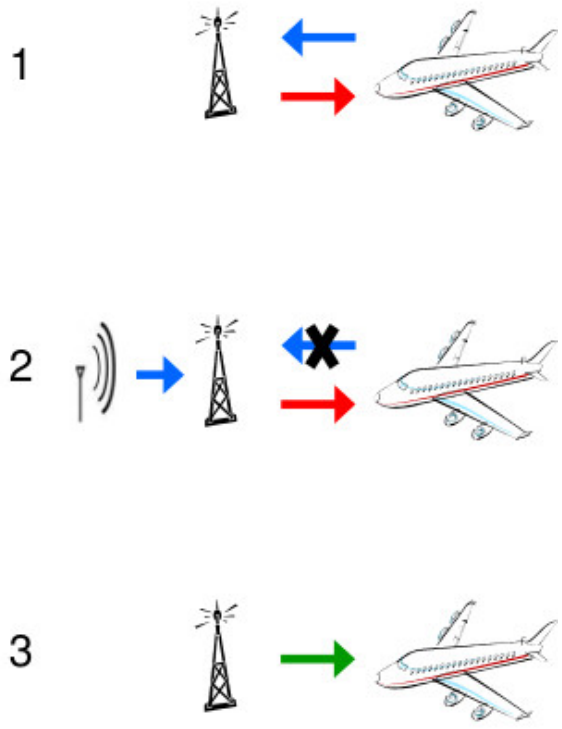

Figure 2.1: *Proposed APNT methods using DME interrogation and response absolute ranging (top), DME pseudo-interrogation and aircraft passive ranging (middle), and DME passive accumulated delta ranging (bottom)*

This paper presents a new method to estimate absolute aircraft position and velocity.

The proposed method is based on accumulated delta range measurements from DME ground transponders using existing DME "heartbeat" signals. The accumulated delta range measurements are provided by radio-navigation carrier phase observables of the "heartbeat" broadcasts.

A DME transponder broadcasts a ground-transponder reply in the form of a pulse pair in response to an aircraft radio interrogation, as discussed for the first of the proposed APNT methods. However, a DME transponder naturally broadcasts its "heartbeat" signals even without an aircraft interrogation. In the absence of aircraft radio interrogations or when the interrogation rate is low, a rate of 700 pulses per minute is maintained by a DME transponder by randomly transmitting pulse pairs [7]. Phase continuity of these signals, despite their on/off pulsed nature, is required for this method to work. The underlying carrier phase has been shown to be continuous for most transponders in service [8]. The intermittent nature of the "heartbeat" signals requires a special phase lock loop (PLL) to extract this continuous carrier phase. Using such a special PLL, it has been demonstrated that the carrier phase is trackable to $0.02m$ standard deviation accuracy or better, as though it is continuously available [9]. DME carrier phase has been used to smooth absolute range measurements and to provide position continuity during outage gaps of absolute range availability [10]. The new concept presented in this paper is the determination of absolute information from the accumulated delta range relative motion data.

This new APNT method has two advantages. First, it requires few upgrades to DME ground transponders, if any. The only needed features are phase coherency, as discussed above, and an adequate frequency standard. Unlike the DME-based passive ranging method, the proposed method requires no transfer of absolute time at the transponders. The second advantage of the method is the complete passivity of the system. The lack

of DME interrogation prevents DME transponder overload with increasing air traffic. Furthermore, this passivity allows flight units to rely only on a DME-band receiver, as opposed to an active DME interrogation unit, and the accompanying reduction in required power makes this method more practical for small aircraft.

The bottom diagram in Fig. 2.1 demonstrates the lack of DME interrogation by an absence of the blue arrow. The reliance on the ground transponder "heartbeat" signals is represented by the green arrow.

The proposed method is similar to Doppler-based radio-navigation, especially as used for spacecraft orbit determination. The shapes of the accumulated delta range time histories are dependent on the absolute aircraft position and motion relative to the DME ground transponder. As such, this method requires the aircraft to have non-zero velocity. Furthermore, the availability of a pressure altimeter is assumed in order to ensure vertical position observability. With sufficient geometric diversity in the DME sources, a full navigation solution can be obtained through proper filtering of a time series of accumulated delta range data.

A modified version of the proposed method incorporates sporadic use of active aircraft interrogation in addition to the use of accumulated delta range measurements. The round-trip two-way ranging obtained by active interrogation of DME transponders provides absolute slant range measurements that alleviate filter convergence issues encountered when using only accumulated delta range measurements. The navigation solution between the absolute range measurements is still obtained through the accumulated delta range measurements and the pressure altimeter altitude measurement. This modified version preserves two of the three advantages of the new APNT method described above. First, the existing infrastructure is already capable of active interrogation, so this version of the proposed method still requires no upgrade of the current infrastructure.

Second, the infrequent interrogation of the DME transponders prevents a system overload that would occur in the first proposed APNT method that relies only on absolute range measurements obtained via active interrogation. However, this alternative to the new system does not preserve the advantage of having a fully passive system that can be smaller and require less power than an active DME transponder.

This paper makes 2 significant contributions to the subject of APNT. First, it develops an Extended Kalman filter that processes the accumulated delta-range and pressure altimeter measurements in order to estimate absolute aircraft position and velocity. No known prior result demonstrates absolute position observability from measurements of incremental range changes. The particular Extended Kalman filter happens to be in Square Root Information filter (SRIF) form, but the particular choice of Extended Kalman filter implementation is a matter of preference, rather than a significant contribution. Second, this paper applies its filter to the outputs of the truth-model simulation in order to demonstrate absolute position observability and to deduce likely filter convergence times and steady-state accuracies for representative scenarios. Specifically, it investigates the convergence time to a 0.025 nm error standard deviation in latitude and longitude in order to determine whether the proposed method merits further study. The accuracy goal of 0.025 nm is derived from the APNT surveillance requirement NACp-8 (0.05 nm 95% accuracy) described in the APNT CONOPS [11].

The remainder of the paper is organized as follows. The second section provides a detailed description of the dynamics and measurement model of the aircraft and the DME accumulated delta range measurement for use in this paper's filter and truth-model simulation. The third section describes this paper's extended Kalman filter. The fourth section explains the functioning of the truth-model simulation. The fifth section presents the results of applying the Kalman filter to the simulated data. The paper's summary and

conclusions are presented in its sixth section.

2.3 Aircraft and DME Model

This section develops the state vector, the dynamics model, and the measurement model that are used by the truth-model simulation and by the corresponding filter.

2.3.1 State Vector

Given N DME ground stations in view, the system state vector that is used by the truth-model simulation and by the filter has dimension $(11+2N)$. It is

$$\underline{x} = \begin{bmatrix} \phi & \lambda & h & \dot{\phi} & \dot{\lambda} & \dot{h} & \ddot{\phi} & \ddot{\lambda} & \ddot{h} & \dot{\delta}_R & \Delta h_{bias} & \dot{\delta}_1 & \dots & \dot{\delta}_N & \beta_1 & \dots & \beta_N \end{bmatrix}^T \tag{2.1}$$

This filter state vector includes 9 aircraft flight states, the aircraft DME receiver's clock frequency offset, and the pressure altimeter bias. The state vector also includes a transmitter clock frequency offset and an accumulated delta range bias for each DME ground station in view. The need for these latter states will be explained in the measurement model section.

The first 9 states represent the aircraft flight information. The quantities ϕ, λ, and h are, respectively, the aircraft position states in latitude, longitude, and altitude, in the WGS-84 coordinate system. The corresponding rates $\dot{\phi}$, $\dot{\lambda}$, and $\dot{h}$ are the aircraft velocity states in the same WGS-84 system. Finally, $\ddot{\phi}$, $\ddot{\lambda}$, and $\ddot{h}$ are the aircraft acceleration

states. An alternative and equally applicable approach, not considered for this paper, is to represent the aircraft position, velocity, and acceleration using an Earth-Centered, Earth-Fixed Cartesian coordinate system.

The next two states parameterize aircraft instrument imperfections. The 10^{th} state, $\dot{\delta}_R$, is the aircraft DME receiver's clock frequency offset. The 11^{th} state, Δh_{bias}, is the aircraft's pressure altimeter bias.

The final $2N$ states parameterize uncertainties associated with N DME ground transponders. States 12 through $(11+N)$ are the DME ground station clock frequency offsets. States $(12+N)$ through $(11+2N)$ are the DME accumulated delta range biases. As discussed in the introduction, the proposed method does not require absolute timing. Therefore, the state vector does not have clock offsets as distinct states. Instead, these delta range biases incorporate the clock offsets, both at the aircraft and in the ground stations, in a manner that accurately represents their effects on the carrier-phase-based accumulated delta range measurements. This lumping of clock offset effects into the accumulated delta range biases has the beneficial effect of helping to ensure system observability.

2.3.2 Aircraft Dynamics

The aircraft discrete-time dynamic propagation model is a simple linear kinematic model. It can be represented in the matrix form:

$$\begin{bmatrix} \phi \\ \lambda \\ h \\ \dot{\phi} \\ \dot{\lambda} \\ \dot{h} \\ \ddot{\phi} \\ \ddot{\lambda} \\ \ddot{h} \end{bmatrix}_{k+1} = \begin{bmatrix} I_3 & \Delta t * I_3 & 0.5\,\Delta t^2 * I_3 \\ 0 & I_3 & \Delta t * I_3 \\ 0 & 0 & I_3 \end{bmatrix} \begin{bmatrix} \phi \\ \lambda \\ h \\ \dot{\phi} \\ \dot{\lambda} \\ \dot{h} \\ \ddot{\phi} \\ \ddot{\lambda} \\ \ddot{h} \end{bmatrix}_{k} + \begin{bmatrix} 0.5\,\Delta t^2 * I_3 \\ \Delta t * I_3 \\ I_3 \end{bmatrix} \underline{v}_{ak} \tag{2.2}$$

$$t_k = k \cdot \Delta t \tag{2.3}$$

In Eq. (2.2), I_3 is the 3-by-3 identity matrix, and 0 is a 3-by-3 matrix with all zero entries. The quantity Δt is the sample interval between DME measurements. Eq. (2.3) defines the discrete sample time t_k with k as the sample index.

The state transition matrix, the block matrix immediately to the right of the equals sign in Eq. (2.2), represents the simple kinematic integration of aircraft position, velocity, and acceleration over one time step. $\underline{v}_{ak}$ is the 3-by-1 time integral of white-noise random jerk. This term is an increment to the acceleration, thereby causing the acceleration to be a random walk. The random vector $\underline{v}_{ak}$ is a sample from a discrete-time white-noise sequence. It is modeled as having zero time correlation, a zero mean, and zero cross-correlation between its individual elements so that its covariance matrix is diagonal.

2.3.3 Clock/Bias Dynamics

A 2-state model for each clock is assumed. This model is taken from [12]. It includes frequency random walk and additional random-walk phase noise. After re-packaging to be consistent with the lumping of clock offsets into accumulated delta range biases, the clock/bias models take the following form:

$$\begin{bmatrix} \beta_i \\ \dot{\delta}_i \end{bmatrix}_{k+1} = \begin{bmatrix} 1 & -\Delta t & \Delta t \\ 0 & 1 & 0 \end{bmatrix} \begin{bmatrix} \beta_i \\ \dot{\delta}_i \\ \dot{\delta}_R \end{bmatrix}_k + \begin{bmatrix} -1 & 0 & 1 \\ 0 & 1 & 0 \end{bmatrix} \begin{bmatrix} v_{p,i} \\ v_{f,i} \\ v_{p,R} \end{bmatrix}_k$$

$$\text{for } i = 1, \ldots, N. \tag{2.4}$$

$$\dot{\delta}_{R_{k+1}} = \dot{\delta}_{R_k} + v_{f,R_k} \tag{2.5}$$

The quantities $v_{p,i}$ and $v_{f,i}$ are the clock offset and clock frequency random process noise for the i^{th} DME ground transponder clock. The quantities $v_{p,R}$ and $v_{f,R}$ are the clock offset and clock frequency random process noise for the aircraft DME receiver clock. Note that typical clock drift models have v_p and v_f correlated to each other for each individual clock [12].

The clock offset and clock frequency random noise for both the transponder clocks and the receiver clock have zero mean. Their covariances depend on the time step, Δt, the minimum root Allan variance of the clock, σ_{Allan}, and the time interval at which the minimum root Allan variance applies, τ_{min}.

$$h_0 = \sigma^2_{Allan}\tau_{min} \tag{2.6}$$

$$h_{-2} = \frac{3h_0}{4\pi^2\tau^2_{min}} \tag{2.7}$$

The quantities h_0 and h_{-2} are the two Allan variance parameters in the 2-state clock model from [12].

Eq. (2.4) applies to each transponder bias and clock frequency offset separately. As discussed before, the bias state includes the clock offset information; therefore, the phase random noise of both the transponder clock and the receiver clock has an effect on the propagation of β_i.

Because the bias state only holds the information about the relative phase offset between the receiver clock and the transponder clock, the phase noise difference, $v_{p,R} - v_{p,i}$, matters. A positive transponder clock offset noise reduces the bias and a positive receiver clock offset noise increases the bias. In a similar manner, the frequency offset difference, $\dot{\delta}_R - \dot{\delta}_i$, enters into the propagation equation.

Eq. (2.5) represents the random walk of the aircraft unit clock frequency offset. The DME ground transponder biases and clock frequency offsets do not affect this state even though this state affects the bias states.

2.3.4 Altimeter Dynamics

The pressure altimeter bias is assumed to be a constant. Therefore, it has a simple dynamic propagation equation:

$$\Delta h_{bias,k+1} = \Delta h_{bias,k} \tag{2.8}$$

2.3.5 Measurement Model

The measurement vector consists of an accumulated delta range measurement for each DME ground station along with the pressure altimeter measurement:

$$\underline{z}_{k+1} = \begin{bmatrix} z_{phase_{i,k+1}} \\ \vdots \\ z_{phase_{N,k+1}} \\ z_{h,k+1} \end{bmatrix} \tag{2.9}$$

Each accumulated delta range measurement is modeled by the following equations:

$$\begin{aligned} z_{phase_{i,k+1}} = \lambda \cdot \phi_{i_{k+1}} &= \rho_{i_{k+1}} + c\delta_{R_{k+1}} - c\delta_{i_{k+1}} + c\alpha_i + w_{i_{k+1}} \\ &= \rho_{i_{k+1}} + c\beta_{i_{k+1}} + w_{i_{k+1}} \end{aligned} \tag{2.10}$$

$$\text{where} \qquad c\beta_{i_{k+1}} = c\delta_{R_{k+1}} - c\delta_{i_{k+1}} + c\alpha_i \tag{2.11}$$

The quantity α_i is the constant accumulated delta range bias. Eq. (2.10) includes this constant bias, as well as the DME ground transponder and aircraft DME receiver range-equivalent clock offsets, $c\delta_{i_{k+1}}$ and $c\delta_{R_{k+1}}$. Eq. (2.11) models the contributions of the constant accumulated delta range bias, of the DME ground transponder clock offset, and of the aircraft DME receiver clock offset to the time-varying accumulated delta range bias, $\beta_{i_{k+1}}$. The final line of Eq. (2.10) represents the actual DME accumulated delta range model used in this paper's truth-model simulation and in its filter.

The quantity $\rho_{i_{k+1}}$ is the distance between the aircraft and the i^{th} DME ground station. This term is the only nonlinear term in the entire filter model. It takes the form

$$\rho_{i_{k+1}} = \sqrt{[\mathbf{r}_{ECEF,i} - \mathbf{r}_{ECEF}(\phi,\lambda,h)]^T [\mathbf{r}_{ECEF,i} - \mathbf{r}_{ECEF}(\phi,\lambda,h)]} \tag{2.12}$$

where $\mathbf{r}_{ECEF,i}$ is the ECEF location of the i^{th} DME ground transponder and $\mathbf{r}_{ECEF}(\phi,\lambda,h)$ is the ECEF position that corresponds to latitude ϕ, longitude λ, and altitude h.

The quantity $w_{i_{k+1}}$ is the discrete-time, zero-mean, Gaussian white noise in the accumulated delta range measurement for the i^{th} DME ground transponder.

The last element of the measurement vector is from the pressure altimeter:

$$z_{h_{k+1}} = h_{k+1} + \Delta h_{bias,k+1} + w_{h_{k+1}} \tag{2.13}$$

The quantity $w_{h_{k+1}}$ is the discrete-time, zero-mean, Gaussian white noise in the pressure altimeter measurement. Thus, the altimeter measurement model includes both an unknown bias and this high-frequency random noise component.

The additional absolute range measurements that are used in the alternative version of this navigation system are modeled by the following equation:

$$z_{\rho_i} = \rho_{i_{k+1}} + w_{\rho_{i,k+1}} \tag{2.14}$$

The quantity $w_{\rho_{i,k+1}}$ is the discrete-time, zero-mean, Gaussian white noise in the absolute range measurement for the i^{th} DME ground transponder.

The measurement vector in the alternative navigation filter and truth model includes the absolute range measurements from a subset of DME ground stations in view:

$$\underline{z}_{k+1} = \begin{bmatrix} z_{phase_i} \\ \vdots \\ z_{phase_N} \\ z_h \\ z_{\rho_j} \\ \vdots \\ z_{\rho_M} \end{bmatrix} \tag{2.15}$$

2.4 Square Root Information Extended Kalman Filter

The Kalman filter algorithm developed in this paper uses the state, dynamics model, and measurement model discussed in the previous section. The results presented in this paper have been generated using a Square Root Information (SRIF) implementation of an Extended Kalman filter. The reader is assumed to be familiar with this type of filter, but more information on Kalman filters can be found in [13] and more information on SRIF implementations is presented in [14].

This Kalman filter performs the usual dynamic propagation step from sample time t_k to sample time t_{k+1} using the state dynamics models in Eqs. (2.2), (2.4), (2.5), and (2.8). It follows each dynamic propagation step by a measurement update that relies on the measurement vector model in Eq. (2.9) for the standard filter and on the model in Eq. (2.15) for the alternative filter that uses sporadic absolute DME range measurements. The filter that uses Eq. (2.9) relies on the constituent models in Eqs. (2.10) and (2.13) to show how the measurements depend on the filter state vector elements and on the mea-

surement noise. The alternate filter that uses Eq. (2.15) relies on constituent Eqs. (2.10), (2.13), and (2.14). The additional absolute range measurements are included every 30 seconds.

Effectively, the EKF linearizes its nonlinear dynamics model and measurement model equations around the current state estimate using first-order Taylor series expansions. It then proceeds with the SRIF form of the standard Kalman filter dynamic propagation and measurement update equations. The SRIF implementation is chosen for its numerical stability compared to the standard Kalman filter and for its capacity to represent zero *a priori* information on state parameters. This capability is needed for the new accumulated delta range bias state that is introduced every time a new DME ground transponder comes into view.

The SRIF form of a Kalman filter works with square-root information matrices and information vectors in place of error covariance matrices and state vector estimates [14]. The *a posteriori* square-root information matrix at time step k, $R_{xx,k}$, and the *a posteriori* information vector, $\zeta_{x,k}$, are defined by the following equations:

$$R_{xx,k}^T \cdot R_{xx,k} = P_k^{-1} \tag{2.16}$$

$$\zeta_{x,k} = R_{xx,k} \cdot \underline{\hat{x}}_k \tag{2.17}$$

The quantity $\underline{\hat{x}}_k$ is the *a posteriori* estimated state vector at time step k, and P_k is the associated *a posteriori* estimation error covariance matrix. $R_{xx,k}$ is an upper triangular matrix. It can be obtained by a Cholesky factorization of P_k, followed by transposition and inversion of the result. Normally, however, the $R_{xx,k}$ matrix is generated directly by the square-root information filter, and Eq. (2.16) is inverted in order to determine the estimation error covariance matrix from $R_{xx,k}$. The *a priori* square-root information

matrix at time step *k+1*, $\bar{R}_{xx,k+1}$, and the *a priori* information vector, $\bar{\zeta}_{x,k+1}$, are related to the *a priori* estimation error covariance matrix, $\bar{P}_{k+1}$, and the *a priori* estimated state vector, $\bar{x}_{k+1}$, in similar ways to Eqs. (2.16-2.17).

This study's proposed filter is adaptive in its state vector dimension. The filter is capable of adding and dropping states related to the DME ground stations as the signal from a DME ground station becomes available or goes out of range. Specifically, a clock frequency offset state and an accumulated delta range bias state are added to the state before the very first Kalman filter measurement update for a ground station whose signal has just become available. Given a state vector with M elements, the new information associated with a new state, the new $(m+1)^{st}$ state in this example, is inserted between the m^{th} and $(m+1)^{st}$ elements of the original *a priori* information vector and *a priori* square-root information matrix by means of the following equations:

$$\bar{R}^{new}_{xx,k+1} = \begin{bmatrix} \bar{R}_{xx,k+1}(1:m,1:m) & 0_{mx1} & \bar{R}_{xx,k+1}(1:m,m+1:M) \\ 0_{1xm} & R_{add} & 0_{1x(M-m)} \\ 0_{(M-m)xm} & 0_{(M-m)x1} & \bar{R}_{xx,k+1}(m+1:M,m+1:M) \end{bmatrix} \tag{2.18}$$

$$\bar{\zeta}^{new}_{x,k+1} = \begin{bmatrix} \bar{\zeta}_{x,k+1}(1:m) \\ \zeta_{add} \\ \bar{\zeta}_{x,k+1}(m+1:M) \end{bmatrix} \tag{2.19}$$

The quantity 0_{ixj} in Eq. (2.18) represents an i-by-j zero matrix. The quantity $\bar{R}_{xx,k+1}(i:j,k:l)$ represents the matrix obtained from the i^{th} to j^{th} rows, and k^{th} to l^{th} columns of $\bar{R}_{xx,k+1}$. If no *a priori* information about the new state is available, R_{add} is set to zero; otherwise, R_{add} is set to $1/\sigma_{add}$, with σ_{add} being the *a priori* standard deviation of the new state. The quantity $\bar{\zeta}_{x,k+1}(i:j)$ in Eq. (2.19) represents the vector obtained from the i^{th} to j^{th} elements of $\bar{\zeta}_{x,k+1}$. If no *a priori* information about the new

state is available, ζ_{add} is set to zero; otherwise, it is set to $\bar{x}_{add}/\sigma_{add}$ where $\bar{x}_{add}$ is the *a priori* estimate of the new state.

The vector $\bar{\zeta}^{new}_{x,k+1}$ and the matrix $\bar{R}^{new}_{xx,k+1}$ are, respectively, the updated *a priori* information vector and square-root information matrix. The process, defined by Eqs. (2.18) and (2.19), is repeated for every new state to be added to the state vector. The new ground transponder clock frequency offset states are initialized with an *a priori* estimate of 0 and with the *a priori* standard deviation given in the left-most column of Table 2.1 divided by c. The new bias states are initialized with zero *a priori* information, i.e., both R_{add} and ζ_{add} are set to zero. All of the initial information about the new bias states will come entirely from the first accumulated delta range measurement from the newly tracked DME ground station.

The associated DME states are dropped off the state vector after the measurement update that contains the final measurement from a particular DME ground station. Given a state vector with M elements, the m^{th} state is dropped from the *a priori* information vector and the *a priori* square-root information matrix by the following equations:

$$R^{'}_{xx,k} = R_{xx,k} \cdot A \tag{2.20}$$

$$Q \cdot R^{''}_{xx,k} = R^{'}_{xx,k} \tag{2.21}$$

$$\zeta^{'}_{x,k} = Q \cdot \zeta_{x,k} \tag{2.22}$$

$$R^{new}_{xx,k} = R^{''}_{xx,k}(2:M, 2:M) \tag{2.23}$$

$$\zeta^{new}_{x,k} = \zeta^{'}_{x,k}(2:M) \tag{2.24}$$

These operations start with a state vector permutation that provides a convenient and statistically correct way to remove the m^{th} state from a square-root information equation. The matrix A in Eq. (2.20) is the corresponding permutation matrix, and $R^{'}_{xx,k}$

is the permuted square root information matrix. The element A_{ij} is 1, where i is the original index of the element in the state vector and j is the new index of the element in the permuted state vector. Other entries of the permutation matrix are set to 0. In order to move the m^{th} state to the top of the state vector, A_{m1} is set to 1. The remaining states are then permuted to the second to M^{th} states in the permuted state vector by setting the appropriate elements of A to 1. The following is an example permutation vector where the third state is to be moved into the first position in preparation for its removal from a four dimensional state vector:

$$A = \begin{bmatrix} 0 & 1 & 0 & 0 \\ 0 & 0 & 1 & 0 \\ 1 & 0 & 0 & 0 \\ 0 & 0 & 0 & 1 \end{bmatrix}$$

Eq. (2.21) implements an orthogonal/upper-triangular (QR) factorization of the permuted square root information matrix, $R'_{xx,k}$. This factorization computes the orthonormal matrix Q and the upper triangular square root information matrix $R''_{xx,k}$ that achieves equality with the column-permuted square-root information matrix on the right-hand side of Eq. (2.21). $R''_{xx,k}$ is a valid square-root information matrix for the permuted state vector.

After these permutations move the state to be dropped to become the first element of the state vector, it can be dropped from further consideration by the filter by removing the first column and the first row from the permuted information matrix in Eq. (2.23) and

Clock	σ_f (m/sec)	Min. Root Allan Variance	τ_{min} (sec)
DME GS	0.03	1.0e-13	3000
Aircraft	30	1.0e-11	10

Table 2.1: Clock standards

by removing the first element from the corresponding information vector in Eq. (2.24).

The vector $\zeta_{x,k}^{new}$ and the matrix $R_{xx,k}^{new}$ are, respectively, the updated *a posteriori* information vector and square-root information matrix. This process, defined by Eqs. (2.20-2.24), is repeated for the clock frequency offset state and the accumulated delta range bias state for every DME station that goes out of view.

The plot on the left in Fig. 2.2 shows an example of the varying number of ground stations in view for a simulation case. The plot on the right in the same figure shows the corresponding variations in the state vector dimension.

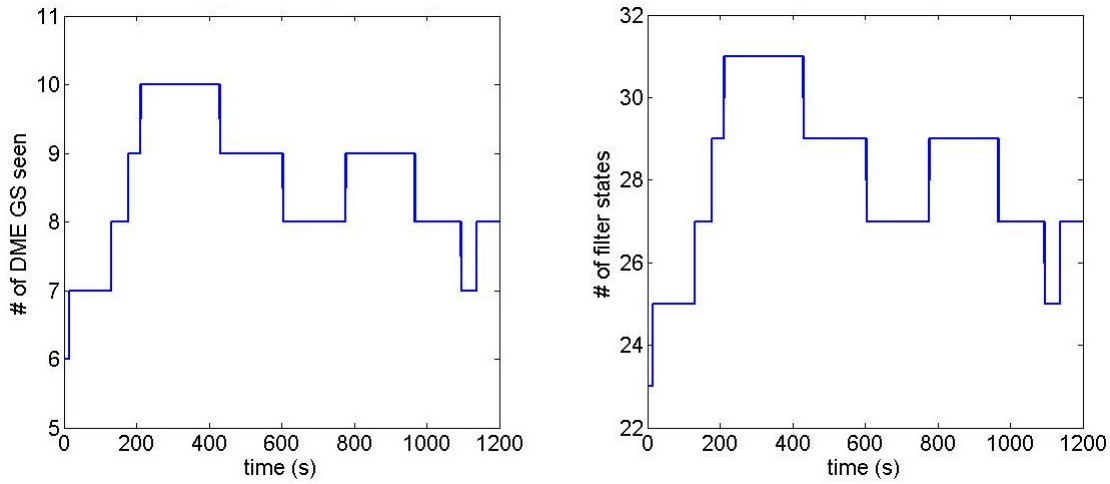

Figure 2.2: *Time history of count of visible DME ground transponders and filter state dimension for a simulation case over the Montana/Dakota region at an altitude of 30000 ft and a speed of 500 kts*

2.5 Truth-Model Simulation

A medium-fidelity truth-model simulation is used to obtain the measurement data necessary for assessment of the proposed filter. This simulation also produces the "truth" aircraft trajectory states and the "truth" clock frequency offset states. The filter's perfor-

mance is evaluated by comparing these "truth" states with their corresponding estimates in the filter.

Three different sets of DME ground stations and regions of aircraft operation are considered. These are shown in Fig. 2.3. The magenta "x" signs are the DME stations of the New York State (NYS) region. The NYS region is considered to be the nominal case for this study. It has good DME ground station density and good geometric diversity of the direction vectors from the visible DME ground transponders to any aircraft flying near its center. The black triangle signs are the DME ground stations of the Montana/Dakota region. This second region has been chosen in order to study the effects of low DME ground station density. In the truth-model simulations, a flight path that traverses the interior of the given region is considered for each of these regions.

The last region, the Mid/South Atlantic seaboard region, is the one whose DME ground transponders are indicated by cyan plus signs. It has been chosen in order to study the effects of insufficient geometric diversity. This region is used to study how the system works while the aircraft is off the Atlantic coast of the southern U.S. and, therefore, all visible ground stations are to the west of the aircraft. A flight path that keeps the aircraft approximately 100 km from the coast is studied for this region.

The ground station locations that have been used in the study are not actual DME or TACAN stations. DME and TACAN ground station locations in these areas have been used with slight random perturbations in order to respect possible restrictions about disclosing their exact locations. The added latitude and longitude perturbations were in the range ± 4 km, and the added altitude perturbations were in the range ± 200 m.

The duration of each truth-model simulation is 1200 seconds. A sampling frequency of 10 Hz, with a corresponding Δt of 0.1 seconds, has been used.

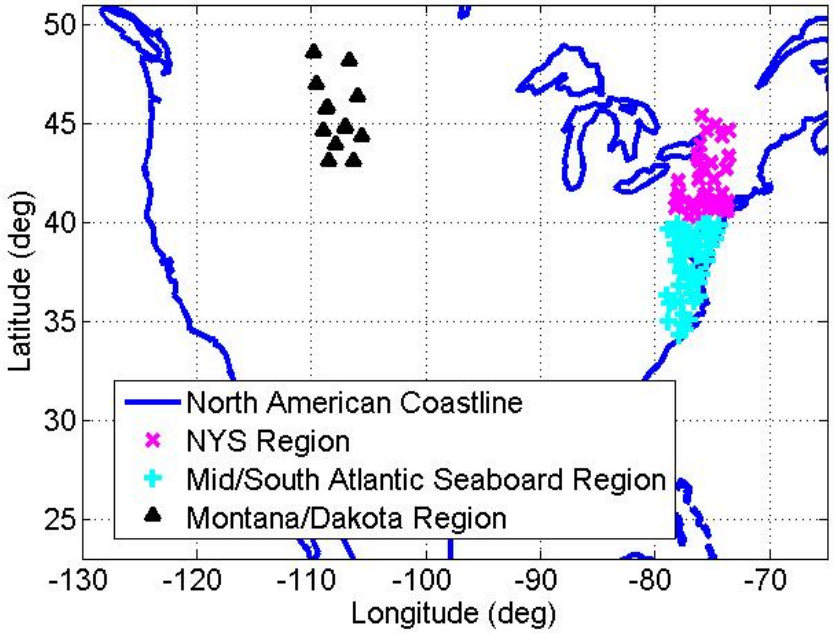

Figure 2.3: *DME ground transponder locations for 3 regions of APNT study*

For each region, three sets of aircraft speeds (60, 200, and 500 knots) are considered. Furthermore, for each region/speed pair, three sets of aircraft altitudes are studied. Altitudes of 5000, 10000, and 30000 feet are chosen for the NYS and Mid/South Atlantic seaboard regions. Because the average ground altitude in the Montana/Dakota region is 3000 feet, altitudes of 8000, 13000, and 30000 feet are instead studied for this region. This change puts the aircraft 5000 and 10000 feet above ground for the two low-altitude cases, similar to the first two regions.

The "truth" state vector is propagated for the duration of the simulation using the state dynamics described in the second section. This propagation includes the random effects of the process noise terms $\underline{v}_{ak}$, $v_{p,i}$, $v_{f,i}$, $v_{p,R}$, and $v_{f,R}$. These process noise terms are generated using a random number generator, and each individual simulation uses different samples of the process noise distributions, thus producing a slightly different actual trajectory through the filter's state space.

Table 2.1 shows the clock model uncertainty parameters that are used for the truth-model simulation. The covariances for $v_{p,i}$, $v_{f,i}$, $v_{p,R}$, and $v_{f,R}$ are determined by the minimum root Allan variance and the time interval over which this minimum applies, τ_{min}. The initial range-rate-equivalent clock frequency error standard deviation, σ_f, is the initial standard deviation of $c \cdot \dot{\delta}_R$ for the aircraft DME receiver and of $c \cdot \dot{\delta}_i$ for a ground station DME transponder. The values of σ_f, the minimum root Allan variance, and τ_{min} are chosen to be consistent with the use of rubidium clocks for the DME ground station clocks and with an ovenized crystal oscillator for the aircraft receiver [15]. The assumption of rubidium clocks for the DME ground station clocks is chosen to investigate how well the proposed APNT system performs if the DME stations are upgraded to this level of clock stability. This is not the current stability level of DME ground station clocks, but the use of rubidium clocks is a reasonable upgrade to study a possible APNT service with the current DME ground stations.

The integrated white-noise random jerk in the aircraft dynamics model has standard deviations of 1e-11 rad/sec^2, 1e-11 rad/sec^2, and 5e-7 m/sec^2, respectively, for the latitude, longitude, and altitude acceleration process noise components in $\underline{v}_{ak}$ from Eq. (2.2). These yield potential increases of $(0.00035\ rad)^2$, $(0.00035\ rad)^2$, and $(17\ m)^2$ in the respective latitude, longitude, and altitude position error variances over the 1200 second simulation interval. The potential latitude and longitude variance increases correspond to a north/south variance increase of $(2200\ m)^2$ and an east/west variance increase of $(1700\ m)^2$. The navigation filter will use accumulated delta range data in order to counteract this tendency for position uncertainty to increase.

For each case, as indicated by the particular combination of the ground station region, the aircraft speed, and the aircraft altitude, 100 truth-model simulations have been run with the same initial position, velocity, and acceleration states, randomized initial

filter errors, randomized process noise, and randomized measurement noise. The initial altitude rate and the initial acceleration states are set to 0 for all cases.

At each time step of the simulation, the expected measurement vector is calculated using the propagated state vector. First, however, a minimum/maximum DME signal range of 10/240 km is applied to the simulation. This range limit is considered at each time step in order to assess whether the signal from a DME ground station can be realistically received by the aircraft receiver. Below the minimum range of 10 km, an aircraft passes into a null of the DME ground transponder antenna. DME signals have been tracked up to 240 km [16] and this range is chosen as the maximum signal range . Excellent DME carrier phase tracking up to 90 km with a handicap of additional noise and a low power transponder has been shown [9]. The results in [9] indicate that the 0.02 m carrier phase standard deviation is conservative up to this range. We believe that the applicability of this accuracy level up to 240 km is feasible because the same paper concludes that the carrier phase tracking range can be significantly improved with high-fidelity instruments.

Next, the pathway of the signal from the DME ground station to the receiver is analyzed for ground obstruction. The simulation determines if the path of the signal pierces the 0-altitude WGS-84 ellipsoid. At each time step, the phase measurements from only the DME ground stations that do not violate the range limit and the 0-altitude piercing condition are included in the measurement vector. This effectively gives a zero elevation cutoff as viewed from the transmitter. In the future, it may be wise to enforce a higher minimum elevation cutoff because it may be unrealistic to expect good signal performance for zero elevation transmissions from DME ground stations. The pressure altimeter measurement is appended to the measurement vector after all the available DME measurements.

Respective standard deviations of 0.02 meters and 18 meters are chosen for the discrete-time Gaussian white noise in each accumulated delta range measurement and in the pressure altimeter measurement.

The pressure altimeter bias is sampled from a zero-mean, 18-m standard deviation Gaussian distribution for each of the 100 simulation runs. Thus, it has a different value for each run.

In the modified version of the method, absolute range measurements from 2 DME ground stations in view that result in the best horizontal dilution of precision are added to the measurement vector every 30 seconds, starting with the first set of measurements. A standard deviation of 37 meters (0.02 nm) is chosen for the discrete-time Gaussian white noise on these absolute range measurements [16].

2.6 SRIF Performance When Applied to Data from Truth-Model Simulations

The Kalman filter, discussed in the Square Root Information Extended Kalman Filter section, has been tested using the data from the truth-model simulation. The filter is initialized with an aircraft position that is sampled from a distribution with 9.1×10^{-5} rad (577 m, 0.312 nm), 1.1×10^{-4} rad (577 m, 0.312 nm), and 577 m 1-σ errors respectively in latitude, longitude, and altitude. The aircraft velocity is sampled with 9.1×10^{-7} rad/sec (5.77 m/sec), 1.1×10^{-6} rad/sec (5.77 m/sec), and 5.77 m/sec 1-σ respective errors in latitude, longitude, and altitude rates. The corresponding filter square-root information matrices are initialized using these same standard deviations. The initial filter aircraft accelerations are set to 0, while the respective latitude, lon-

gitude, and altitude acceleration error standard deviations used to initialize the filter's square-root information matrices are set to 1×10^{-8} rad/sec^2 (0.064 m/sec^2), 1×10^{-8} rad/sec^2 (0.053 m/sec^2), and 0.1 m/sec^2.

For each case, the filter is applied to the 100 simulation runs, and the filter results are compared with the 100 true state histories from the truth-model simulation in order to carry out a statistical analysis of filter performance. Figs. 2.4, 2.5, and 2.6 are from an example case that flies through the Montana/Dakota region. The aircraft has a nominal speed of 500 kts and a nominal altitude of 30000 ft. An example simulated aircraft trajectory over this region is depicted in Fig. 2.4 by the blue line, starting from the green circle and ending at the magenta "x". The DME ground stations are shown by the red asterisks.

Fig. 2.5 compares the state estimation error standard deviation time histories for the latitude, longitude, and altitude computed by the filter with those calculated by computing the 100-simulation-case statistics of the differences between the estimated filter position components and the simulated truth values of these components. The vertical axes for the latitude and longitude plots use a logarithmic scale. The bottom plot for the altitude error standard deviation is on a linear scale. For all three position states, the standard deviation reported by the filter (blue dashed lines) matches fairly well with the true error standard deviation (red solid lines).

Fig. 2.6 shows the filter convergence for the clock frequency offset states in their range-rate-equivalent forms, $c\dot{\delta}_R$ and $c\dot{\delta}_i$. The vertical axis of the left plot is on a logarithmic scale and the right plot is on a linear scale. The filter is able to bring the uncertainty in the clock frequency states down to 0.01 m/sec during the 1200 seconds of simulated trajectory, for both the aircraft clock on the left and a representative DME clock on the right. Note how the DME clock frequency offset starts its convergence

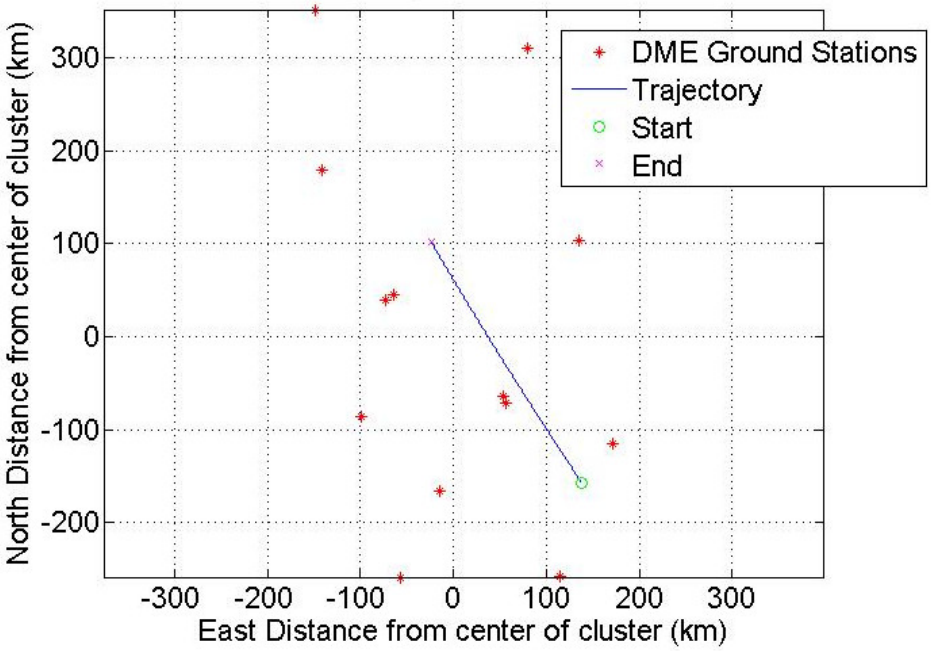

Figure 2.4: *Plan view of an example simulated aircraft trajectory over the Montana/Dakota region at an altitude of 30000 ft and a speed of 500 kts*

about 180 sec after the filter initialization. This happens because this particular ground station is not visible until that time.

2.6.1 Results for NYS Region Using Only Accumulated Delta Range Measurements

Summaries of the filter results for the 3 different regions are presented in Tables 2.2-2.4. The NYS region is presented in Table 2.2. The first and second columns define the corresponding case's altitude/speed combination. The third column, N_{avg}, indicates the average number of ground stations in view for the duration of the simulation. The fourth column presents the time when the filter has converged to a navigation solution in latitude and longitude with a per-axis 1-σ accuracy of 0.025 nautical miles (46.3 m). The top two panels of Fig. 2.5 illustrate how this number is obtained for that figure's

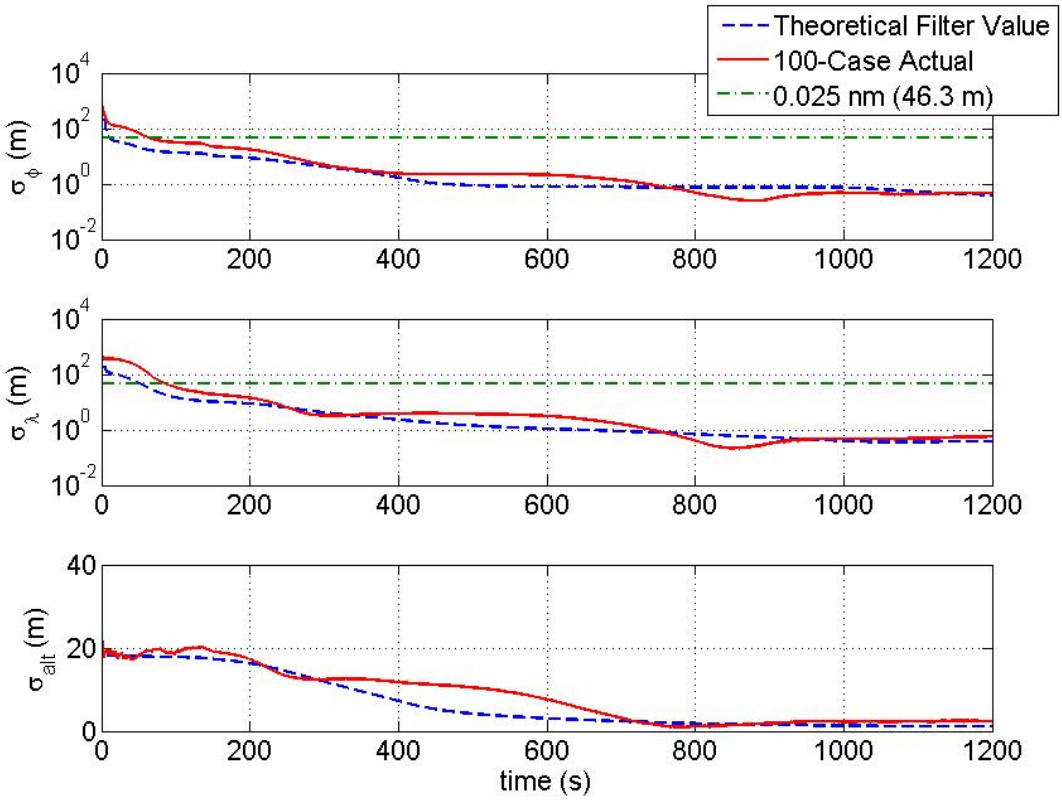

Figure 2.5: *Latitude, longitude, and altitude position error standard deviation time histories for the cases in the Montana/Dakota region at an altitude of 30000 ft and a speed of 500 kts*

corresponding table entry: by determining the intersection of the 46.3 m goal (green dashed lines) and the true error standard deviation (red solid lines). The greater number from the two panels is reported as the convergence time. This convergence time yields a 95% confidence that the latitude and longitude error is no larger than 0.05 nm, which is a sufficient accuracy level to meet the RNAV 0.1 requirement. The fifth, sixth, and seventh columns are the steady-state 1-σ accuracies achieved by the filter in latitude, longitude, and altitude, from left to right.

The filter has converged to the 0.025 nm horizontal accuracy within the 1200 second simulation duration in all cases for the NYS region. Moreover, the steady-state horizontal accuracy values are much better than the 0.025 nautical mile (46.3 m) goal.

Altitude (ft)	Speed (kt)	N_{avg}	Convergence Time to 0.025 nm lat/long (s)	$\sigma_{Lat,ss}$ (m)	$\sigma_{Long,ss}$ (m)	$\sigma_{alt,ss}$ (m)
5000	60	22	762	17	13	138
	200		323	0.5	3	88
	500		132	0.2	0.8	15
10000	60	28	860	19	15	106
	200		390	0.6	6	71
	500		85	0.05	0.14	1.5
30000	60	30	875	15	15	54
	200		302	0.2	0.9	5
	500		110	0.05	0.1	0.8

Table 2.2: Summary of filter results for NYS region

The results indicate that altitude does not have a significant effect on filter convergence. The aircraft speed, however, noticeably alters both the convergence time and the steady-state accuracy. In particular, the cases with a speed of 500 kts show the best results, while the cases with a speed of 60 kts give the worst results. This is consistent with the nature of the navigation information that is contained in accumulated delta range time histories. A higher speed improves the observability for the system, and these results confirm this expectation.

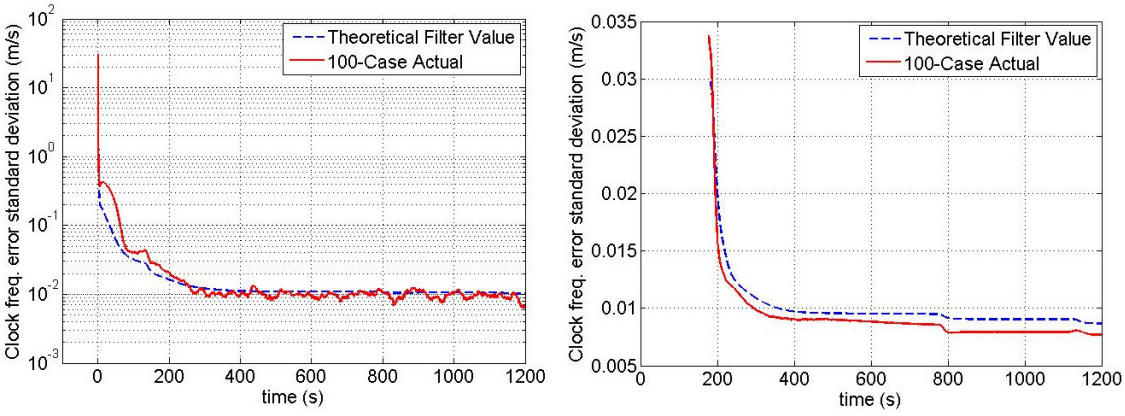

Figure 2.6: *Range-rate-equivalent clock frequency error standard deviation time histories for the airborne receiver (left) and a representative DME ground transponder (right) for the case in the Montana/Dakota region at an altitude of 30000 ft and a speed of 500 kts*

2.6.2 Results for Montana/Dakota Region Using Only Accumulated Delta Range Measurements

A summary of the filter results for the Montana/Dakota region is presented in Table 2.3. The column structure is the same as in Table 2.2. This region has an overall smaller number of ground stations in view for all cases. The symbol "-" in the convergence time column represents a failure to converge to lateral error standard deviations below 0.025 nm in the simulation duration of 1200 seconds. The symbol "*" attached to a number in the steady-state accuracy columns indicates that this number is not a steady-state value in reality, but rather the value the filter reached at the end of the simulation duration. In other words, the filter covariance time histories did not converge to an obvious steady-state value. Instead, they were still declining at the 1200 sec final time and likely would converge at some later time.

Unlike in the NYS region, where the filter has converged in all cases, in the Montana/Dakota region the filter has failed to converge for the cases with a speed of 60 kts. Moreover, the filter has slower convergence times for the 200 kt cases, roughly comparable convergence times for the 500 kt cases, poorer latitude accuracy in all cases, and comparable or poorer longitude accuracy in all cases. However, for all the cases in which the filter does indeed converge, the steady-state horizontal position uncertainty values are again significantly below the 0.025 nautical miles (46.3 m) goal.

In order to assess the impact of the initial DME clock frequency error uncertainty on the 60 kt cases, an additional case has been investigated. The 60 kt, 8000 ft case has been repeated with initial DME clock frequency error range-rate-equivalent 1-σ values of 0.003 m/sec instead of 0.03 m/sec. Its results are reported in italics in Table 2.3, i.e., in the second line. This line shows improvement in the 1-σ accuracy values; however, the

Altitude (ft)	Speed (kt)	N_{avg}	Convergence Time to 0.025 nm lat/long (s)	$\sigma_{Lat,ss}$ (m)	$\sigma_{Long,ss}$ (m)	$\sigma_{alt,ss}$ (m)
8000	60	7	-	68*	122*	25
	60		-	*38*	*70**	*22*
	200		450	1.7	2.6	39
	500		96	0.7	0.6	18
13000	60	9	-	60*	65*	23
	200		473	3.5	5.9	48
	500		90	0.6	0.7	7
30000	60	9	-	62*	105*	23
	200		510	4.9	8.1	22
	500		92	0.5	0.7	3

Table 2.3: Summary of filter results for Montana/Dakota region

filter still fails to converge to a situation where both horizontal error standard deviations are below 0.025 nm (46.3 m) within the 1200 sec simulation window.

2.6.3 Results for Mid/South Atlantic Seaboard Region Using Only Accumulated Delta Range Measurements

A summary of the filter results for the Mid/South Atlantic seaboard region is presented in Table 2.4. The column structure is the same as in Table 2.2. The symbols "-" and "*" have the same meanings as in Table 2.3.

The 60 kts cases have failed to converge, similar to the Montana/Dakota region. This region presents another failed convergence case, with a speed of 200 kts and an altitude of 5000 feet. This case has been repeated with initial DME clock frequency error range-rate-equivalent 1-σ values of 0.003 m/sec instead of 0.03 m/sec. The results, reported in italics on the third line of Table 2.4, show that a lower initial DME clock frequency error uncertainty leads to an actual convergence, unlike the attempt at 60 kts in the

Altitude (ft)	Speed (kt)	N_{avg}	Convergence Time to 0.025 nm lat/long (s)	$\sigma_{Lat,ss}$ (m)	$\sigma_{Long,ss}$ (m)	$\sigma_{alt,ss}$ (m)
5000	60	5	-	390	304	16
	200		-	93*	40	18
	200		*644*	*15*	*18*	*18*
	500		510	3.7	8	17
10000	60	10	-	198*	177*	19
	200		890	4.9	2.7	17
	500		374	0.6	1.5	17
30000	60	12	-	180*	177*	21
	200		882	4.9	3.1	16
	500		369	0.9	2.0	13

Table 2.4: Summary of filter results for Mid/South Atlantic Seaboard region

Montana/Dakota region.

As expected, the insufficient DME geometric diversity in this region leads to inferior results both in convergence times and in the steady-state horizontal position accuracy values. In the converged cases, however, the steady-state horizontal accuracy values are again significantly better than the 0.025 nautical mile (46.3 m) goal.

2.6.4 Results from the Filter with Absolute Range Measurements

The cases that have convergence issues have been re-investigated with the modified version of the proposed method that includes intermittent DME absolute range measurements once every 30 seconds from 2 of the visible ground stations. In addition, a series of cases that show good convergence rates and steady-state accuracies have been re-analyzed with the modified version of the proposed method. A summary of the filter results for all of these cases is presented in Table 2.5.

The problematic low-speed cases for the Mid/South Atlantic seaboard region and the

Region	Altitude (ft)	Speed (kt)	Convergence Time to 0.025 nm lat/long (s)	$\sigma_{Lat,ss}$ (m)	$\sigma_{Long,ss}$ (m)	$\sigma_{alt,ss}$ (m)
Mid/South Atlantic seaboard	5000	60	90	15	10	21
	5000	200	120	12	9	21
	10000	60	150	14	6	23
	30000	60	90	12	5	22
Montana/ Dakota	8000	60	150	8	6	27
	13000	60	150	5	6	25
	30000	60	120	7	7	21
NYS	5000	60	0	5	2	45
	10000	60	0	2	2	14
	10000	200	0	0.2	0.3	4
	10000	500	0	0.04	0.1	0.9
	30000	60	0	2	2	6
	30000	200	0	0.1	0.4	1
	30000	500	0	0.06	0.1	0.5

Table 2.5: Summary of filter results for the method that incorporates sporadic use of two-way ranging

Montana/Dakota region have managed to converge within 150 seconds in the modified method. As indicated before, these cases failed to converge to the desired accuracy values without the use of absolute range measurements. The latitude and longitude steady-state 1-σ accuracy values are no greater than 15 meters for all these cases.

The cases for the NYS region in Table 2.5 are the cases that did not have any convergence issues in the original method. However, the modified filter still shows very remarkable improvements. The convergence times for all NYS region cases have been reduced to 0 seconds. This indicates that the 1-σ uncertainties in latitude and longitude have been reduced below the 0.025 nm (46.3 m) level with the first set of measurements that include absolute range measurements, and they have stayed below this level for the rest of the simulation. The results show that the absolute range measurements in the initial sample are sufficient for convergence purposes in these cases. The steady-state accuracy values for these cases have significantly improved to levels much below the

desired accuracy goal.

Overall, the intermittent use of absolute range measurements has solved the convergence issues for the problematic cases. Furthermore, the modified filter decreases the convergence times of cases that achieve convergence in the original filter implementation that relies only on accumulated delta range measurements.

2.6.5 Results for the Minimum Required Number of Ground Stations

Table 2.6 presents the results from simulations that investigated the minimum number of DME ground stations that need to be tracked simultaneously for satisfactory convergence times. These simulations have been run in the NYS Region for all altitude/speed pairs described previously. The filter has been modified to choose an optimal set of 3, 4, 5, or 6 DME ground stations, with regard to horizontal dilution of precision, from the ground stations in view at every time step. The first number in each entry in columns 3 through 6 indicates the convergence time to 0.025 nm for the filter that does not use absolute range measurements, and the second number shows the same convergence time with 2 absolute range measurements used every 30 seconds. The symbol "-" indicates a failure to converge by the end of the 1200 sec simulation.

The original method has noticeable problems with all of the 60 kt cases without absolute range measurements. The results improve as the aircraft speed increases, but the altitude doesn't have a significant effect. The convergence times decrease significantly when the number of ground stations is increased from 3 to 4. Specifically, the 200 kt cases for all altitudes have gone from not converging within the simulation dura-

Altitude (ft)	Speed (kt)	Convergence Time to 0.025 nm lat/long (s) with n DME ground stations (no absolute DMEs | 2 absolute DMEs once every 30 sec)			
		n = 3	n = 4	n = 5	n = 6
5000	60	- | 30	- | 0	- | 0	- | 0
	200	- | 30	426 | 0	344 | 0	350 | 0
	500	250 | 30	122 | 0	131 | 0	133 | 0
10000	60	- | 30	- | 0	- | 0	- | 0
	200	- | 30	540 | 0	352 | 0	363 | 0
	500	268 | 30	132 | 0	120 | 0	140 | 0
30000	60	- | 30	- | 0	- | 0	- | 0
	200	- | 30	655 | 0	410 | 0	393 | 0
	500	325 | 30	137 | 0	142 | 0	140 | 0

Table 2.6: Summary of filter results for NYS region with different number of DME ground stations tracked

tion to converging in under 660 seconds. Increasing the number of ground stations to 5 has improved the convergence times slightly for the cases with an altitude of 10000 ft. The cases with an altitude of 30000 ft show mixed results when increasing from 4 to 5 ground stations. The convergence times do not change significantly with the increase of the number of ground stations from 5 to 6.

In contrast, the modified method that utilizes the absolute range measurements shows no convergence issues. The 60 kt cases, which have failed to converge with the original method, have been successfully tracked with the modified filter. All of the cases with 3 ground stations have converged in 30 seconds. There is a noticeable improvement in the filter's performance when the number of ground stations is increased from 3 to 4, after which the convergence time drops to 0 for all cases. This indicates that the filter has managed to bring the 1-σ uncertainty in latitude and longitude below the 0.025 nm (46.3 m) level with the first set of measurements that include absolute range measurements, and it has managed to stay below this level for the whole simulation. Further increases of the number of ground stations to 5 or 6 show no more improvements, naturally. The convergence times stay at 0 for all the cases with these two numbers of ground stations.

Given the success of the modified method in the NYS region, a logical follow-up question is to assess the performance in an area with bad geometric diversity or a low number of ground stations. Another important question is whether the current DME ground stations cover the whole United States in a way that guarantees performance levels similar to the NYS region. Although important, these questions are not answered in this paper, and they are left for a future study.

The filter with only accumulated delta range measurements shows poor performance at low aircraft speeds. This could be problematic for an aircraft after takeoff or just before landing due to the reduced aircraft speed during terminal area operations compared to the speed at cruise. Another problem for terminal area operations is low altitude, which causes a reduction in the number of visible ground stations. This reduction might be severe enough to render even the filter with absolute range measurements inadequate for position estimation. This study does not encourage optimism about the performance of the proposed systems for terminal area operations.

2.7 Summary and Conclusions

This paper has investigated a new method for APNT based on DME carrier phase. An SRIF implementation of an Extended Kalman filter has been developed to compute navigation solutions from time series of DME carrier phase data, and a Monte Carlo truth-model simulation has been conducted to assess the likely performance of this proposed APNT method.

The results suggest that given enough time, a sufficient aircraft speed, and a reasonable number of visible ground stations, the SRIF filter is able to achieve convergence. Furthermore, the steady-state accuracy observed in the converged cases is not

only within useful range for APNT, defined as 0.025 nautical mile 1-σ error in order to satisfy RNAV 0.1 requirements, but it can be an order of magnitude below this threshold in many cases.

The cases that have been considered indicate that altitude has a relatively minor effect on filter performance, and they confirm that sufficient ground station density and sufficient geometric diversity together allow faster filter convergence. In addition, an increase in aircraft speed improves both the convergence speed of the position estimate and its steady-state accuracy.

The addition of intermittent absolute range measurements to a few DME ground stations helps alleviate the convergence issues encountered in the cases with poor geometric diversity or low aircraft speed and improves convergence rates in general. Additionally, tracking a minimum of 4 DME ground stations aided by absolute range measurements keeps the uncertainty in latitude and longitude below the 0.025 nm (46.3 m) goal for all cases.

The accuracy levels demonstrated by this simulation study suggest potential usefulness of the proposed method as part of an APNT solution. The results show that the system with only accumulated delta range measurements yields a navigation solution for medium to high speed aircraft, whereas the modified system with the intermittent absolute range measurements is able to deliver consistent filter convergence for the low speed cases as well.

CHAPTER 3

GNSS MULTIPATH DETECTION AND ESTIMATION WITH A SMALL ANTENNA ARRAY

3.1 Abstract

A method that detects multipath in GNSS signals by considering accumulation-type measurements in an antenna array is developed. The goal of the system is to mitigate multipath effects by exploiting direction-of-arrival and polarization difference in the multipath. A batch filter is used to estimate the code phase, carrier Doppler shift, direction of arrival, and phasors of the left-hand and right-hand circularly polarized components of the direct and multipath signals. The method employs a novel test statistic to determine the number of signals present, and it uses an incremental search for the number of signals based on this test statistic. Truth-model simulation results show accurate estimation of all direct and multipath features with up to 2 multipath signals. This hold true even when there is direction-of-arrival overlap. RMS errors in co-elevation and azimuth angles stay below one degree for all the considered cases. RMS error in code phase is around 0.004 chips, and successful labeling of the direct signal based on the estimated code phase is observed. Further analysis indicates the robustness of the proposed method to minor model mismatch.

3.2 Introduction

Multipath distortion is a significant source of error in Global Navigation Satellite System (GNSS) based navigation. Reflected multipath signals distort the accumulations within

a typical GNSS receiver. These unwanted distortions can lead to erroneous carrier phase and code phase measurements, and result in inaccurate position and velocity estimates.

Various methods have been proposed for the problem of multipath detection and mitigation, both in single- and multiple-antenna configurations. For single-antenna receivers, existing solutions include the Multipath Estimating Delay Lock Loop (MEDDL) [17], the Modified Sequential Maximum Likelihood (MSML) method [18], and a moving antenna approach that uses synthetic aperture techniques [19]. For multiple-antenna receivers, exploitation of directional diversity is a common and effective method to mitigate multipath. Existing multi-antenna methods include statistical detection [20], mitigation using a moving antenna array [21], and signal direction-of-arrival (DOA) estimation using a uniform linear array [22].

The use of cross-correlation between antenna feeds to estimate DOA has been explored in the radio imaging field [23–27]. Such a method relies on calculating the covariance matrix between different feeds of an antenna array and extracting the number of signals and their directions-of-arrival from this sparse covariance matrix. These cross-correlation methods are limited in their use for the problem explored in this paper. First, most of these methods rely on the assumption that signals coming from different source directions are uncorrelated, whereas the direct signal and the multipath signals are highly correlated for the multipath problem. Second, even for the methods that account for correlated signals, a high signal-to-noise ratio (SNR) is required for successful estimation. These methods fail in detecting signals below an SNR of -10 dB, whereas the GPS multipath problem has a SNR of around -20 to -25 dB at sampling frequencies that capture the entire RF bandwidth. Third, these methods have limited resolution in their DOA separation compared to the method discussed in this paper. Moreover, since these methods find signals in the feed space, they require an iterative search to go from

the solution in the feed space to the direction space, which negates the decreased number of calculations due to a lack of non-linear operations.

This paper develops a multipath detector and estimator based on batch filtering of data from an antenna array. The estimator employs models of the amplitude and phase response of each antenna feed to each of the two possible circular polarizations as functions of direction-of-arrival. This model operates at the level of in-phase and quadrature accumulations. It implements an iterative method of estimating a set of parameters that characterize the contribution of each incident signal to the measured accumulations. Prior work [28] has shown that a maximum likelihood estimator (MLE) for estimating code delay, direction-of-arrival, Doppler frequency, and complex amplitude of the direct and multipath signals is possible. The proposed antenna array includes two feeds per antenna to make the polarization of the direct and multipath signals observable. The estimation of signal polarization enables further separation between the direct and multipath signals because multipath signals typically have linear polarization, unlike the right-hand circular polarization of direct GNSS signals.

This paper makes two significant contributions to the subject of multipath detection and estimation with an antenna array. First, it develops a maximum likelihood estimator that processes accumulations from a single interval, but using multiple code delay offsets, in order to estimate the following characteristics of each received signal, whether direct or multipath: code delay, carrier phase, carrier Doppler shift, direction-of-arrival (azimuth/co-elevation), and the phasors of the left-hand circularly polarized (LHCP) component and the right-hand circularly polarized (RHCP) component. No known prior result demonstrates observability of all these quantities from a single accumulation interval. This paper's second contribution is to apply its estimator to the output of a truth-model simulation in order to demonstrate observability of its full state space

and to deduce estimator performance in various scenarios that include model mismatch.

The remainder of the paper is organized as follows. The second section provides a detailed description of the signal and accumulation models for use in this paper's batch estimator and truth-model simulation. The third section describes this paper's estimation algorithm. The fourth section explains the functioning of the truth-model simulation. The fifth section presents the results of applying the estimator to the simulated data. The paper's summary and conclusions are presented in its sixth section.

3.3 Data Model

This section develops the signal and accumulation measurement models that are used by the truth-model simulation and by the corresponding estimator.

3.3.1 Signal Model

Given an antenna array with N antennas, with two feeds for each antenna, one designed mainly to receive RHCP signals and the other designed mainly to receive LHCP signals, the complex baseband output of the RF front-end of the n^{th} antenna array feed is described as:

$$y_i^n = y_{Ii}^n + j\, y_{Qi}^n = \sum_{m=1}^{M} \left[\tilde{A}_{Rm} G_R^n(\theta_m, \phi_m) + \tilde{A}_{Lm} G_L^n(\theta_m, \phi_m)\right] e^{j\omega_{Dm}(t_i - t_0)}\, C_m[(1+\eta_m)(t_i - \tau_m)] + v_{Ii}^n + j\, v_{Qi}^n \tag{3.1}$$

The quantities y_{Ii}^n and y_{Qi}^n are, respectively, the real and imaginary components of

the complex baseband RF front-end output sample, y_i^n, at the receiver clock time t_i. The sample period is $\Delta t = t_{i+1} - t_i$. The total number of antenna feeds is $2N$. There are M received signals.

Each signal is characterized by the following set of parameters. The quantities $\tilde{A}_{Rm}$ and $\tilde{A}_{Lm}$ are, respectively, the RHCP and LHCP signal phasors. These quantities are complex scalars. They define the received amplitudes and initial carrier phases of the two signal components for the m^{th} signal as it would've been received at the center of the antenna array and at the initial time t_0. The m^{th} signal's direction-of-arrival is parameterized by the quantities θ_m and ϕ_m. These are, respectively, the co-elevation and azimuth angles defined in the antenna array's coordinate system. The DOA for each signal is assumed to be constant over the accumulation interval. The quantity ω_{Dm} is the carrier Doppler shift for the m^{th} signal. The related quantity η_m is the non-dimensional code Doppler shift. It can be obtained by dividing ω_{Dm} by the nominal carrier frequency ω_c. Each signal's carrier Doppler shift is assumed to be constant. The quantity τ_m describes the start time of the m^{th} signal's PRN code at the array. The PRN code is described by the function $C_m(t)$. Because the direct and multipath signals from each satellite share the same PRN code, they form a subset of the M signals that shares identical $C_m(t)$ functions. In summary, the parameters of the m^{th} signal are $\tilde{A}_{Rm}$, $\tilde{A}_{Lm}$, θ_m, ϕ_m, ω_{Dm} and τ_m. Given that $\tilde{A}_{Rm}$ and $\tilde{A}_{Lm}$ are complex, there are a total of 8 real parameters for each signal.

The functions $G_R^n(\theta_m, \phi_m)$ and $G_L^n(\theta_m, \phi_m)$ are the complex-valued steering functions of the n^{th} antenna feed for, respectively, incident RHCP and LHCP signals. They characterize the amplitude and phase effects of direction variations for the two polarizations. If the n^{th} feed is tuned primarily for RHCP signals, then one would expect $G_R^n(\theta_m, \phi_m)$ to have a larger complex magnitude than $G_L^n(\theta_m, \phi_m)$ in the antenna's most sensitive

directions, and vice-versa for an LHCP feed.

The noise terms v_{Ii}^n and v_{Qi}^n are the in-phase and quadrature measurement noise. They are modeled as being zero-mean, Gaussian white noise. The noise terms are uncorrelated between different feeds. The in-phase and quadrature noise components for each feed are uncorrelated. All components are assumed to have the same variance σ_v^2. The following equations describe the whiteness and lack of correlation for the noise terms:

$$E[v_{Ii}^m v_{Ik}^n] = E[v_{Qi}^m v_{Qk}^n] = \delta_{mn}\ \delta_{ik}\ \sigma_v^2 \tag{3.2}$$

$$E[v_{Ii}^m v_{Qk}^n] = 0 \qquad \text{for any combination of } i,\ k,\ m, \text{ and } n \tag{3.3}$$

The quantities δ_{mn} and δ_{ik} in Eq. (3.2) are Kronecker delta functions.

3.3.2 Accumulation Model

Given the raw RF front-end samples from the n^{th} feed modeled in the previous subsection, in-phase and quadrature accumulations for the p^{th} satellite are calculated according to the following recipe:

$$I_p^n(\delta\omega_D, \delta\tau) + jQ_p^n(\delta\omega_D, \delta\tau) = \frac{1}{N_{acc}} \sum_{i=i_{p0}}^{i_{p0}+N_{acc}-1} y_i^n\ e^{-j(\hat{\omega}_{Dp}+\delta\omega_D)(t_i-t_0)} \times C_p[(1+\hat{\eta}_p)(t_i-\hat{\tau}_p-\delta\tau)] \tag{3.4}$$

The quantities $I_p^n(\delta\omega_D, \delta\tau)$ and $Q_p^n(\delta\omega_D, \delta\tau)$ are, respectively, the in-phase and quadrature accumulations using N_{acc} RF-front end samples, indexed from i_{p0} to $(i_{p0}+$

$N_{acc}-1$). These accumulations use the Doppler shift estimate $\hat{\omega}_{Dp}$, the non-dimensional code Doppler shift estimate $\hat{\eta}_p = \hat{\omega}_{Dp}/\omega_c$, and the PRN code period start time estimate $\hat{\tau}_p$. The accumulation formula includes the option of using a frequency offset $\delta\omega_D$ from $\hat{\omega}_D$ and a code start time offset $\delta\tau$ from $\hat{\tau}$. Accumulations will be calculated for multiple different frequency offsets $\delta\omega_D$ and for multiple difference code start time offsets $\delta\tau$ in order to make the carrier Doppler shift ω_{Dp} and the code start time τ_p observable.

For the remainder of the paper, the focus is on a single satellite. The low cross-correlation between PRN code at different satellites allows one to neglect the contribution of the signals from the rest of satellites. The subscript p is omitted in the following equations. In addition, the number of received signals, M, henceforth refers to the total number of direct and multipath signals for the satellite under consideration.

The accumulation recipe in Eq. (3.4) can be combined with the signal model in Eq. (3.1) in order to produce the following model of how the computed accumulations relate to the unknown signal parameters:

$$\begin{aligned} I^n(\delta\omega_D,\delta\tau)+jQ^n(\delta\omega_D,\delta\tau) = \sum_{m=1}^{M} & [\tilde{A}_{Rm}G_R^n(\theta_m,\phi_m)+\tilde{A}_{Lm}G_L^n(\theta_m,\phi_m)]\times \\ & R[(1+\hat{\eta})(\tau_m-\hat{\tau}-\delta\tau)]\times \\ & sinc(\frac{T_{acc}}{2}[\omega_{Dm}-\hat{\omega}_D-\delta\omega_D])e^{\frac{jT_{acc}}{2}\,[\omega_{Dm}-\hat{\omega}_D-\delta\omega_D]} \\ & +\tilde{v}_I^n(\delta\omega_D,\delta\tau)+j\,\tilde{v}_Q^n(\delta\omega_D,\delta\tau) \end{aligned} \tag{3.5}$$

The function $R(\tau)$ is the normalized auto-correlation function for the PRN code. The quantity T_{acc} is the accumulation interval. It corresponds to the sample time difference between the first and last samples used for the accumulation calculations, $N_{acc}\times\Delta t$.

The quantities $\tilde{v}_I^n(\delta\omega_D,\delta\tau)$ and $\tilde{v}_Q^n(\delta\omega_D,\delta\tau)$ are the in-phase and quadrature accu-

mulation noise terms. They can be derived from applying the accumulation formula in Eq. (3.4) to the raw noise terms from Eq. (3.1). They are zero-mean, Gaussian random quantities with the following statistics:

$$E[(\tilde{v}_I^n(\delta\omega_D,\delta\tau))^2] = E[(\tilde{v}_Q^n(\delta\omega_D,\delta\tau))^2] = \frac{\sigma_v^2}{N_{acc}} \tag{3.6}$$

$$E[\tilde{v}_I^m(\delta\omega_{Da},\delta\tau_a)\ \tilde{v}_I^n(\delta\omega_{Db},\delta\tau_b)] = \delta_{mn}\frac{\sigma_v^2}{N_{acc}}R[(\delta\tau_a-\delta\tau_b)(1+\hat{\eta})]\times sinc([\delta\omega_{Da}-\delta\omega_{Db}]\ T_{acc}) \tag{3.7}$$

$$E[\tilde{v}_Q^m(\delta\omega_{Da},\delta\tau_a)\ \tilde{v}_Q^n(\delta\omega_{Db},\delta\tau_b)] = \delta_{mn}\frac{\sigma_v^2}{N_{acc}}R[(\delta\tau_a-\delta\tau_b)(1+\hat{\eta})]\times sinc([\delta\omega_{Da}-\delta\omega_{Db}]\ T_{acc}) \tag{3.8}$$

$$E[\tilde{v}_I^m(\delta\omega_{Da},\delta\tau_a)\ \tilde{v}_Q^n(\delta\omega_{Db},\delta\tau_b)] = \delta_{mn}\frac{\sigma_v^2}{N_{acc}}R[(\delta\tau_a-\delta\tau_b)(1+\hat{\eta})]\times \frac{1-\cos[(\delta\omega_{Db}-\delta\omega_{Da})\ T_{acc}]}{(\delta\omega_{Db}-\delta\omega_{Da})\ T_{acc}} \tag{3.9}$$

The RHCP and LHCP signal phasors, $\tilde{A}_{Rm}$ and $\tilde{A}_{Lm}$, can be broken down into their real and imaginary parts:

$$\tilde{A}_{Rm} = A_{RIm} + jA_{RQm} \tag{3.10}$$

$$\tilde{A}_{Rm} = A_{LIm} + jA_{LQm} \tag{3.11}$$

The unknown parameter vector for the m^{th} signal is defined as

$$\underline{x}^m = \begin{bmatrix} \theta_m & \phi_m & \omega_{Dm} & \tau_m & A_{RIm} & A_{RQm} & A_{LIm} & A_{LQm} \end{bmatrix}^T \tag{3.12}$$

and the individual parameter vectors from all signals are combined together to form the large parameter vector for the full set of M signals:

$$\underline{x} = \begin{bmatrix} (\underline{x}^1)^T & (\underline{x}^2)^T & \dots & (\underline{x}^{M-1})^T & (\underline{x}^M)^T \end{bmatrix}^T \tag{3.13}$$

The accumulation models can be rewritten using the state vector:

$$\begin{aligned} I^n(\delta\omega_D, \delta\tau) + jQ^n(\delta\omega_D, \delta\tau) = h_I^n(\underline{x}, \delta\omega_D, \delta\tau) + jh_Q^n(\underline{x}, \delta\omega_D, \delta\tau) \\ + \tilde{v}_I^n(\delta\omega_D, \delta\tau) + j\,\tilde{v}_Q^n(\delta\omega_D, \delta\tau) \end{aligned} \tag{3.14}$$

$$\begin{aligned} \text{where} \quad h_I^n(\underline{x}, \delta\omega_D, \delta\tau) + jh_Q^n(\underline{x}, \delta\omega_D, \delta\tau) = \sum_{m=1}^{M} [\tilde{A}_{Rm} G_R^n(\theta_m, \phi_m) + \tilde{A}_{Lm} G_L^n(\theta_m, \phi_m)] \times \\ R[(1+\hat{\eta})(\tau_m - \hat{\tau} - \delta\tau)] sinc(\frac{T_{acc}}{2}[\omega_{Dm} - \hat{\omega}_D - \delta\omega_D]) e^{\frac{jT_{acc}}{2}\,[\omega_{Dm} - \hat{\omega}_D - \delta\omega_D]} \end{aligned} \tag{3.15}$$

The in-phase and quadrature accumulations from *2N* different feeds, N_{code} different code phase offsets $\delta\tau$ and N_{freq} different carrier Doppler shift offsets $\delta\omega_D$ can be lumped together to two vectors to form the complete measurement equation:

$$\underline{z} = \begin{bmatrix} h_I(\underline{x}) \\ h_Q(\underline{x}) \end{bmatrix} + \begin{bmatrix} \underline{v}_I \\ \underline{v}_Q \end{bmatrix} \tag{3.16}$$

The vectors $h_I(\underline{x})$, $h_Q(\underline{x})$, $\underline{v}_I$, and $\underline{v}_Q$ are defined as below:

$$\underline{h}_I = \begin{bmatrix} h_I^1(\underline{x}, \delta\omega_{D1}, \delta\tau_1) \\ \vdots \\ h_I^{2N}(\underline{x}, \delta\omega_{D1}, \delta\tau_1) \\ h_I^1(\underline{x}, \delta\omega_{D2}, \delta\tau_2) \\ \vdots \\ h_I^{2N}(\underline{x}, \delta\omega_{D2}, \delta\tau_2) \\ \vdots \\ h_I^1(\underline{x}, \delta\omega_{DN_{comb}}, \delta\tau_{DN_{comb}}) \\ \vdots \\ h_I^{2N}(\underline{x}, \delta\omega_{DN_{comb}}, \delta\tau_{DN_{comb}}) \end{bmatrix}, \quad \underline{h}_Q = \begin{bmatrix} h_Q^1(\underline{x}, \delta\omega_{D1}, \delta\tau_1) \\ \vdots \\ h_Q^{2N}(\underline{x}, \delta\omega_{D1}, \delta\tau_1) \\ h_Q^1(\underline{x}, \delta\omega_{D2}, \delta\tau_2) \\ \vdots \\ h_Q^{2N}(\underline{x}, \delta\omega_{D2}, \delta\tau_2) \\ \vdots \\ h_Q^1(\underline{x}, \delta\omega_{DN_{comb}}, \delta\tau_{DN_{comb}}) \\ \vdots \\ h_Q^{2N}(\underline{x}, \delta\omega_{DN_{comb}}, \delta\tau_{DN_{comb}}) \end{bmatrix} \tag{3.17}$$

$$\underline{v}_I = \begin{bmatrix} \tilde{v}_I^1(\underline{x}, \delta\omega_{D1}, \delta\tau_1) \\ \vdots \\ \tilde{v}_I^{2N}(\underline{x}, \delta\omega_{D1}, \delta\tau_1) \\ \tilde{v}_I^1(\underline{x}, \delta\omega_{D2}, \delta\tau_2) \\ \vdots \\ \tilde{v}_I^{2N}(\underline{x}, \delta\omega_{D2}, \delta\tau_2) \\ \vdots \\ \tilde{v}_I^1(\underline{x}, \delta\omega_{DN_{comb}}, \delta\tau_{DN_{comb}}) \\ \vdots \\ \tilde{v}_I^{2N}(\underline{x}, \delta\omega_{DN_{comb}}, \delta\tau_{DN_{comb}}) \end{bmatrix}, \quad \underline{v}_Q = \begin{bmatrix} \tilde{v}_Q^1(\underline{x}, \delta\omega_{D1}, \delta\tau_1) \\ \vdots \\ \tilde{v}_Q^{2N}(\underline{x}, \delta\omega_{D1}, \delta\tau_1) \\ \tilde{v}_Q^1(\underline{x}, \delta\omega_{D2}, \delta\tau_2) \\ \vdots \\ \tilde{v}_Q^{2N}(\underline{x}, \delta\omega_{D2}, \delta\tau_2) \\ \vdots \\ \tilde{v}_Q^1(\underline{x}, \delta\omega_{DN_{comb}}, \delta\tau_{DN_{comb}}) \\ \vdots \\ \tilde{v}_Q^{2N}(\underline{x}, \delta\omega_{DN_{comb}}, \delta\tau_{DN_{comb}}) \end{bmatrix} \tag{3.18}$$

Each ($\delta\omega_{Di}$,$\delta\tau_i$) pair in Eqs. (3.17-3.18) represents a unique combination of carrier Doppler shift offset and PRN code phase offset from each of the $N_{comb} = N_{code} \times N_{freq}$ total combinations. The effective total number of real-valued measurements is $(4N \times N_{code} \times N_{freq})$. The total number of unknown parameters is $8M$.

The noise covariance is defined as R_z, and it can be calculated from Eqs. (3.6-3.9):

$$E\{\begin{bmatrix} \underline{v}_I \\ \underline{v}_Q \end{bmatrix} \begin{bmatrix} \underline{v}_I{}^T & \underline{v}_Q{}^T \end{bmatrix}\} = R_z \tag{3.19}$$

3.4 Multipath Batch Estimator

This section develops the multipath batch estimator that solves an optimal batch estimation problem based on the accumulation measurement models from the previous section.

The weighted nonlinear least-squares batch estimation problem is to find a value of $\underline{x}$ that minimizes the following cost function:

$$J(\underline{x}) = \frac{1}{2}[\underline{z} - h(\underline{x})]^T R_z^{-1} [\underline{z} - h(\underline{x})] \tag{3.20}$$

$$\text{where} \quad h(\underline{x}) = \begin{bmatrix} h_I(\underline{x}) \\ h_Q(\underline{x}) \end{bmatrix} \tag{3.21}$$

The cost function in Eq. (3.20) equals the negative natural logarithm of the probability density function of the accumulation measurement vector conditioned on the values in the x vector, but with the natural logarithm of the probability density normalization constant removed. Minimization of this cost function amounts to maximum likelihood estimation.

This batch estimation problem is a weighted nonlinear least-squares estimation problem. The eventual solution algorithm will employ Gauss-Newton (GN) solution techniques. This iterative algorithm is like the Newton algorithm for nonlinear equation

solving, and like that algorithm, it requires a first guess. Given that the vector $\underline{x}$ has $8M$ elements, generating a reasonable first guess presents a challenge. This paper develops a staged method of building up a reasonable first guess. The first stage of this procedure uses standard GNSS signal acquisition techniques. The later stages are unique to the batch estimation problem at hand. Once a good first guess is found, it is straightforward to implement a Gauss-Newton minimizer for the batch least-squares cost function in Eq. (3.20).

3.4.1 Initial Coarse Acquisition of Carrier Doppler Shift and Code Delay

The initial coarse acquisition is a generalization of the brute-force search that is standard in GNSS receivers. A search is carried out over a grid of code delays $\hat{\tau}$ and carrier Doppler shifts $\hat{\omega}_D$. For each $(\hat{\tau},\hat{\omega}_D)$ candidate pair in the grid, in-phase and quadrature accumulations are generated according to Eq. (3.4) using $\delta\omega_D = 0$ and $\delta\tau = 0$. The accumulations from all antenna feeds are added non-coherently to form the following signal detection statistic:

$$\lambda(\hat{\omega}_D,\hat{\tau}) = \sum_{n=1}^{2N} [I^n(0,0)\Big|^2_{\hat{\omega}_D,\hat{\tau}} + Q^n(0,0)\Big|^2_{\hat{\omega}_D,\hat{\tau}}] \tag{3.22}$$

The carrier Doppler shift search ranges from -9 kHz to 9 kHz, with a grid spacing of half the accumulation frequency, π/T_{acc} rad/s. The code delay search range is the full PRN code period, with a grid spacing of the sampling period, Δt.

The test statistic $\lambda(\hat{\omega}_D,\hat{\tau})$ for each $(\hat{\tau},\hat{\omega}_D)$ candidate pair is compared against a given

detection threshold, λ_{min}, that is generated from a statistical analysis of the noise statistics as described in Eqs. (3.6-3.9). The ($\hat{\tau}$,$\hat{\omega}_D$) candidate with the highest λ value above the threshold is chosen as the result of the coarse acquisition. If the multipath code delay or Doppler shift (or both) have sufficiently large offsets for a strong multipath signal, then a second distinct acquisition peak will be visible. Its $\hat{\tau}$ and $\hat{\omega}_D$ values can be used to augment this paper's first guess procedure. The same holds true for a spoofing signal with large code delay or Doppler shift offset. Such problems are typically easier to solve. This paper's examples are all taken from multipath cases that produce only one distinct peak during coarse acquisition.

3.4.2 Estimation of Signal Phasors, Code Delay, Carrier Doppler Shift, and Direction of Arrival for one signal

The batch estimation of all signal parameters is seeded with the coarse acquisition estimates of the carrier Doppler shift and code delay. In-phase and quadrature accumulations are generated using these estimates over a grid of carrier Doppler shift and code phase offsets, $\delta\omega_D$ and $\delta\tau$, as in Eq. (3.4). The range of code phase offsets needs to be wide enough to cover potential peaks of the direct and multipath signals along the code phase axis. The code phase offset spacing is chosen such that close peaks of direct and multipath signals can be separated in the code phase. The cross-correlation of noise terms for accumulations with small code offset differences puts a limit on the improvement that can be achieved with a finer code phase grid. Similarly, the range of carrier Doppler shift offsets is chosen to encompass potential carrier Doppler shift values of the direct and multipath signals. Cross-correlation of noise terms limits the amount of extra information the filter can achieve with decreasing grid spacing in the

carrier Doppler shift. The resulting weighed nonlinear least-squares problem is solved by using a specially constructed numerical search that iteratively increases the number of signals.

The cost function optimization starts by assuming that the number of signals is one. A brute-force search is conducted over a co-elevation/azimuth grid (θ,ϕ) to find an initial estimate for the direction of arrival. This initial DOA search keeps the carrier Doppler shift and the code delay for the signal at their coarse acquisition estimates. The choice of grid spacing for the co-elevation and the azimuth grid is important to the performance of the estimator and will be discussed in the results section. At each point in the co-elevation/azimuth grid, an optimal set of RHCP and LHCP phasors is calculated. The phasor optimization can be carried out using standard matrix operations because the phasor components enter the signal model linearly. The (θ,ϕ) pair with the lowest cost as calculated using Eq. (3.20) and the associated phasor components are combined with the $\hat{\omega}_D$ and $\hat{\tau}$ estimates from the coarse acquisition to form an initial solution guess vector:

$$\underline{x}_0 = \begin{bmatrix} \bar{\theta} & \bar{\phi} & \hat{\omega}_D & \hat{\tau} & \bar{A}_{RI} & \bar{A}_{RQ} & \bar{A}_{LI} & \bar{A}_{LQ} \end{bmatrix}^T \tag{3.23}$$

The quantities $\bar{\theta}$, $\bar{\phi}$, $\bar{A}_{RI}$, $\bar{A}_{RQ}$, $\bar{A}_{LI}$, and $\bar{A}_{LQ}$ are, respectively, the co-elevation angle, the azimuth angle, and the phasor components from the DOA brute-force search. This initial solution guess is used to seed a Gauss-Newton nonlinear least-squares solver [29]. The resulting optimal estimate for $\underline{x}$ is designated as $\underline{x}_{opt,1}$ to indicate that it is the optimal solution with one signal.

3.4.3 Estimation of Signal Phasors, Code Delay, Carrier Doppler Shift, and Direction of Arrival for two signals

The optimal value of the cost function in Eq. (3.20) can be used to test the assumption that the current assumed number of signals is correct.

If the given number of signals is the same as the actual number, and if the optimal estimate from the Gauss-Newton nonlinear least-squares solver is close to the true state vector, then $2J(\underline{x}_{opt})$ can be approximated as being a sample from a chi-squared distribution with $(4N \times N_{code} \times N_{freq} - 8M)$ degrees of freedom. An upper bound for $2J(\underline{x}_{opt})$ is calculated to give a prespecified false alarm probability for the detection of added signals. If $2J(\underline{x}_{opt})$ is below this bound, then $\underline{x}_{opt,1}$ is the final estimate of the algorithm. If $2J(\underline{x}_{opt})$ exceeds the bound, then the assumed number of signals is incremented by one.

If the algorithm decides that there are 2 signals, then the brute-force search for DOA is repeated in a modified form. The co-elevation/azimuth grid is extended from a 2D grid to a 4D grid, with 2 azimuth angles and 2 co-elevation angles. At each grid point, the carrier Doppler shift and the code delay for the signals are set to the coarse acquisition estimates, and an optimal set of phasor components for all signals is calculated. Again, the phasors are optimized exactly by using the matrix method of linear least-squares because they all enter the problem linearly. Grid points that correspond to the same azimuth and co-elevation angles for both signals are not utilized because the 8-dimensional vector of RHCP and LHCP phasor components for the 2 signals becomes unobservable when the signals have the same direction of arrival. Thus, the brute-force search is conducted to find two different directions of arrival for the signals. These direction-of-arrival estimates are combined with the $\hat{\omega}_D$ and $\hat{\tau}$ estimates from the coarse acquisition to form an initial solution guess vector:

$$\underline{x}_0^m = \begin{bmatrix} \bar{\theta}_m & \bar{\phi}_m & \hat{\omega}_D & \hat{\tau} & \bar{A}_{RIm} & \bar{A}_{RQm} & \bar{A}_{LIm} & \bar{A}_{LQm} \end{bmatrix}^T \quad \text{for } m = 1,2 \tag{3.24}$$

$$\underline{x}_0 = \begin{bmatrix} (\underline{x}_0^1)^T & (\underline{x}_0^2)^T \end{bmatrix}^T \tag{3.25}$$

The quantities $\bar{\theta}_m$, $\bar{\phi}_m$, $\bar{A}_{RIm}$, $\bar{A}_{RQm}$, $\bar{A}_{LIm}$, and $\bar{A}_{LQm}$ are, respectively, the co-elevation angle, the azimuth angle, and the phasor components for the m^{th} signal from the DOA brute-force search. The initial solution guess in Eq. (3.25) is, again, used to seed a Gauss-Newton nonlinear least-squares solver. The new resulting optimal estimate for $\underline{x}$ is designated as $\underline{x}_{opt,2}$ to indicate that it is the optimal solution with 2 signals.

3.4.4 Estimation of Signal Phasors, Code Delay, Carrier Doppler Shift, and Direction of Arrival for more than two signals

As in the case of 1 signal, the validity of an M-signal estimate can be checked by comparing $2J(\underline{x}_{opt})$ to a false alarm upper bound based on chi-squared statistics for a degree $(4N \times N_{code} \times N_{freq} - 8M)$ distribution. If the bound is respected, them M is accepted as the true number of signals, and $\underline{x}_{opt,M}$ is accepted as the best estimate of their parameters. Otherwise, the number of signals is incremented by one and a new estimation problem is solved.

The DOA brute-force search for 2 signals described in the previous section can be generalized for any number of signals. The co-elevation/azimuth grid can be extended to a $2M$-dimensional grid, with M azimuth angles and M co-elevation angles. However, this DOA brute-force search for M signals can become very slow for $M > 2$. Given N_θ co-elevation angles and N_ϕ azimuth angles in the grid, there are $(N_\theta \times N_\phi)^M$ points in

the grid. Thus, the grid space is exponential in the assumed number of signals, and the DOA brute-force search rapidly becomes computationally infeasible as M grows above two.

An alternate method for seeding of the Gauss-Newton optimization starts with the optimal estimate from the $M-1$ signals case. Given the optimal estimate $\underline{x}_{opt,M-1}$, the measurement residuals are calculated as:

$$\underline{z}_{res,M-1} = \underline{z} - h(\underline{x}_{opt,M-1}) \tag{3.26}$$

The measurement residual vector, $\underline{z}_{res,M-1}$, is then used as though it were a raw measurement to search for the DOA of one signal as previously described for the $M=1$ case. Instead of keeping only the DOA with the lowest cost, all the local minima in the (θ,ϕ) grid are utilized. For each such pair, the optimal phasor components are calculated and then combined with the optimal estimate from the $M-1$ case to form an alternate initial solution guess vector for the M case:

$$\underline{x}_0^i = \left[\begin{array}{ccccccccc} \underline{x}_{opt,M-1}{}^T & \bar{\theta}_M^i & \bar{\phi}_M^i & \hat{\omega}_D & \hat{\tau} & \bar{A}_{RIM}^i & \bar{A}_{RQM}^i & \bar{A}_{LIM}^i & \bar{A}_{LQM}^i \end{array} \right]^T \tag{3.27}$$
$$for \quad i = 1, \cdots, n_{local}$$

where n_{local} is the number of local minima in the DOA grid. The quantities $\bar{\theta}_M^i$, $\bar{\phi}_M^i$, $\bar{A}_{RIM}^i$, $\bar{A}_{RQM}^i$, $\bar{A}_{LIM}^i$, and $\bar{A}_{LQM}^i$ are, respectively, the co-elevation angle, the azimuth angle, and the phasor components for the i^{th} local minimum from the DOA brute-force search. $\hat{\omega}_D$ and $\hat{\tau}$ are the values from the initial coarse acquisition. The initial solution guess vectors in Eq. (3.27) are separately used to seed the Gauss-Newton solver so that

n_{local} solutions are computed. The resulting optimal estimates are reduced to a single estimate by choosing the one with the lowest cost. This estimate is then designated as the optimal estimate for the case with M signals. One might be tempted to use only the global minimum from the initial DOA search for the M^{th} signal. This would seed just one GN search for $\underline{x}_{opt,M}$. Unfortunately, this approach often yields a local minimum of the M-signals batch estimation cost function, but not the global minimum. The development of n_{local} initial guesses and the execution of n_{local} GN searches provide a reliable means of finding the globally minimizing $\underline{x}_{opt,M}$.

Calculating the local minima in the DOA grid is non-trivial due to the azimuth periodicity and the co-elevation singularities at $\theta = 0$ and $\theta = 180$ degrees. A local minimum is defined as a grid point that has a cost lower than all of its neighboring grid points. The tricky aspect of determining local minima concerns the definition of a given point's neighbors. In general, a grid point (θ_i,ϕ_k) has 8 neighboring points that are characterized by the preceding, current, and following co-elevation angles, θ_{i-1}, θ_i, and θ_{i+1}, and by the preceding, current, and following azimuth angles ϕ_{k-1}, ϕ_k, and ϕ_{k+1}. These 8 neighboring points are $(\theta_{i-1},\phi_{k-1})$, (θ_{i-1},ϕ_k), $(\theta_{i-1},\phi_{k+1})$, (θ_i,ϕ_{k-1}), (θ_i,ϕ_{k+1}), $(\theta_{i+1},\phi_{k-1})$, (θ_{i+1},ϕ_k), and $(\theta_{i+1},\phi_{k+1})$. A point at the edge of the grid with azimuth angle 0 or $\phi_{k_{max}}$, has 5 neighboring points if the azimuth periodicity is not taken into account. The missing 3 points that would be neighboring points if the grid is wrapped around in the azimuth angle are added to the list of neighboring points when the local-minimum check is evaluated for this grid point. For a polar grid point $(\theta = 0^\circ,\phi = 0^\circ)$ or $(\theta = 180^\circ,\phi = 0^\circ)$, all points with the nearest co-elevation angle are considered as the only neighbors. Consistent with this treatment of the poles, each neighbor of a polar point has only 6 neighbors because the one polar point takes the place of the three neighbors that it would otherwise have for a neighboring co-latitude that was neither 0 nor 180 degrees. If the grid only extends to $\theta = 90$ degrees, then all the grid points with this

co-elevation angle have only 5 neighboring points because the neighboring grid points with the next higher co-elevation angle are missing from the grid.

The need to execute n_{local} GN searches is somewhat expensive computationally. Nevertheless, the cumulative amount of computation required by the multiple searches is typically much lower than the amount required to do a brute-force search simultaneously on 3 or more DOA grids.

3.4.5 Estimation Algorithm Summary

This paper's algorithm and its process of calculating the optimal solution can be summarized as follows:

1. Obtain estimates $\hat{\omega}_D$ and $\hat{\tau}$ from the initial coarse acquisition.
2. Set $M = 1$.
3. If $M < 3$, go to Step 4. Otherwise, go to Step 6.
4. Do a DOA brute-force grid search for M signals. Use the globally cost-minimizing solution to develop a seed for the Gauss-Newton solver.
5. Use the Gauss-Newton method to solve $\underline{x}_{opt,M}$. Go to Step 8.
6. Compute $\underline{z}_{res,M-1}$ as in Eq. (3.26) and do a DOA brute-force grid search for 1 signal, treating $\underline{z}_{res,M-1}$ as though it were $\underline{z}$. Combine $\underline{x}_{opt,M-1}$ with the multiple local minima of the cost function to seed the Gauss-Newton solver.
7. Use the Gauss-Newton method and each of the seeds developed in Step 6 to solve for candidate $\underline{x}_{opt,M}$, and choose the one with the lowest cost as $\underline{x}_{opt,M}$. Go to Step 8.

8. Decide if the assumed number of signals is correct using the test statistic $2J(\underline{x}_{opt,M})$. If so, terminate with the solution $\underline{x}_{opt,M}$. Otherwise, proceed to Step 9.

9. Increment M by one and go to Step 3.

3.4.6 Estimator Algorithm Limitations of System Motion

The estimator developed in this paper relies on the assumption that the DOA and the Doppler shift of a signal remain constant over the accumulation interval. In the case of a moving antenna array, these assumptions may not hold true, and the estimation algorithm's performance would be affected.

A constant velocity motion would not pose any problems for the estimator. Such a motion would cause an additional constant Doppler shift offset, and the estimator would be able to handle such a situation without any performance degradation because it estimates carrier Doppler shift. Linear acceleration of the array would cause a varying carrier Doppler shift. However, even a large acceleration such as 10g would not cause any issues for the system due to its short accumulation interval. Over a 10 ms accumulation interval, such an acceleration would cause a Doppler shift change of 5 Hz, and it would lead to a negligible power loss in the accumulators of around 0.01 dB.

Rotations of the array would cause varying DOA in the estimator during the accumulation interval. The main effect would be the spreading of signal power across different DOAs. The effective power loss can be calculated by considering the following two parameters for each feed:

$$G_1^n = \left|\left| \frac{1}{T_{acc}} \int_0^{T_{acc}} G^n[\theta(t), \phi(t)] dt \right|\right|^2 \tag{3.28}$$

$$G_2^n = \frac{1}{T_{acc}} \int_0^{T_{acc}} || \, G^n[\theta(t), \phi(t)] \, ||^2 dt \tag{3.29}$$

The integrals are taken over the accumulation interval, and the varying DOA is emphasized by the time-varying co-elevation and azimuth angles, $\theta(t)$ and $\phi(t)$. The ratio of $\frac{\sum_{n=1}^{2N} G_1^n}{\sum_{n=1}^{2N} G_2^n}$ is used as an indicator of the power loss as a result of the array rotation. In the absence of any rotation, this ratio is 0 dB. As the rotation rate increases, this ratio decreases from 0 dB monotonically, indicating the spreading of power across different DOAs and the inability of a single DOA to represent the calculated accumulations.

For this power loss analysis, the average co-elevation angle, $\bar{\theta}$, is varied from 0 deg to 75 deg, with a spacing of 15 deg. The average azimuth angle, $\bar{\phi}$, is varied from 0 deg to 315 deg, with a spacing of 45 deg. These average angles are related to the time-varying angles as follows:

$$\bar{\theta} = \frac{1}{T_{acc}} \int_0^{T_{acc}} \theta(t) dt \tag{3.30}$$

$$\bar{\phi} = \frac{1}{T_{acc}} \int_0^{T_{acc}} \phi(t) dt \tag{3.31}$$

Seven different rotation vectors defined in the antenna array's coordinate system are used: $\begin{bmatrix} 0 & 0 & 1 \end{bmatrix}^T$, $\begin{bmatrix} 0 & 1 & 0 \end{bmatrix}^T$, $\begin{bmatrix} 1 & 0 & 0 \end{bmatrix}^T$, $\begin{bmatrix} 1/\sqrt{2} & 1/\sqrt{2} & 0 \end{bmatrix}^T$, $\begin{bmatrix} 1/\sqrt{2} & 0 & 1/\sqrt{2} \end{bmatrix}^T$, $\begin{bmatrix} 0 & 1/\sqrt{2} & 1/\sqrt{2} \end{bmatrix}^T$, and $\begin{bmatrix} 1/\sqrt{3} & 1/\sqrt{3} & 1/\sqrt{3} \end{bmatrix}^T$. For each triplet of co-elevation, azimuth, and rotation vector, the ratio defined above is calculated for a given rotation vector magnitude. The lowest $\frac{\sum_{n=1}^{2N} G_1^n}{\sum_{n=1}^{2N} G_2^n}$ ratio among all considered triplets for a given rotation rate is taken as the worst power loss. This analysis has

been conducted for a RHCP signal, and a linear polarized signal of linear polarization orientations of 0, 45, 90, 135, and 180 deg in the plane perpendicular to the propagation vector. A rotation rate of up to 60 rad/s would cause a rotation of the antenna array by about one tenth of a cycle over the accumulation interval. This rotation rate has been found to induce power losses up to 2.5 dB in the accumulations among all combinations of DOA, rotation vector, and signal polarization.

An additional analysis has been conducted for the angular estimation errors caused by rotation of the array. Given the time-varying co-elevation and azimuth angles, $\theta(t)$ and $\phi(t)$, the average steering function for the n^{th} feed over the accumulation interval can be calculated as follows:

$$\bar{G}^n = \frac{1}{T_{acc}} \int_0^{T_{acc}} G^n[\theta(t), \phi(t)] dt \tag{3.32}$$

This method's optimal estimation calculations will determine a single pair of co-elevation and azimuth, $\hat{\theta}$ and $\hat{\phi}$, that matches the overall average steering vector as best as possible when input to the steering function assuming, that the angles stay static and by considering all the feeds together. The deviation from the average DOA, represented by the pair ($\delta\theta$,$\delta\phi$), is used to determine the DOA angular estimation errors that are induced by rotation:

$$(\hat{\theta}, \hat{\phi}) = \underset{(\theta,\phi)}{\operatorname{argmin}} \sum_{n=1}^{2N} \left|\left| G^n(\theta, \phi) - \bar{G}^n \right|\right|^2 \tag{3.33}$$

$$\delta\theta = \hat{\theta} - \bar{\theta} \tag{3.34}$$

$$\delta\phi = \hat{\phi} - \bar{\phi} \tag{3.35}$$

The Gauss-Newton method is used to determine $\hat{\theta}$ and $\hat{\phi}$. The average and maximum number of iterations required to converge to a solution were 5 and 9, respectively.

This angular estimation error analysis has been conducted over the same set of average DOA angles, rotation vectors, and signal polarizations used for the power loss analysis. The azimuth errors are normalized by multiplying them by $\sin\bar{\theta}$ to make proper comparisons between different average co-elevation cases. The results show that the worst angular error among all considered combinations is on the order of 0.1 deg for a rotation rate of 15 rad/s. This angular error rises rapidly as the rotation rate is increased from 15 rad/s. At rotation rates of 17.5, 18, 19, and 20 rad/s, the worst angular errors are, respectively, around 0.5, 5.5, 15, and 22 deg. The worst power loss has been found as 0.05 dB at a rotation rate of 20 rad/s. Thus, it appears that the angular estimation error rather than the power loss is the limiting factor in how much rotation the estimator can handle. A rotation rate of 17.5 rad/s with its negligible angular deviation of 0.5 deg is deemed as the upper limit of how much rotation the estimator can handle without performance degradation when using an accumulation interval of $T_{acc} = 0.010$ sec.

3.5 Truth-Model Simulation

A truth-model simulation has been used to synthesize measurement data for use in assessing the proposed estimator. The simulation produces measurements at the accumulation level, given by Eq. (3.5), rather than at the RF front-end sample level, given by Eq. (3.1).

An array with 6 patch antennas is considered. There are 2 feeds for each antenna in the array. The antennas are equally distributed on a circle with a radius of 4.1 cm. The boresight of each antenna is slanted at 35 degrees away from the center of the

array. Each antenna is modeled as a crossed dipole with additional attenuation below its horizon. The two feeds implement phased addition such that one feed yields perfect RHCP reception along the boresight while the other feed yields perfect LHCP reception along the boresight. At the horizon, this crossed dipole model yields linear polarization on both feeds. In theory, the polarizations reverse when exactly opposite the boresight, but attenuation in this direction implies that signals below the horizon with reversed polarization will be unimportant.

The received carrier-to-noise-density ratio is set at 45 dB-Hz in the RHCP feed for the direct signal when arriving along a given antenna's boresight. For other arrival angles and other feeds, the received carrier-to-noise-density ratio is typically lower. Multipath received carrier-to-noise-density ratios are also typically lower.

The accumulation model in Eq. (3.5) uses the following parameters. The accumulation interval is set $T_{acc} = 10$ ms. Three carrier Doppler frequency offsets are used, $\delta\omega_D = -\frac{\pi}{T_{acc}}$, 0, and $\frac{\pi}{T_{acc}}$ rad/s. The code start time offsets range from -1.5 to 1.5 chips, with a spacing of 0.1 chip so that $\delta\tau$ takes on the 31 possible values -1.5, -1.4, -1.3, ... , 1.5. In total, 93 unique combinations of carrier Doppler shift offset and PRN code phase offset are used. This results in 2232 accumulations, half of them in-phase and half of them quadrature, from a total of 12 different antenna feeds.

Three different sets of cases have been considered. The first one uses one signal, the second two signals and the last one three.

For the cases with one signal, 500 truth-model simulations have been run. For each simulation, the signal is right-hand circularly polarized, and the DOA, PRN code phase and the carrier Doppler shift have been randomized as follows: The DOA has been sampled from a random uniform distribution with a maximum possible co-elevation angle of

75 degrees. The PRN code phase has been sampled from a random uniform distribution with a minimum value of 4×10^{-6} seconds and a maximum value of 6×10^{-6} seconds. The carrier Doppler shift has been sampled from a random uniform distribution with a range (0,100) Hz. For each simulation, the accumulation measurement noise is randomized. These 1-signal simulations are used to test the algorithm's ability to recognize the absence of multipath signals.

For the cases with two signals, the angle between the DOA's of the direct signal and the multipath signal has been varied to test the limits of how close the two signals can be in terms of the DOA before this paper's algorithm fails to distinguish them. For each considered angle pair, 500 truth-model simulations have been run and the estimation algorithm has been used to compute the number of signals and the corresponding parameters in the $\underline{x}$ vector. The accumulation measurement noise is randomized for each of the 500 simulations.

Table 3.1 shows the signal parameters used in the truth-model simulations for the cases with two signals. The second and third columns document the DOA angles for the two signals. The direction separation between the two signals is achieved by varying the azimuth of the multipath signal. Seven used values of the multipath azimuth result in an angle of separation of, respectively, 0, 2, 4, 6, 10, 15, and 20 degrees between the two signals. The polarizations for the direct signal and the multipath signal are set to, respectively, right-hand circular polarization and linear polarization, as indicated by the fourth column. The fifth column shows the power of the multipath signal relative to the direct signal. The final two columns describe, respectively, the PRN code phase and the carrier Doppler shift differences between the two signals.

Note that linear polarization of the multipath signal has been achieved by setting $\tilde{A}_{Rm} = \tilde{A}_{Lm}$. This has the effect of orienting the electric field direction in the plane

defined by the propagation direction and the antenna boresight. At the multipath co-elevation angle $\theta = 45$ degrees, the particular physical orientation of the multipath signal's linear polarization does not have a large effect on the estimation performance. At the antenna horizon, $\theta = 90$ degrees, the direction of linear polarization can have a large impact.

One challenge in multipath estimation is to distinguish between the direct signal and the multipath component with very little code phase offset. This challenge is particularly difficult if the receiver electronics tend to blunt the sharp peak in the original PRN code's auto-correlation function. Therefore, it is necessary to model this effect in order to probe this aspect of multipath estimation. The simulations model the effects of the limited RF front-end bandwidth on the accumulations. This is accomplished by defining $R(\tau)$ in Eq. (3.5) to be the cross-correlation between a wide-bandwidth exact replica of the PRN code and the filtered PRN code as received at the output of the RF front-end. Figure 3.1 shows this simulated PRN cross-correlation function for a range of bandwidth values. The green dash-dotted line shows the ideal auto-correlation function that is expected from an infinite bandwidth. The red dashed line, the blue dotted line, and the black solid line describe the cross-correlation function for bandwidths of 4, 2, and 1.5 MHz, respectively. A limited bandwidth is simulated by smoothing the auto-correlation function at $\tau = 0$ and $\tau = \pm 1$ chips. This is achieved by replacing portions of the ideal auto-correlation function centered at these three code delays. The width of the replaced portions are inversely proportional to the bandwidth. A cubic spline fills in the gaps to make the cross-correlation function continuous, with continuous first derivative. As

Signal	θ (deg)	ϕ (deg)	Polarization	Rel. Power	$\Delta\tau$ (chips)	$\Delta\omega_D$ (Hz)
Direct	45	25	RHC	-	-	-
Multipath	45	variable	Linear	-3 dB	0.2	5

Table 3.1: Signal parameters for the cases with two signals

a result, the sharp auto-correlation peak and the abrupt bends at $\tau = \pm 1$ chips become more rounded with decreasing bandwidth. For the truth-model simulations, an RF front-end bandwidth of 2 MHz has been used, and the PRN cross-correlation function is set to the one shown as the blue dotted line in Fig. 3.1.

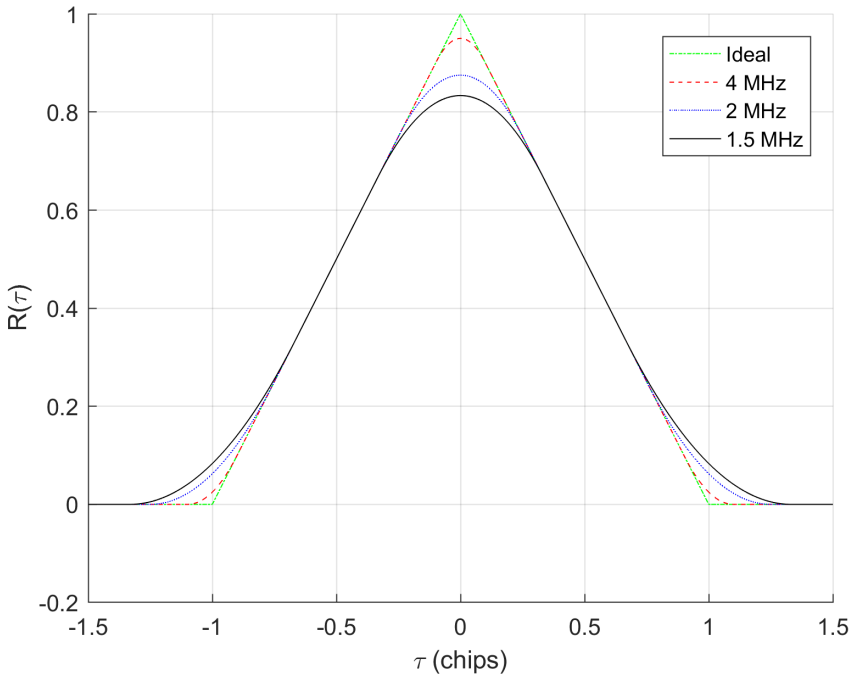

Figure 3.1: *Simulated PRN auto-correlation function for different RF front-end bandwidths*

Table 3.2 show the signals parameters used in the truth-model simulations for the cases with three signals. The column structure is the same as in Table 3.1. The second and third columns indicate the use of only one combination of DOA for the three signals. The fourth column indicates that both multipath signals are linearly polarized. The power of the second multipath signal is varied from -3 to -10 dB relative to the direct signal, with a spacing of 1 dB, consistent with the third line of the fifth column. This set of power levels is used to test the efficacy of the incremental signal search used in the algorithm for 3 or more signals. For each third signal power, 500 truth-model simulations have been run. The accumulation measurement noise is randomized for

each run.

A test has been conducted to evaluate the improvement in estimating the direct signal's parameters using this paper's algorithm. It compares the filter's results when estimating only the direct signal to the results where the filter decides automatically how many multipath signals to estimate. It is expected that the direct-signal-only ($M = 1$) results should be less accurate than the results where the filter estimates detected multipath signals. Two additional sets of 500 simulations have been run for these tests. For each set, the direct signal's parameters are kept the same, as shown in Table 3.1. The first set contains a single multipath signal, and the second set 2 multipath signals. The multipath signal parameters for all runs are chosen randomly. The multipath signals are linearly polarized, and their DOA, PRN code phase and carrier Doppler shift have been randomized as follows: The DOA has been sampled from a random uniform distribution with a maximum possible co-elevation angle of 75 degrees. The PRN code phase has been sampled from a random uniform distribution such that the multipath signal is between 0.1 chips and 0.5 chips later than the direct signal. The carrier Doppler shift has been sampled from a random uniform distribution such that the multipath value is within ± 50 Hz of the direct signal carrier Doppler shift. This range spans the Nyquist range of the accumulation frequency. The multipath signal power is uniformly randomized between -2 to -6 dB relative to the direct signal power. For each simulation, the accumulation measurement noise is randomized. In addition to the final $\underline{x}_{opt}$ from the algorithm for $M > 1$, each $\underline{x}_{opt,1}$ is also stored to evaluate errors when the algorithm limits itself to

Signal	θ (deg)	ϕ (deg)	Polarization	Rel. Power	$\Delta\tau$ (chips)	$\Delta\omega_D$ (Hz)
Direct	45	25	RHC	-	-	-
Multipath #1	65	25	Linear	-3 dB	0.2	5
Multipath #2	50	190	Linear	variable	0.3	4

Table 3.2: Signal parameters for the cases with three signals

finding only the direct signal.

3.5.1 Estimator Tunings

The upper bound for the test statistic $2J(\underline{x}_{opt})$ must be set to a reasonable value for deciding whether to search for an additional signal. This bound is set to a value that gives an expectation that the test statistic will fall below its value 99.5% of the time for a solution with the correct number of signals.

For the initial DOA search, the nominal grid spacing for both the co-elevation and azimuth angles is set to 18 degrees. The co-elevation angle ranges from 0 to 90 degrees. These grid spacings are used for the 1-signal search and for the 2-signals search. A latter study considers the effect of changing the spacing.

The bandwidth of the PRN code assumed by the estimator is 2 MHz for most cases. This matches the truth-model simulation bandwidth. In one special study, however, the estimator model uses bandwidths that range from 1.7 MHz to 2.5 MHz.

3.6 Performance When Applied to Data From Truth-Model Simulations

Several important questions about this system has been studied using data from the truth-model simulation. These include the following: how well does the method identify the correct number of signals? When the correct number of signals is identified, how accurate are the system's estimates of each signal's 8 parameters? Is the accuracy consistent with the predicted accuracy based on the batch filter's computed covariance?

In cases when the estimated number of signals is wrong, are the estimates of the direct path signal parameters accurate?

This section's initial subsection presents results for an example case with one signal. The next three subsections present Monte-Carlo statistics for cases with one, two, and three signals. The fifth subsection compares the errors for the direct signal's parameters using this paper's algorithm to the errors obtained when the algorithm estimates only the direct signal, ignoring any possible multipath signals. The sixth subsection considers the effect of unmodeled RF front-end filter distortion. The final subsection explores the issue of DOA search grid spacing.

3.6.1 Example Case With Only The Direct Signal

This subsection analyzes the results from a single simulation with only the direct signal present. This simulation has the following signal parameters: $\theta = 70.2$ deg, $\phi = 6.9$ deg, $\tau = 4.4 \times 10^{-6}$ seconds, and $\omega_D = 34.8$ Hz. The algorithm's optimal estimate produces a value of 2115 for the test statistic $2J(\underline{x}_{opt})$ with $M = 1$. This value is lower than the bound for the 1-signal search, 2400; so, the algorithm successfully determines that there is only one signal present. The optimal estimate $x_{opt,1}$ is compared against the truth values to calculate the estimation error in the 8 estimated quantities. The calculated errors can also be compared to the estimator 1-σ values obtained from the filter covariance matrix to assess how well the predicted errors in the estimated parameters match the actual errors.

The optimal estimate has error values of 0.19 and -0.26 degrees for the co-elevation and azimuth angles, respectively. The filter has been able to successfully estimate the direction-of-arrival. The filter 1-σ values for the co-elevation and the azimuth angles

are 0.18 and 0.21 degrees, respectively. These values are commensurate to the actual errors, and thus the filter has a very good idea about the accuracy of its DOA estimates.

The error in ω_D is 0.69 Hz, and the error in τ is 7.5×10^{-4} chips. The filter 1-σ values are 0.90 Hz and 0.0019 chips, respectively. The carrier Doppler frequency error and filter 1-σ values are comparable in magnitude, but the 1-σ τ value is an order of magnitude larger than the actual error. The filter appears to be conservative in its accuracy estimates for ω_D and τ, but data from a sample truth-model simulation can not adequately assess conservatism.

The errors in phasor components are 0.005, -0.023, -0.001, and -0.003 for A_{RI}, A_{RQ}, A_{LI}, and A_{LQ}, respectively. Note that the true A_{RI} and A_{RQ} are on the order of 1, while the true A_{LI} and A_{LQ} are zero. Thus, these errors are small relative to the signal amplitude. The filter 1-σ values for these parameters are 0.011, 0.026, 0.004, and 0.004, respectively. The filter 1-σ values and the actual errors are very close in size. The difference between the estimated RHCP power and the estimate LHCP power is 49 dB. This large power difference verifies that the estimator is able to correctly identify the polarization of the direct signal.

3.6.2 Results from the Cases with One Signal

This subsection analyzes the results from the 500 simulations with one signal. When the filter has $M = 1$, 0.4% of the 500 simulations produces a test statistic value that exceeds the specified bound for deciding whether there is more than one signal. For the other 498 simulations, the filter has successfully concluded that there is only one signal present. This observed false alarm rate is consistent with the 99.5% rate expected from the bound set for the test statistic.

For the simulations that have identified the correct number of signals, root-mean-square (RMS) error values are calculated for the signal parameters using the differences between the simulated truth-values and the filter estimates. In addition, the maximum value of the absolute error over all the simulations is calculated for each signal parameter to observe the worst performance of the estimator.

For the co-elevation angle, the RMS error is 0.20 degrees and the maximum error is 0.72 degrees. The filter 1-σ values for the co-elevation angle range from 0.14 to 0.26 degrees. The filter 1-σ values are close to the observed RMS error. The maximum error is observed in a simulation that has produced the largest 1-σ value and is within the 3-σ value (0.78 degrees) for that simulation.

The RMS error in the azimuth angle is 0.36 degrees. The maximum error is 5.06 degrees. The filter 1-σ values show a much wider range for the azimuth angle than for the co-elevation angle. The filter 1-σ values and the actual absolute errors are depicted by red circles and blue x's, respectively, in Fig. 3.2. The horizontal axis in this figure is the true co-elevation angle from the simulation. The filter 1-σ values are comparable to the observed errors in magnitude and the filter reports the highest 1-σ value when the largest actual error is observed. Note how the largest azimuth error and the largest filter 1-σ occur near the lowest co-elevation angles. This is expected because azimuth observability decreases to zero as co-elevation decreases to zero. Azimuth has no meaning at zero co-elevation. Overall, the filter's accuracy estimates are consistent with the observed errors.

The RMS carrier Doppler shift error is 0.72 Hz. The maximum error is 2.49 Hz. The filter 1-σ error values range from 0.60 Hz to 0.98 Hz. Overall, the filter accuracy estimates are consistent with the observed errors of the simulations. Similarly, the RMS PRN carrier phase error is 0.0015 chips, and the maximum error is 0.0047 chips. The

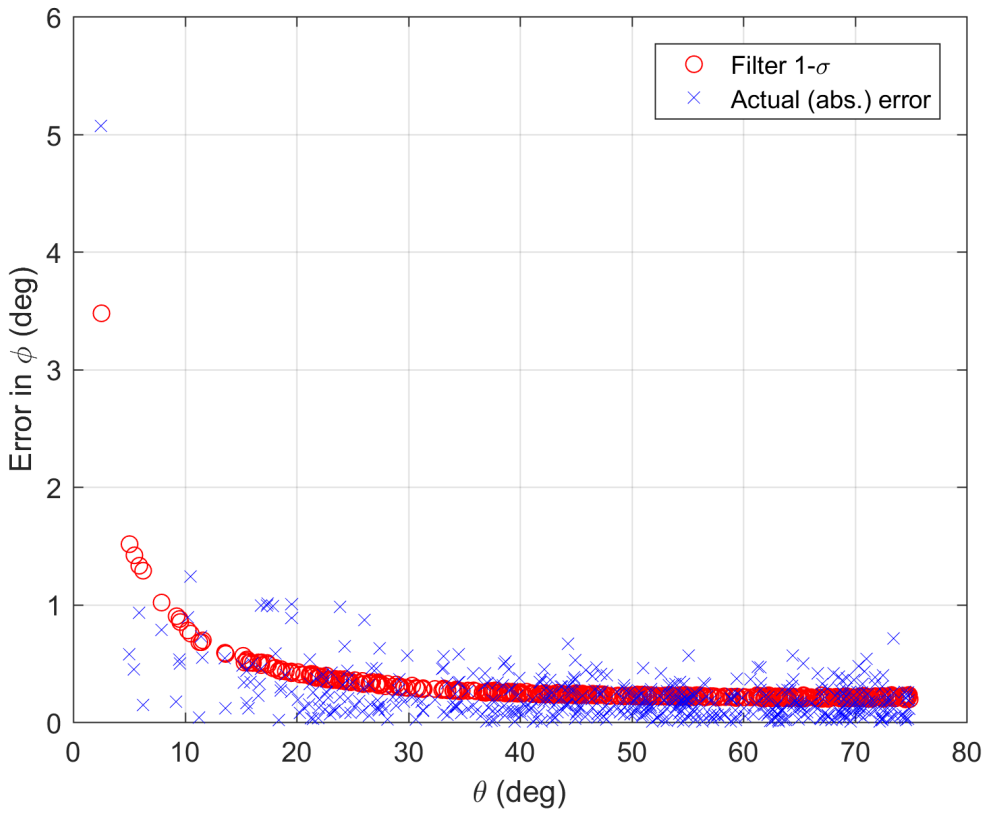

Figure 3.2: *Azimuth error comparison for the cases with one signal*

filter 1-σ error values are in the range 0.0021-0.0047 chips. The predicted filter accuracy for the code phase is consistent with the observed errors.

In terms of the polarization, the difference between the estimated RHCP power and the estimated LHCP power ranges from 37 dB to 88 dB. This large power difference between the RHCP and LHCP phasors show that the filter successfully captures the RHCP nature of the signal for all the runs.

The two runs that produce the false alarm cases both result in an optimal filter estimate with 2 signals. The power difference between the 2 estimated signals are 27 and 24 dB, respectively, in these two runs; so, the final filter solution consists of one signal with the expected direct signal power and a very weak second signal. In one of these

runs, the filter-labeled direct signal parameters match well with the true parameters. The estimation errors are 0.77 and 1.84 degrees, respectively, for the co-elevation and the azimuth angles. The error in ω_D estimate is 0.78 Hz. The error in τ_D estimate is 9×10^{-4} chips. The power ratio of RHCP to LHCP phasors for the direct signal is 26 dB. The filter captures the RHCP nature of the signal correctly.

The other run that produces a false alarm case fails in designating the correct signal as the direct signal. The filter has labeled the fairly weak second signal as the direct signal because the τ estimates for the two signals put the weak signal as the earlier signal. The resulting errors are quite large as expected. The filter errors are -10 degrees, 197 degrees, -106 Hz, and -0.04 chips for θ, ϕ, ω_D, and τ, respectively. This shows a complete failure to estimate parameters of the only signal present for this run. The filter can be modified to label the signal with the most power as the direct signal. If the estimated signal with the larger power from this run is designated as the direct signal and its parameters are used to calculate the estimation errors, then the estimator performance improves drastically in terms of the observed errors. The errors, with this modification, are 0.56 degrees, 0.12 degrees, 0.26 Hz and 0.002 chips for θ, ϕ, ω_D, and τ, respectively. This result shows that for this run the filter actually has a good estimate for the parameters of the direct signal, but the failure to label the correct signal as the direct signal results in the large error values reported above. Nevertheless, in certain scenarios that involve attenuation of the direct signal, the multipath signal components can have bigger powers than the direct signal. In those scenarios, the modification to label the signal with the most power as the direct signal would lead to erroneous results.

Similarly, the polarization estimates can be used to designate the direct signal. For the first false alarm case, the estimated power ratio of RHCP to LHCP phasors is 26 and 3 dB, respectively, for the correctly-identified direct signal and the additional weaker

signal. For the second false alarm case with the signal identification failure, the estimated power ratio of RHCP to LHCP phasors is 51 dB and 3 dB for, respectively, the more powerful signal that produces the small error values discussed above and the weaker signal that produces the large error values. In both cases, the signal whose estimated parameters are close to the truth signal parameters is clearly right-hand circularly polarized, whereas the other weak signal is closer to linearly polarized than right-hand or left-hand circularly polarized. Thus, if the algorithm is modified to designate the signal with a clear right-hand circular polarization as the direct signal, then it would label the correct signal as the direct signal in both cases. A future modification to the algorithm's method of choosing the direct signal among the estimated signals would incorporate both the estimates for signal power levels and polarizations.

3.6.3 Results from the Cases with Two Signals

This subsection analyzes the results from the cases with two signals. When the filter has $M = 1$, the filter is able to conclude that there must be more signals for all 500 runs of each of the 7 cases. Recall that the 7 cases are distinguished by the 7 different azimuth angles of the multipath signal. For all the runs, the calculated test statistic remains well above the bound (2400 for 1 signal), with an observed minimum of 4392 for the test statistic over all runs. When the filter has at most $M = 2$, 0.2% of the 500 runs for each case produces a test statistic value that exceeds the bound for 2 signals (2391). This false alarm rate shows little variation with the changing angle between the two signals' DOA.

RMS errors for all the cases are calculated over the runs that identified the correct number of signals by comparing the filter estimates against the simulated true values.

Figures 3.3-3.6 show 500-run RMS error, maximum error, and filter's computed 1-σ values for θ, ϕ, ω_D, and τ, respectively. For all 4 figures, the RMS errors are shown by red stars for the first signal (the direct signal) and black diamonds for the second signal (the multipath signal). The maximum errors are shown by blue crosses (first/direct) and red x's (second/multipath). The predicted 1-σ values from the filter covariance matrix are depicted with magenta squares (first/direct) and black circles (second/multipath). Overall, for all of these 4 quantities, the predicted 1-σ errors match quite well with the actual observed RMS errors, as seen by the overlap of the symbols used for the RMS error and the 1-σ filter values. This result confirms the consistency of the filter in predicting the accuracy levels of its estimates. The RMS values do not show any significant variations with the DOA azimuth angle. The co-elevation RMS errors are around 0.3 and 0.4 degrees for the two signals, respectively. The azimuth RMS errors are around 0.4 and 0.6 degrees, respectively. The RMS carrier Doppler shift errors are around 1.0 and 1.4 Hz, respectively. Finally, the RMS PRN code phase errors are around 0.004 and 0.005 chips, respectively. The maximum observed error in the code phase is 0.02 chips. Given that the code phase difference between the two signals is 0.2 chips, a maximum error of 0.02 chips in the code phase estimates means that the filter has been able to successfully label the correct signal as the direct signal through the use of code phase estimates, even when the two DOAs are identical. For all 4 parameters, RMS errors, maximum errors, and filter 1-σ values are consistently lower for the direct signal than the multipath signal. This is consistent with the fact that the direct signal has 3 dB more power.

The ability to estimate polarization can be evaluated by considering the estimated power ratio of the RHCP component to the LHCP component for the two signals. It should be very large for the direct signal and 1 for the multipath signal. The RHCP signal component is estimated to be 25 to 73 dB more powerful than the LHCP signal

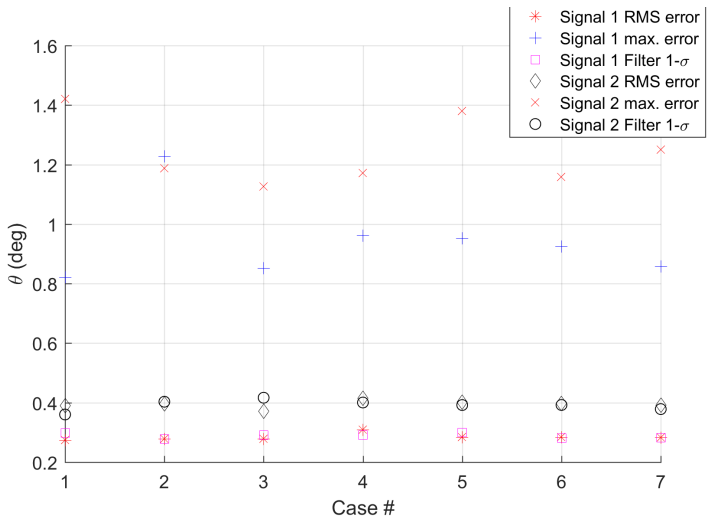

Figure 3.3: *Co-elevation estimation error values for the cases with two signals*

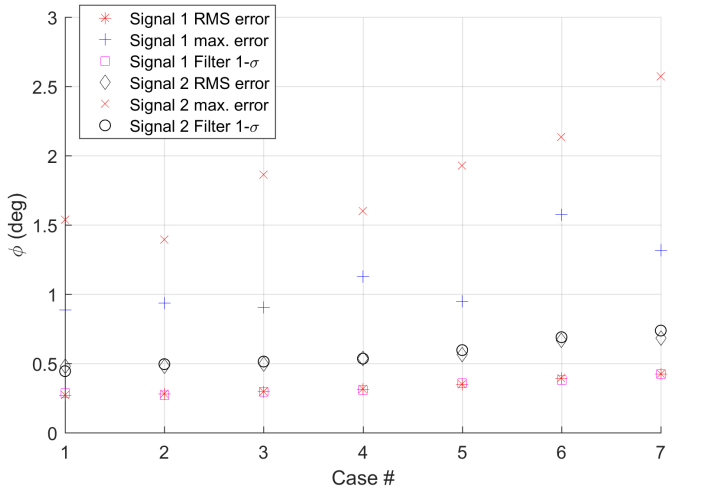

Figure 3.4: *Azimuth estimation error values for the cases with two signals*

component for the direct signal over all the runs. Thus, the filter successfully identifies the right-hand circular polarization of the direct signal. Similar calculations for the multipath signal show a range of -1.31 dB to 1.17 dB for the ratio of the RHCP and LHCP amplitude estimates. Figure 3.7 shows a histogram of this ratio using data from all the runs. The true power ratio is 0 dB for all the runs since the multipath signal is linearly polarized and the estimated amplitudes are close to this true value for all runs indicating good identification of the multipath signal's linear polarization.

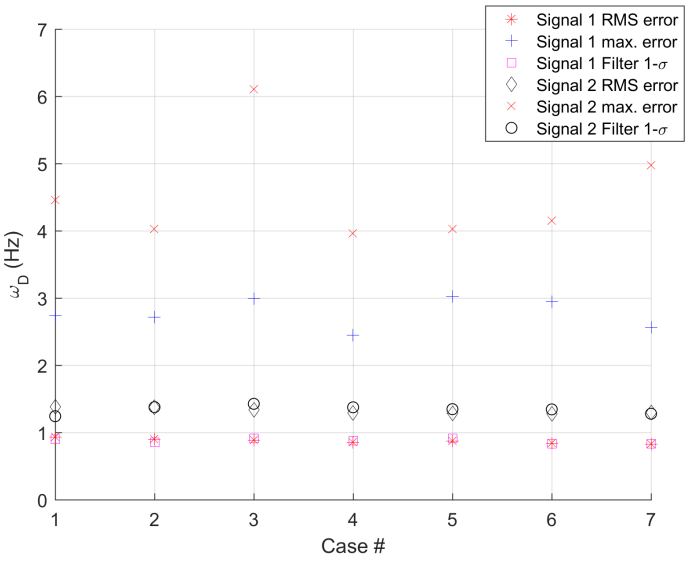

Figure 3.5: *Carrier Doppler shift estimation error values for the cases with two signals*

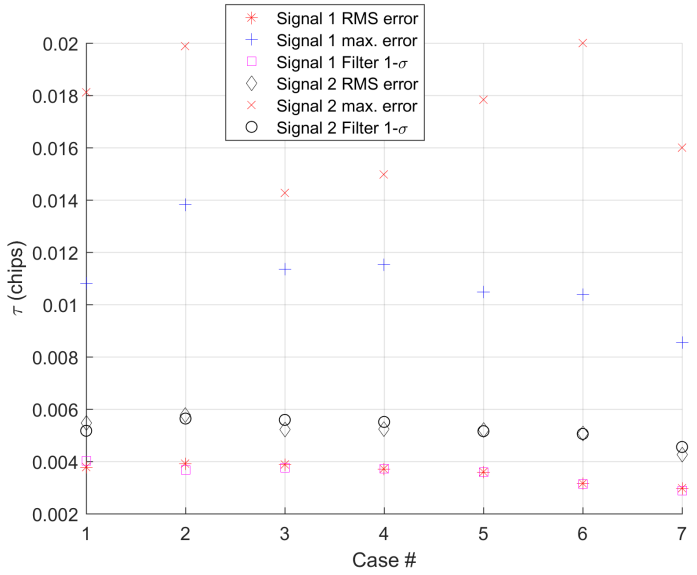

Figure 3.6: *PRN code phase estimation error values for the cases with two signals*

For the runs where the filter fails to identify two as the correct number of signals, it concludes that there are three signals. The filter fails to find the direct signal in every one of these runs. None of its three signal estimates is anything like the true direct signal. Thus, the filter estimates for the direct signal parameters are very poor. Such occurrences could be reduced or eliminated by raising the statistical test bound for deciding whether

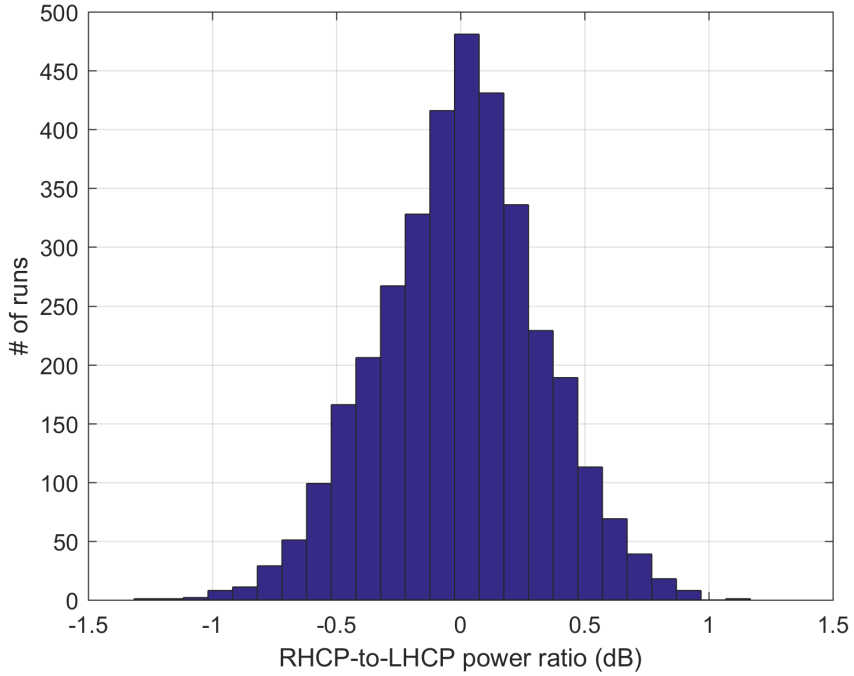

Figure 3.7: *Histogram for the RHCP to LHCP power ratio estimates for the multipath signal, for the cases with 2 signals*

an extra signal is present. Instead of a 99.5% bound, one could use a 99.95% bound. Of course, this might cause the algorithm to decide that there are only two signals when there are actually three. The question of how best to set this bound remains open.

3.6.4 Results from the Cases with Three Signals

This subsection analyzes the results from the cases with three signals. When the filter is considering the one-signal hypothesis and the two-signals hypothesis, it is able to conclude that there must be more signals for all the runs of all the cases. The calculated test statistic remains well above the extra-signal detection bound (2400 for 1 signal and 2391 for 2 signals), with an observed minimum of 11991 for 1 signal and 4082 for 2 signals, for the test statistic over all runs. One might have expected failures to detect

the third signal when it was 10 dB down from the direct signal and 7 dB down from the first multipath signal, as in one of the 8 cases. These results indicate that the 3^{rd} signal must be even weaker to cause detection failure. When the filter has $M = 3$, at most 0.4% of the 500 runs produces a test statistic value that exceeds the detection bound for an additional signal. Figure 3.8 shows the false alarm rates for all cases with three signals. Recall that each case is a set of 500 simulations with a different relative power of the 2^{nd} multipath signal. The false alarm rate remains within the expected value of 0.5% for all the cases, regardless of the relative power of the second multipath signal.

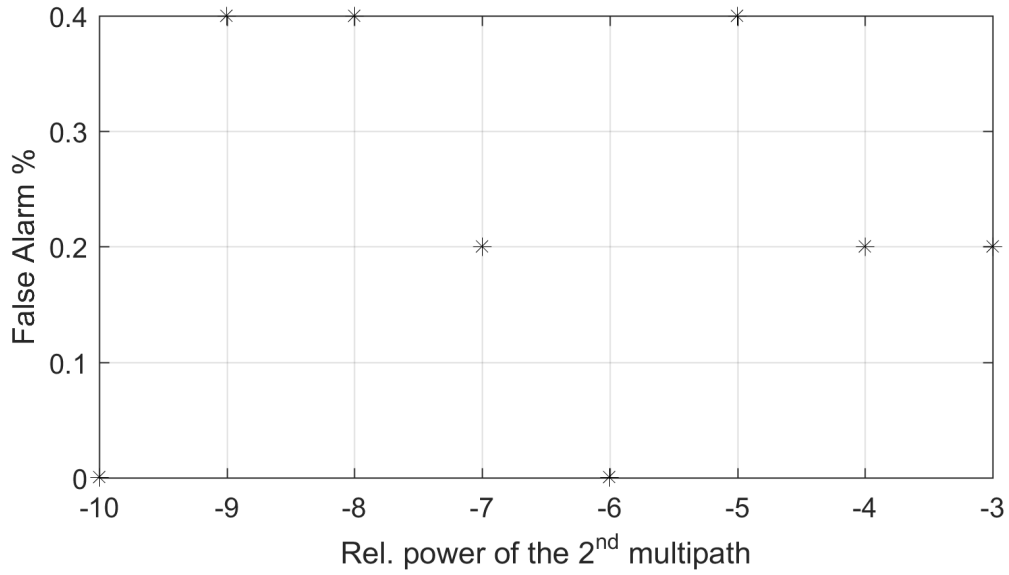

Figure 3.8: *False Alarm rates for the cases with three signals*

Figures 3.9-3.12 show the RMS error, the maximum error, and the computed filter 1-σ values for θ, ϕ, ω_D, and τ, respectively. As in Fig. 3.8, the horizontal axis indicates the case in terms of the power level of the second multipath signal relative to the direct signal. For all 4 figures, the RMS errors are shown by red stars for the first signal (the direct signal), black diamonds for the second signal (the first multipath signal), and black triangles pointing up for the third signal (the second multipath signal). The maximum errors are shown by blue crosses (first), red x's (second), and blue triangles

pointing down (third). The predicted 1-σ values from the filter covariance matrix are depicted with magenta squares (first), black circles (second), and red triangles pointing right (third). Similar to the cases with two signals, the filter 1-σ values match well with the actual RMS errors. The actual accuracy levels are consistent with the predicted levels.

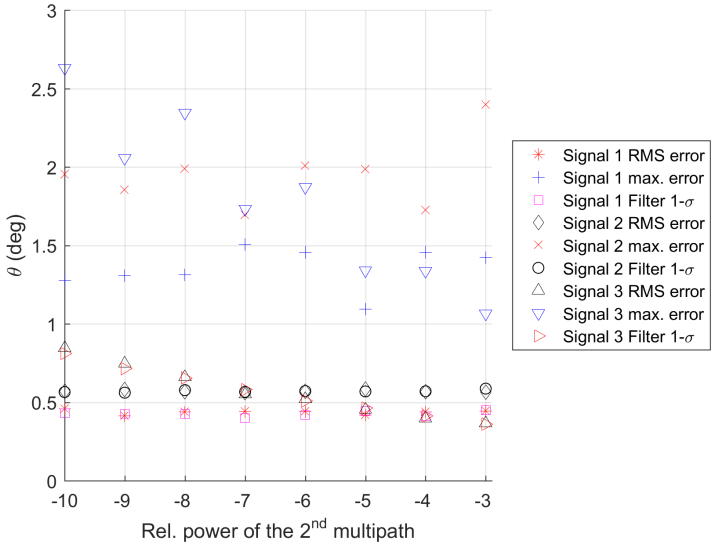

Figure 3.9: *Co-elevation estimation error values for the cases with three signals*

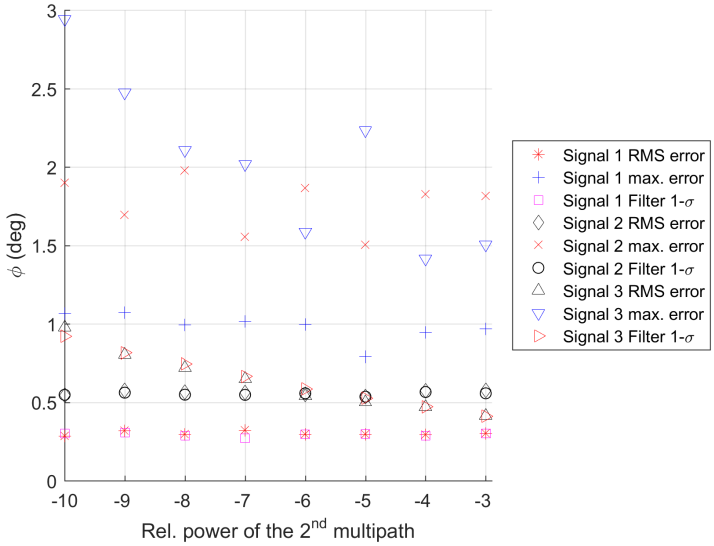

Figure 3.10: *Azimuth estimation error values for the cases with three signals*

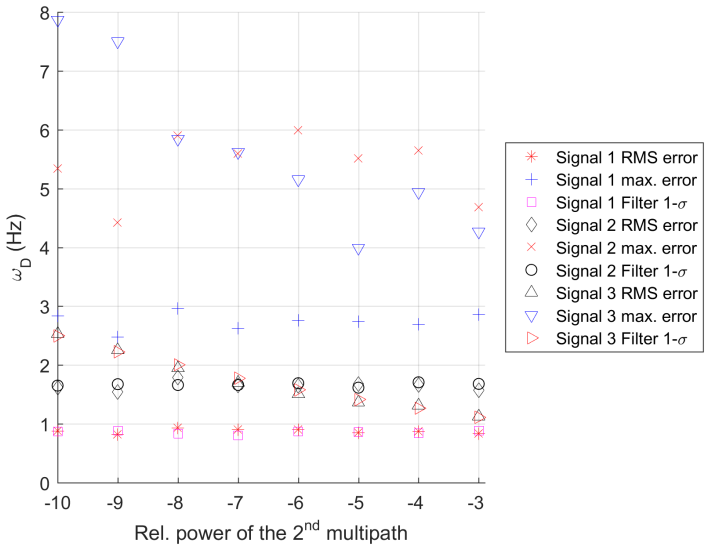

Figure 3.11: *Carrier Doppler shift estimation error values for the cases with three signals*

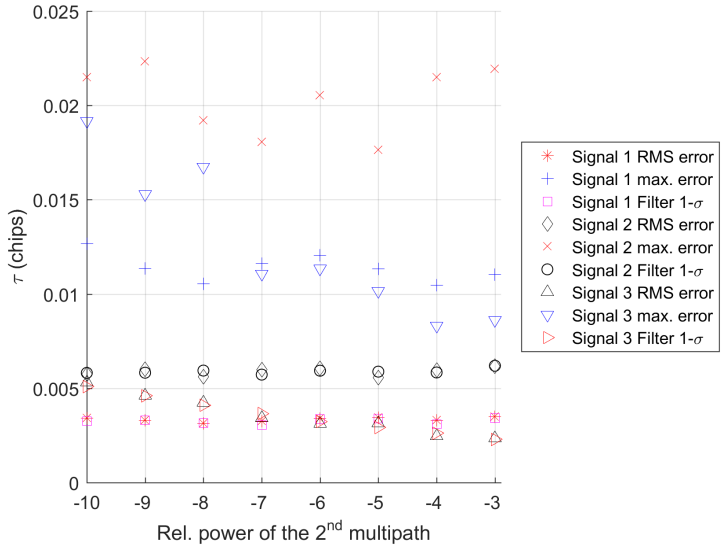

Figure 3.12: *PRN code phase estimation error values for the cases with three signals*

The RMS error values for the direct signal and the first multipath signal show little variance with the changing power of the second multipath signal. The RMS errors for the direct signal are 0.4 degrees, 0.3 degrees, 1 Hz, and 0.004 chips, respectively, for θ, ϕ, ω_D, and τ. These error values are similar to the ones observed for the cases with 2

signals. The RMS error values for the second multipath signal decrease with increasing power in the second multipath signal for all the shown parameters. The observed RMS errors in the PRN code phase are significantly smaller than the truth code phase differences between the 3 signals. This means that the filter has been able to successfully label the correct signal as the direct signal by considering their relative code phases.

The RHCP signal component is estimated to be 26 to 90 dB more powerful than the LHCP signal component for the direct signal over all the runs. Thus, the filter successfully identifies the right-hand circular polarization of the direct signal. Similar calculations for the first and the second multipath signals show, respectively, a range of -1.51 dB to 1.30 dB, and a range of -0.54 dB to 0.59 dB for the ratio of the RHCP and LHCP power estimates. The power ratios for both of the multipath signals show a histogram similar to the one shown in Figure 3.7. The true power ratio is 0 dB for all the runs since the multipath signals are linearly polarized. For the majority of the runs, the estimated power ratios are close to this true value. The observed maximum estimation errors of ± 1.5 dB for this power ratio indicates success in identifying the linear polarization of the multipath signals.

For the runs where the filter fails to identify three as the correct number of signals, it concludes that there are four signals. Similar to such cases with two signals when the filter has identified a wrong number of signals, the filter fails to find the direct signal. The problem is not one of choosing among the several signal estimates to find the one that is actually the direct signal. None of the estimates are reasonable. As a result, the filter estimates for the direct signal parameters result in error values that are again significantly larger than the RMS error values observed for the runs with the correct number of identified signals.

3.6.5 Direct Signal Parameter Accuracy Improvement with the Estimation of Multipath Signals

This subsection analyzes the results from the set of cases with one random multipath signal and from the set with two random multipath signals. It assesses the improvement in filter accuracy for the direct signal's parameters that results from the estimation of multipath features. Recall that two different estimates for the direct signal's parameters are obtained for each simulation, one from the usual procedure of this paper's algorithm and the other from where the algorithm limits itself to finding only the direct signal. In other words, when the algorithm stops at $M = 1$ signal regardless of the value of the test statistic obtained from the solution $\underline{x}_{opt,1}$.

For the 500 runs with one random multipath signal, the RMS errors for θ, ϕ, ω_D, and τ are, respectively, 0.28 degrees, 0.30 degrees, 0.74 Hz, and 0.002 chips when the algorithm proceeds normally. The maximum errors in the same parameters are, respectively, 1.02 degrees, 1.94 degrees, 2.25 Hz, and 0.006 chips. When the algorithm stops at $M = 1$, the RMS errors are, respectively, 10 degrees, 9 degrees, 5.1 Hz, and 0.05 chips. The maximum errors are, respectively, 51 degrees, 38 degrees, 28 Hz, and 0.27 chips. Both the RMS errors and the maximum errors show a significant reduction when the algorithm functions normally as opposed to stopping at $M = 1$. The estimation of the multipath signals attenuates multipath-induced inaccuracies of direct-path signal parameter estimates.

In terms of the polarization, the difference between the estimated RHCP power and the estimated LHCP power falls in the range from 26 dB to 80 dB for the direct signal when the filter functions normally. This large power difference between the RHCP and LHCP phasors show that the filter successfully captures the RHCP nature of the signal

for all the runs. When the filter is limited to finding only the direct signal, this power ratio lies in the range from 3 dB to 47 dB. In the best case scenario, this limited filter captures the RHCP nature of the direct signal, but in the worst case scenario, the filter fails in this task, and instead estimates that the signal is nearly linearly polarized.

For the 500 runs with two random multipath signal, the RMS errors for θ, ϕ, ω_D, and τ are, respectively, 0.36 degrees, 0.37 degrees, 0.84 Hz, and 0.002 chips when the algorithm proceeds normally. The maximum errors in the same parameters are, respectively, 1.02 degrees, 1.94 degrees, 2.25 Hz, and 0.006 chips. When the algorithm stops at $M = 1$, the RMS errors are, respectively, 14 degrees, 32 degrees, 8.3 Hz, and 0.10 chips. The maximumerrors are, respectively, 60 degrees, 180 degrees, 46 Hz, and 0.53 chips. Similar to the 500 runs with one multipath signal, both the RMS errors and the maximum errors show a significant reduction when the algorithm functions normally as opposed to enforcing the limit for $M = 1$. The errors when the algorithm is limited to $M = 1$ are higher for these runs than the runs with only one multipath signal. This is expected because the additional multipath signal causes further distortion of the direct signal's estimated parameters when multipath signals are unaccounted for by the estimator.

The polarization estimates show a similar trend to the cases with a single multipath component. When the filter functions normally, the estimated power difference between the RHCP and LHCP phasors range from 25 dB to 68 dB. When the filter is limited to $M = 1$, this power difference ranges from -8 dB to 43 dB. Clearly, the ability to estimate the multipath signals enables the filter to successfully capture the RHCP nature of the direct signal.

3.6.6 Results from a Filter Mismatch for the Cases with Two Signals

Often, the estimator does not have a perfect replica of the distorted PRN cross-correlation function for its RF front-end. In order to analyze the effects of such a model mismatch, all cases with two signals are re-run with the filter given an RF front-end bandwidth that's different from the one used in generating the measurements in the truth-model simulation. Bandwidth values of 1.7, 1.8, 1.9, 2.1, 2.2, 2.3, 2.4, and 2.5 MHz are used in the filter model. Unlike all other cases in this paper, none of these filter model bandwidths equal the truth-model simulation bandwidth of 2.0 MHz. For each wrong bandwidth, 500 runs for all 7 DOA cases are re-analyzed. Figure 3.13 shows the false alarm rates for all 7 cases, with the 8 different RF front-end bandwidth values used in the filter model. This figure shows the frequency with which the filter incorrectly identifies the presence of extra signals. The false alarm rates for all the mismatched filter bandwidth cases are equal to or larger than the false alarm rates observed from an estimator with perfect bandwidth match, as expected. The false alarm rate increases as the RF front-end bandwidth value used by the estimator moves away from the true value, obtaining maximum rates in both bandwidth error directions, with the greatest changes as shown by the dashed magenta line marked with stars for a bandwidth of 1.7 MHz and the dashed green line marked with x symbols for a bandwidth of 2.5 MHz. For small mismatches, as shown by the dashed black line marked with squares for 2.1 MHz and the magenta line marked with crosses for 1.9 MHz, the estimator is able to work as expected and the false alarm rates remain below 0.5%. This shows that the estimator is robust to small mismatches between the true distorted cross-correlation function and the one used by the filter.

Table 3.3 shows the RMS errors and the computed filter 1-σ estimates in the direct signal's parameters for the different filter bandwidth values and for the runs that identi-

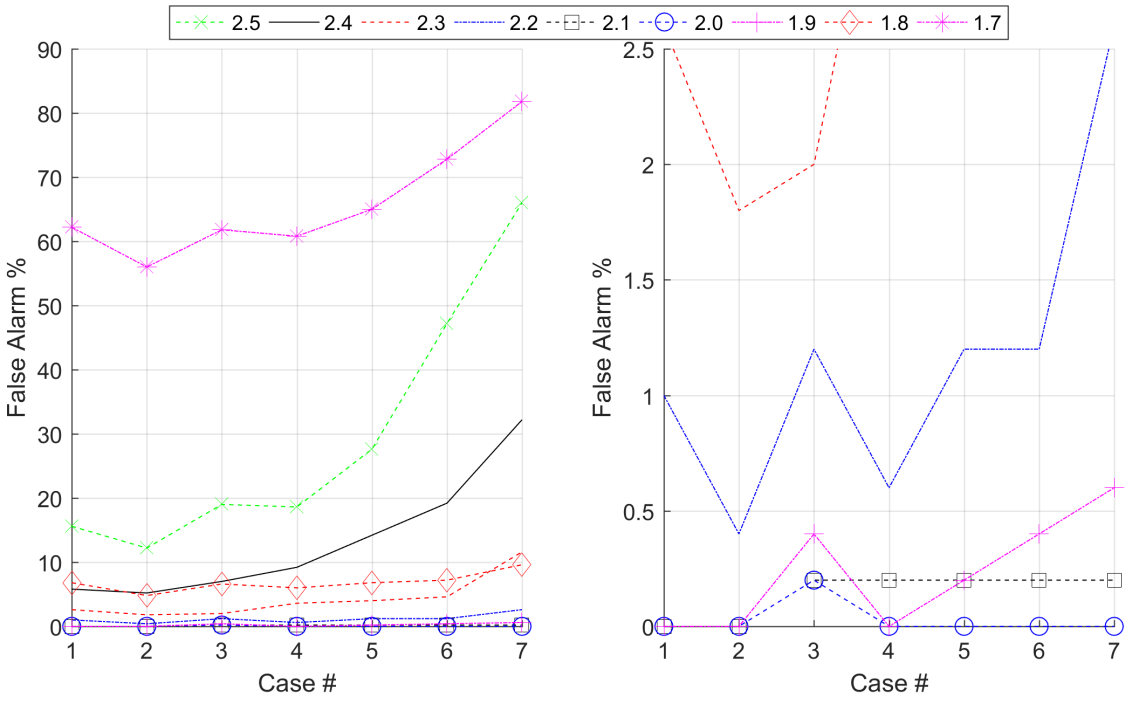

Figure 3.13: *False Alarm rates with RF front-end bandwidth mismatch (zoomed version on the right)*

fied the correct number of signals. Each entry of the table shows two values for a particular combination of estimated quantity (column) and bandwidth (row). The first value in an entry represents the RMS error, and the second value is the computed filter 1-σ estimate. The row that corresponds to values from perfect bandwidth match is italicized for emphasis. The bandwidth mismatch does not seem to have any significant impact on the accuracy of the co-elevation angle and the carrier Doppler shift (see second and fourth columns). The RMS errors and 1-σ filter estimates remain the same with different levels of mismatch. In addition, the observed RMS errors match the filter predicted values. The predicted filter accuracy level for the azimuth angle also shows no variation with the amount of bandwidth mismatch. However, the observed RMS errors increase with larger mismatch values (see the third column). RMS errors in PRN code phase show the most impact of bandwidth mismatch. RMS errors increase from 0.004 chips in the perfect-bandwidth-match case to 0.028 chips in the most-mismatched-bandwidth case.

Bandwidth (MHz)	θ (deg)	ϕ (deg)	ω_D (Hz)	τ (chips)
1.7	0.4 | 0.4	1.0 | 0.4	1.0 | 1.0	0.025 | 0.004
1.8	0.3 | 0.3	0.6 | 0.4	1.0 | 1.0	0.011 | 0.004
1.9	0.3 | 0.3	0.4 | 0.4	1.0 | 1.0	0.007 | 0.004
2.0	*0.3 | 0.3*	*0.4 | 0.4*	*1.0 | 1.0*	*0.004 | 0.004*
2.1	0.3 | 0.3	0.5 | 0.4	1.0 | 1.0	0.010 | 0.004
2.2	0.3 | 0.3	0.6 | 0.4	1.0 | 1.0	0.018 | 0.004
2.3	0.3 | 0.3	0.8 | 0.4	1.0 | 1.0	0.022 | 0.004
2.4	0.3 | 0.3	0.8 | 0.4	1.0 | 1.0	0.025 | 0.004
2.5	0.4 | 0.4	1.0 | 0.4	1.0 | 1.0	0.028 | 0.004

Table 3.3: RMS errors and computed filter 1-σ values of the direct signal parameters with RF front-end bandwidth mismatch for the cases with two signals

This significant increase in error is expected since a mismatch in the cross-correlation function form directly affects the estimator's ability to lock on to the code phase peak for each signal. More worrisome is the absent increase in the 1-σ filter estimates for τ. The filter reports the same accuracy level in its τ estimates regardless of bandwidth, resulting in overconfident filter estimates compared to the actual RMS errors. Nevertheless, even with the most mismatch, RMS PRN code phase error is significantly below the actual code phase difference of the two simulated signals, i.e. below 0.2 chips. This enables to the filter to label the direct signal correctly even in the most mismatched cases, on the condition that the filter identifies the correct number of signals.

3.6.7 Results from the DOA Grid Spacing Analysis

Additional simulations have been run in order to investigate the effects of co-elevation and azimuth spacing in the initial DOA search grid. Five hundred runs of the simulation have been generated using 2 signals with the signal parameters from Table 3.1. The azimuth angle for the multipath signal is selected such that the DOA's of the two signals differ by 20 degrees. Another 500 runs of the simulation have been generated for a

3-signals case with the signal parameters from Table 3.2. The relative power of the second multipath signal is set to -5 dB. For different co-elevation and azimuth search grid spacings, the estimator is given the same set of 500 runs such that the measurement noise values are the same for each chosen grid spacing.

Table 3.4 shows the results from the simulations that investigate the DOA search grid spacing. Each column describes the results from a different grid. The second column, with co-elevation and azimuth spacings of 18 deg., is the grid used in all the previous simulations, and its performance is used as a baseline against which comparisons are made. The first and the second rows give, respectively, the spacing in co-elevation and the spacing in azimuth. The third and fourth rows show the average reduction in processing time for the estimator compared to the baseline grid with, respectively, 2 and 3 simulated signals. The last two rows indicate the false alarm (extra-signal) rates for the runs with 2 and 3 simulated signals, respectively.

The false extra-signal rates show no change with the different grids. For each run, the estimator is able to come to the same optimal solution, within the estimator tolerance, for all the grids. As a result, the test statistic values generated for all runs are almost the same irrespective of the initial DOA grid spacing. The estimator is able to reach the global minimum of the cost function for all runs, independent of the initial DOA grid spacing. In terms of the processing time, all the larger grid spacings show a reduction compared to the baseline grid. However, the biggest reduction in time is not observed in

θ-spacing (deg)	18	30	45	45
ϕ-spacing (deg)	18	30	45	60
Time reduction, M=2	-	24%	31%	19%
Time reduction, M=3	-	8%	10%	4%
False Extra-Signal Rate, M=2	0.2%	0.2%	0.2%	0.2%
False Extra-Signal Rate, M=3	0.4%	0.4%	0.4%	0.4%

Table 3.4: Results for different co-elevation/azimuth grids in the initial DOA search

the estimator that uses the smallest grid — results are shown in the last column of Table 3.4. Rather the grid whose results are shown in the second-to-last column reduces the execution time the most.

This result can be explained by considering the trade-offs when increasing the grid spacing. While a larger spacing enables a faster initial DOA search, thereby reducing processing time, it also results in an initial guess for the GN optimization that is farther from the optimal solution than an initial guess resulting from a grid with smaller spacing. As a result of the increased distance between the initial guess and the global minimum of the cost function, the estimator has to go through more GN iterations in order to arrive at the optimal solution. Compared to the baseline case, the decrease in processing time to search through the DOA grid exceeds the increase in time from increased number of GN iterations. This hold true for all of the alternate grids considered. The 45 deg-by-45 deg grid appears to optimize this trade-off between the initial DOA grid search and the GN optimization.

Another thing to note is that the processing time reduction as a percentage of the total processing time is smaller for all the alternate grids when solving for 3 signals instead of 2 signals. This is explained by the additional GN iterations the estimator goes through in 3 signal cases due to the need to consider all the local minima in the initial DOA search to seed the GN optimization. More of the processing time is taken by GN iterations for 3 signals compared to 2 signals; so, the time trade-off between the DOA grid search and the GN optimization leans more toward the GN optimization. Thus, a reduction in the DOA grid shows less percentage improvement in the estimator processing time when there are 3 signals.

3.7 Summary and Conclusions

This paper has developed and presented a method to estimate multipath in GNSS signals with the use of a special antenna array. The array must have RHCP and LHCP feeds for each antenna element. Each feed of each element must have a good calibration of its steering vector in response to both RHCP and LHCP incident signals. It is possible to build such arrays using a half dozen patch antennas with a total array footprint that has a diameter of 12 cm.

A maximum likelihood batch estimator has been developed to filter data from such an antenna array. A truth-model simulation has been used to assess the likely performance of the proposed estimator. The batch filter estimates the direction of arrival, code phase, carrier phase, carrier Doppler shift, and RHCP and LHCP phasors for each signal. It includes techniques to ensure convergence to the global minimum of its nonlinear least-squares cost function. It iteratively estimates the number of multipath signals by looking at cost residuals to determine whether its current assumed number needs to be incremented.

The simulation results indicate that the filter successfully estimates each signal's parameters for cases that include a direct signal and up to two multipath signals. The only failures occur in a very small percentage of cases when the estimator incorrectly overestimates the number of signals. It never underestimates this number. Further tuning of the filter's extra-signal detection bound might reduce the wrong-number cases.

For two signals, successful estimation is observed even when the two signals come from the same direction. Code phase and polarization difference enable the filter to distinguish two signals in such cases. Analysis of RF front-end bandwidth mismatch reveals that the estimator is robust to small mismatches. The degraded performance

with increasing bandwidth mismatch emphasizes the need of the proposed method to have a good characterization of the RF front-end filter response.

For all cases where the filter determines the correct number of signals present, actual RMS errors match well with the filter's predicted 1-σ estimates. Typical direct signal DOA accuracies are on the order of 0.4 deg RMS or less. Code phase accuracies are on the order of 0.004 chips. In the cases where the filter fails to identify the correct number of signals, it produces inaccurate estimates of the direct signal's parameters. With proper tuning of the detection threshold for the extra signals, or with sequential filtering of a sequence of such detections, misidentification of the number of signals and the resulting parameter estimation errors should become rare.

CHAPTER 4

PASSIVE-REFLECTOR-BASED RADIONAVIGATION SYSTEM

4.1 Abstract

A novel radionavigation system based on passive spherical reflector satellites and ground transmitters is developed. Such a system would constitute an adaptable global navigation system with an increased robustness against attacks due to the ability to change the broadcast signal characteristic at a much quicker pace than the currently available global navigation satellite systems in the case of system compromise. A rectangular transmitter array is designed for the proposed system. Expected power density levels at ground receivers and phase deviations from spherical propagation are investigated for a range of proposed orbital altitudes. The effects of different array sizes are considered. Results show that a reflector altitude of 10000 km provides good power density levels for a radiated power of 50 kW. This altitude also provides acceptable phase deviations from spherical propagation.

4.2 Introduction

Position, Navigation, and Timing (PNT) services are vital to many essential applications worldwide. In particular, global navigation satellite systems such as the Global Positioning System (GPS) have attained widespread civilian and military use. This widespread use of GPS necessitates robustness to provide integrity to the PNT services. GPS vulnerability in the form of spoofing has been recognized as one threat [30, 31], and the need for a robust system has become more evident with the recent field demonstrations

of the unencrypted civilian L1 C/A signal spoofing [4, 32, 33]. Jamming also poses a threat to GPS. Service denial in the form of jamming has also been studied as a major GPS vulnerability [34–36].

Various methods have been proposed to detect spoofing attack. The proposed methods include the use of multiple antennas [37], reliance on cross-correlation of encrypted signals between a secure receiver and the receiver under attack [38, 39], dependence on inertial measurements [40], and changes to the navigation message to provide authentication bits [41]. However, in the event that the security of the military signals of GPS is compromised, the methods that rely on cross-correlation, authentication bits, or the encrypted military code would fail to work as intended. A compromised GPS system would require the design of a new, secure signal to be broadcast. Unfortunately, the current GPS constellation lacks the ability to change the signal broadcast from the GPS satellites in orbit. Thus, a replacement of the whole GPS constellation, which would be very expense and slow, would be required.

This vulnerability can be avoided by developing a system whose broadcast signal can be changed relatively easily when needed. One way to provide signal adaptability is to rely on ground transmitters to broadcast the signals instead of active satellites. The proposed system relies on passive orbiting reflectors that would reflect the ground-transmitted signals back to Earth. Because the transmitters are on the ground, the signal can be rapidly and cheaply changed when needed, especially if the signal loses its integrity.

Project Echo was a passive communication satellite program conducted by NASA during the 1960s [42, 43]. It relied on balloon satellites that served as passive reflectors for communication signals that were broadcast from a ground antenna. Two experimental satellites were flown, Echo 1 and Echo 2. Their respective diameters were 30.5 and

41 meters. Figure 4.1 shows Echo 2 on the ground. The system included a 26 meter HA-DEC antenna to track the satellites and a 26.5 meter Az-El dish antenna that transmitted the communication signal. The signal frequency was 2390 MHz. The system was tested successfully when a pre-recorded message was relayed to a secondary location on Earth by reflecting the signal off of the balloon. The radar tracking of the satellites was shown to be accurate to 0.1 degree for the transmitting antenna. The project was abandoned later as it was believed that the reliability of the proposed method needed to be improved before it could be considered operationally feasible. Soon after, active communications satellite systems became the focus of satellite communications developments, and the use of active satellites was a natural choice when satellite-based radionavigation systems were developed.

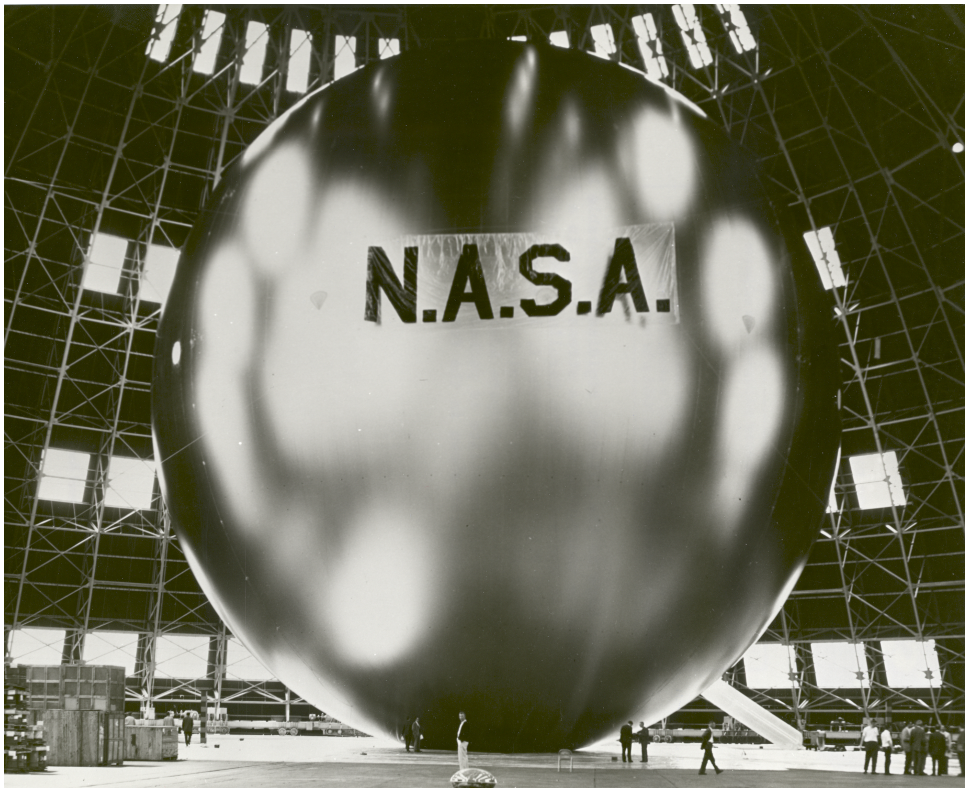

Figure 4.1: *A photograph of Echo 2 undergoing tensile stress test*

The proposed method seeks to revisit the use of the passive reflectors demonstrated

in Project Echo. A constellation of passive reflector satellites, with sufficient numbers and distribution around the globe to provide global coverage of reflected signals, is the central part of the proposed system. On the ground side, the system includes antenna arrays that are distributed around the globe to ensure that each reflector satellite is visible continuously from at least 1 transmitter. Figure 4.2 shows a diagram of the proposed system. The ground transmitters are depicted by the black antenna arrays, and the user receiver is shown by the blue antenna. Three reflectors in orbit are depicted by grey circles. Blue, orange, and green solid arrows show the transmitted signals from the ground transmitter on the left. Yellow and black solid arrows show the transmitted signals from the ground transmitter on the right. Blue, orange, green, yellow, and black dashed arrows depict the reflected signals that are received by the user receiver. The system requires the transmitter to be able to send signals to all visible reflectors in view. This requirement necessitates the use of dynamic phased arrays at the ground transmitters. Steering of the transmitted signals from the arrays to the reflectors is accomplished through the use of dynamic phasing. The use of electronic steering instead of mechanical steering, as implemented by Project Echo, is intended to enable rapid steering of the signal beam and the ability to transmit to multiple reflectors in view of a single ground transmitter. In general, as observed in GPS, the user requires signals from at least 4 distinct reflectors to be able to solve for its position and timing.

This paper makes 2 significant contributions to the subject of alternative PNT systems based on passive reflector satellites and ground-based transmitters. First, it analyzes a passive reflector-based radionavigation system that relies on ground-based phased-array transmitters. Second, it investigates the feasibility of the proposed system by analyzing expected signal performance. Power density level of the reflected signals on the ground and deviation of the received phase from a spherical propagation model are analyzed.

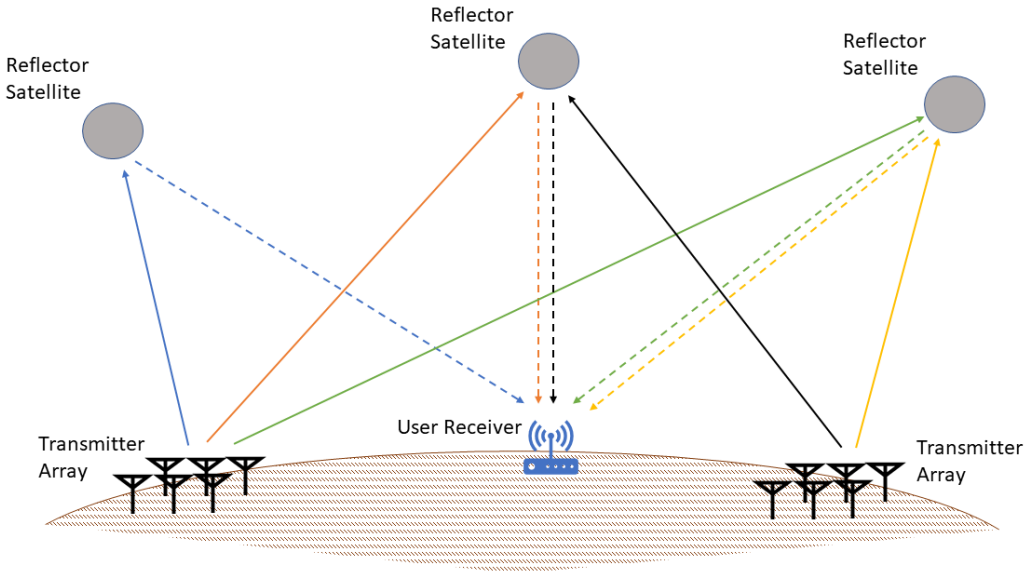

Figure 4.2: *Reflector-based system under consideration*

The remainder of the paper is organized as follows. The second section provides a detailed description of the antenna array model and the reflection calculations. The third section presents the results from simulations. A summary and conclusions are presented in the fourth section.

4.3 System Model

This section develops the antenna array model and the reflection model that are used in the power density and phase calculations.

4.3.1 Antenna Array Model

A rectangular array of identical elements is considered. Each element is excited with the same amplitude, but with different phase to achieve high gains in the direction of the reflector satellite.

Figure 4.3 shows the antenna array and the coordinate system used to derive the gain of the array. The coordinate system is centered on the central element. The coordinate system is local East, North, Up (ENU). The quantities θ, ϕ, and r are the equivalent spherical coordinates, co-elevation, azimuth and distance, respectively.

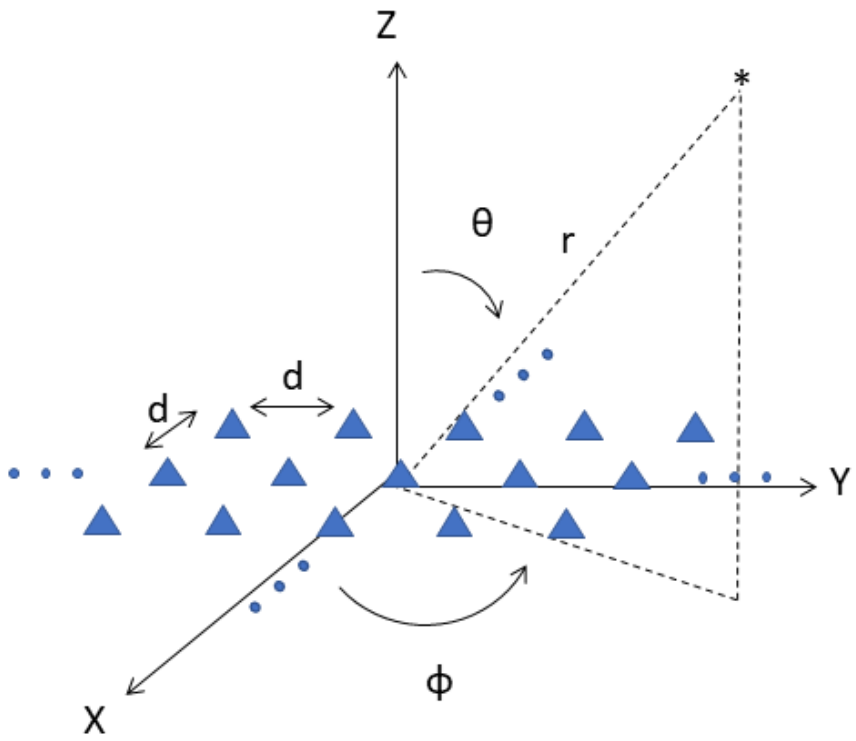

Figure 4.3: *Antenna array configuration and the local coordinate system*

Rows and columns of elements are parallel to the local east and the local north axes, respectively. The following equation describes the coordinate of the element in the m^{th} row and the n^{th} column. The array elements are separated by a distance d in both directions. There are $(2N+1)$ elements in each direction, and a total of $(2N+1)^2$ elements in the array. The side length of the array is $(2Nd)$.

$$\underline{r}_{mn} = md\hat{x} + nd\hat{y} \tag{4.1}$$

The following equation describes the phase of the element in the m^{th} row and the n^{th} column. It constitutes the phase steering law for the array. This phase is added to the nominal signal at each array element. The quantities α and β are, respectively, the phase progressions per unit length in the local east and local north directions. Varying these two quantities changes the location of the main beam in the array pattern and thus will be used to steer the main beam in the direction of the reflector.

$$\psi_{mn} = m\alpha d + n\beta d \tag{4.2}$$

The non-normalized array far-field pattern can be calculated using the following sum of each individual element's phasor over the whole array [44]:

$$\begin{aligned} F(\theta,\phi) &= \sum_{m=-N}^{N}\sum_{n=-N}^{N} e^{j\psi_{mn}+jk\ \hat{r}\cdot\underline{r}_{mn}} \\ &= \frac{\sin\left[\frac{2N+1}{2}(u+u_0)\right]}{\sin\left[\frac{1}{2}(u+u_0)\right]}\frac{\sin\left[\frac{2N+1}{2}(v+v_0)\right]}{\sin\left[\frac{1}{2}(v+v_0)\right]} \end{aligned} \tag{4.3}$$

The quantity $\hat{r}$ is the unit vector in the propagation direction defined by θ and ϕ, $\begin{bmatrix} \cos\phi\sin\theta & \sin\phi\sin\theta & \cos\theta \end{bmatrix}^T$. The quantity k is the wavenumber of the signal. The quantities u and v describe the dependence of the array factor (F) on the radiation direction:

$$u = kd\sin\theta\cos\phi \tag{4.4}$$

$$v = kd\sin\theta\sin\phi \tag{4.5}$$

The related quantities u_0 and v_0 are respectively, the phase progressions per element in the local east and local north directions. They are defined as $u_0 = \alpha d$ and $v_0 = \beta d$.

If the main beam of the radiation pattern from the antenna array is intended to be steered to the co-elevation/azimuth pair ($\hat{\theta}$,$\hat{\phi}$), the phase progression in each direction is calculated to achieve $u + u_0 = 0$ and $v + v_0 = 0$ in that direction. This leads to:

$$\alpha = -k\sin\hat{\theta}\cos\hat{\phi} \tag{4.6}$$

$$\beta = -k\sin\hat{\theta}\sin\hat{\phi} \tag{4.7}$$

One can calculate the total gain in any direction using the far-field un-normalized pattern from Eq. (4.3) and the radiation pattern of each element, $f(\theta,\phi)$. The function $f(\theta,\phi)$ represents the gain pattern of each individual element. The elements are assumed to be ideal hemispherical radiators for this study, and the exact radiation pattern used will be discussed in a later subsection. The resulting normalized gain takes the form [45]:

$$G(\theta,\phi) = 4\pi \frac{F^2(\theta,\phi) f^2(\theta,\phi)}{\int_0^{2\pi}\int_0^{\pi} F^2(\bar{\theta},\bar{\phi}) f^2(\bar{\theta},\bar{\phi}) \sin\bar{\theta} d\bar{\theta} d\bar{\phi}} \tag{4.8}$$

4.3.2 Specular Reflection Solution

The calculations required to find the specular reflection point on a spherical reflector in orbit for a given pair of antenna array location and receiver location are explored in this subsection. The specular reflection point on a spherical reflector is needed in order to calculate the received phase at the receiver location in the following subsections.

Figure 4.4 describes the problem of finding the specular reflection point. The quantity $\underline{r}_T$ represents the position of the antenna array in some arbitrary coordinate system. The vectors $\underline{r}_R$ and $\underline{r}_{ref}$ are, respectively, the position of the receiver and the specular reflection point on the satellite in the same coordinate system. The solid blue arrow shows the transmitted signal. The dashed blue arrow is the same signal reflected at the specular reflection point and received by the user. Given a radius of R and a center location vector of $\underline{r}_0$ for the spherical reflector, the specular reflection point must satisfy the following set of equations:

$$\left|\left|\underline{r}_{ref} - \underline{r}_0\right|\right| = R \tag{4.9}$$

$$\underline{u}_r - \underline{u}_t + 2(\underline{u}_t^T \underline{n})\underline{n} = 0 \tag{4.10}$$

where

$$\underline{u}_r = \frac{\underline{r}_R - \underline{r}_{ref}}{\left|\left|\underline{r}_R - \underline{r}_{ref}\right|\right|} \tag{4.11}$$

$$\underline{u}_t = \frac{\underline{r}_{ref} - \underline{r}_T}{\left|\left|\underline{r}_{ref} - \underline{r}_T\right|\right|} \tag{4.12}$$

$$\underline{n} = \frac{\underline{r}_{ref} - \underline{r}_0}{\left|\left|\underline{r}_{ref} - \underline{r}_0\right|\right|} \tag{4.13}$$

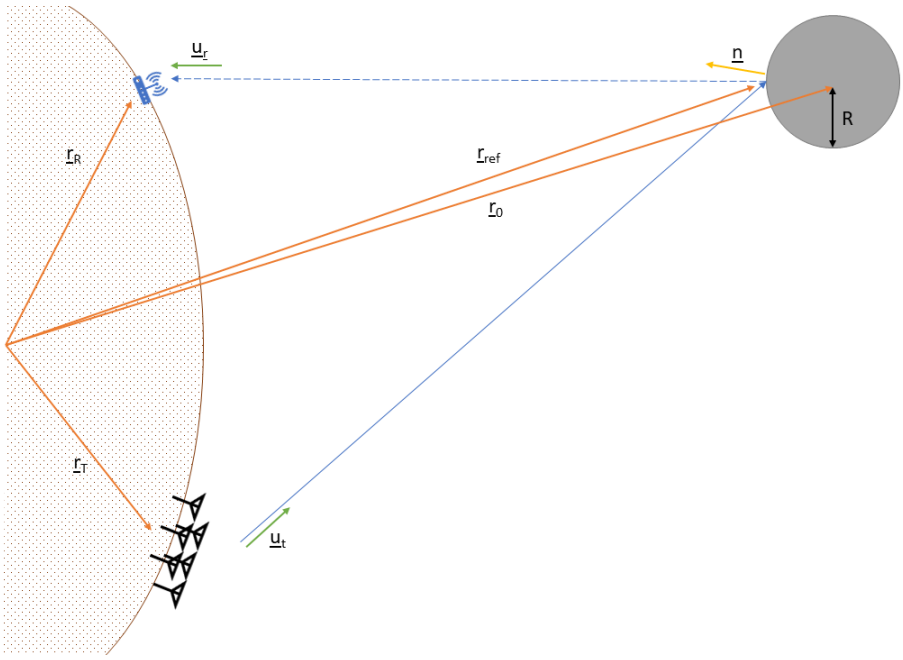

Figure 4.4: *Specular reflection problem*

The quantities $\underline{u}_t$, $\underline{u}_r$, and $\underline{n}$ are, respectively, the unit vector from the transmitter to the reflection point, the unit vector from the reflection point to the receiver, and the unit normal vector to the spherical surface at the reflection point, as depicted in Fig. 4.4. The only unknowns in the problem are the coordinates of the reflection point given by $\underline{r}_{ref}$. Eqs. (4.9) and (4.10) are implicit equations in $\underline{r}_{ref}$.

Given the geometry of the problem, the number of unknowns can be reduced down to 1 from 3 by considering the plane created by $\underline{r}_R$, $\underline{r}_T$, and $\underline{r}_0$. This reduces the problem to finding a reflection point on a circle.

Figure 4.5 describes the modified problem of finding the specular reflection point on a circle. The coordinate system is centered at the physical center of the reflector. The receiver is placed on the x-axis of the plane, labeled X_{Plane}, and the y-axis, labeled Y_{Plane}, is defined such that the transmitter lies in the +y half of the xy-plane. A single quantity, θ_{ref} is used to describe the reflection point. Its coordinates in the new coordinate system are defined by the vector $\underline{r}_{ref} = \begin{bmatrix} R\cos\theta_{ref} & R\sin\theta_{ref} \end{bmatrix}^T$. The vectors $\underline{u}_r$, $\underline{u}_t$, and $\underline{n}$ are similarly redefined using the new planar coordinate system:

$$\underline{u}_r = \frac{\begin{bmatrix} (\rho_R - R\cos\theta_{ref}) & -R\sin\theta_{ref} \end{bmatrix}^T}{\left\| \begin{bmatrix} (\rho_R - R\cos\theta_{ref}) & -R\sin\theta_{ref} \end{bmatrix}^T \right\|} \tag{4.14}$$

$$\underline{u}_T = \frac{\begin{bmatrix} (R\cos\theta_{ref} - X_T) & (R\sin\theta_{ref} - Y_T) \end{bmatrix}^T}{\left\| \begin{bmatrix} (R\cos\theta_{ref} - X_T) & (R\sin\theta_{ref} - Y_T) \end{bmatrix}^T \right\|} \tag{4.15}$$

$$\underline{n} = \begin{bmatrix} \cos\theta_{ref} & \sin\theta_{ref} \end{bmatrix}^T \tag{4.16}$$

The quantities ρ_R, X_T, and Y_T are, respectively, the distance from the reflector sphere origin to the receiver, the new 2-dimensional X-coordinate of the transmitter, and the new 2-dimensional Y-coordinate of the transmitter.

This results in a single 2D-vector equation, a modified form of Eq. (4.10), with a single unknown, θ_{ref}, to be solved for finding the point of reflection. However, a closed-form solution for this problem does not exist [46]. Thus, the specular reflection point is calculated using Newton's method to solve this problem involving a modified form of Eqs. (4.10-4.13):

$$0 = A \sin\theta_{ref} \cos\theta_{ref} + B(\sin^2\theta_{ref} - \cos^2\theta_{ref}) + C\cos\theta_{ref} + D\sin\theta_{ref} \tag{4.17}$$

where

$$A = 2\, X_T\, \rho_R \tag{4.18}$$

$$B = Y_T\, \rho_R \tag{4.19}$$

$$C = R\, Y_T \tag{4.20}$$

$$D = -R\,(X_T + \rho_R) \tag{4.21}$$

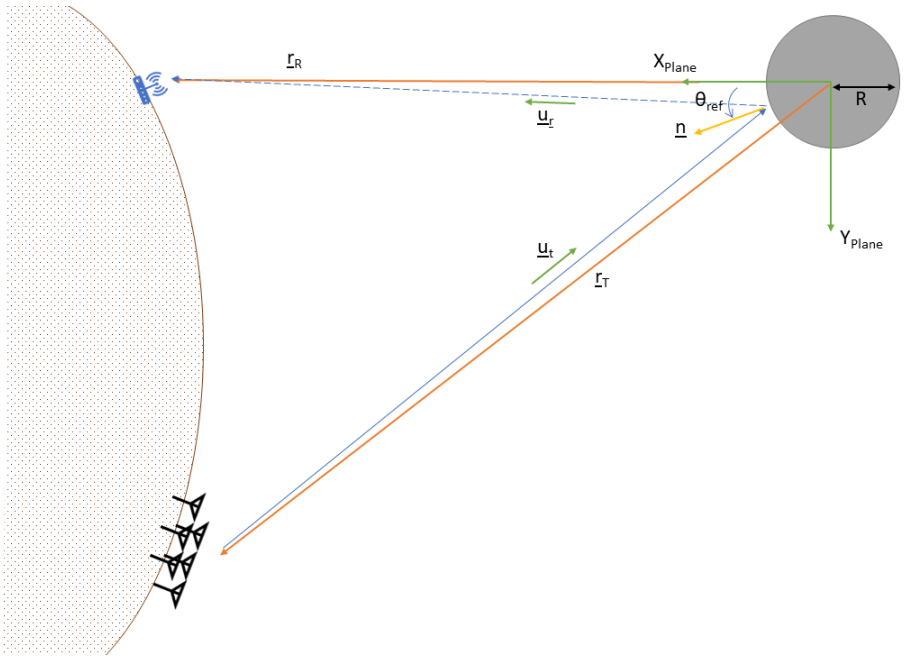

Figure 4.5: *Specular reflection problem - planar*

4.3.3 Power Density Calculation

The system under study involves transmission from ground and reflection in orbit. This means that signal power loss through propagation is expected to be greater than active satellite systems that have one-way propagation (orbit to ground) as opposed to two (ground to orbit followed by orbit to ground). Because of this, received power on ground needs to be investigated to analyze the feasibility of the system.

The received power density at a given receiver location, $\underline{r}_R$ is calculated using the following equation [47]:

$$\bar{P}_R = \frac{G(\theta_{ref},\phi_{ref})\, P_T}{4\pi \left|\left|\underline{r}_T - \underline{r}_{ref}\right|\right|^2} \frac{\sigma_{ref}(\underline{r}_T,\underline{r}_R)}{4\pi \left|\left|\underline{r}_R - \underline{r}_{ref}\right|\right|^2} \tag{4.22}$$

The first fraction represents the signal power density at the reflector location. The quantity P_T is the total power radiated by the antenna array. It includes the antenna gain in the direction of the reflector (θ_{ref},ϕ_{ref}) to get the effective radiated power in that direction. The denominator, $4\pi \left|\left|\underline{r}_T - \underline{r}_{ref}\right|\right|^2$, represents the power loss due to the distance between the antenna array and the reflector. Similarly, the second denominator $4\pi \left|\left|\underline{r}_R - \underline{r}_{ref}\right|\right|^2$ is the power loss due to the distance between the reflector and the receiver.

The quantity $\sigma_{ref}(\underline{r}_T,\underline{r}_R)$ in Eq. (4.22) is the scattering cross section of the reflector. It depends on the reflection scenario and this dependence is expressed as a function of the transmitter and receiver locations. However, for this study, certain assumptions are made that simplify the expression for the scattering cross section. First, the reflector is assumed to be a perfect electric conductor (PEC) sphere. Second, the reflector sphere is assumed to be large compared to the wavelength of the signal. The behaviour of the

scattering cross section depends on the product of the wavenumber and the reflector radius (kR). The particular radius of the reflector sphere and the particular wavelength used for this study will be discussed in a later section, but using the values from Project ECHO gives a value of about 1000 for this product. In this large sphere regime ($kR >> 1$), the scattering cross section simplifies to the following expression [48]:

$$\sigma_{ref}(\underline{r}_T, \underline{r}_R) = \pi R^2 \tag{4.23}$$

This result can be derived by considering how the area perpendicular to the direction of travel at the receiver, A, depends on the solid angle at the transmitter, Ω. One can calculate $\frac{dA}{d\Omega}$ and calculate the scattering cross section through this derivate, $\sigma_{ref} = \left(4\pi \left|\left|\underline{r}_R - \underline{r}_{ref}\right|\right|^2 \times \left|\left|\underline{r}_T - \underline{r}_{ref}\right|\right|^2\right) / \frac{dA}{d\Omega}$. Such calculations agree with the simplified result from Eq. (4.23).

This implies that the reflector scatters back the incident power isotropically and the scattering cross section is a constant independent of the transmitter and receiver location. This approximation is invalid in the forward scattering scenarios where the transmitter and the receiver lie on the opposite sides of the reflector; however, scenarios where both the transmitter and the receiver are on Earth, located on the same side of the reflector, are considered for this study.

For simplicity, potential power losses due to propagation through the ionosphere and the neutral atmosphere are ignored in this discussion. The effects of the ionosphere and the neutral atmosphere on the received power density are left for a future study.

4.3.4 Phase Calculation

The total phase of the signal at the receiver location is given by the following equation:

$$\theta_R(\underline{r}_R) = -k\left|\underline{r}_T - \underline{r}_{ref}\right| - k\left|\underline{r}_R - \underline{r}_{ref}\right| - \pi \tag{4.24}$$

The first two terms are the phase changes due to the wave propagation. The extra phase of π radians is due to the reflection from the sphere.

These phase calculations for a reflector sphere in the far-field regime are typical in the literature [49], but the possibility of approximating the non-spherical wave front by finding the best-fit phase center assuming a spherical wave-front model for use in navigation solutions has not been explored. One important question to be answered is the variation of the received phase on the ground from an expected phase given a spherical propagation from the reflector. Pseudorange equations typically used in receiver location solutions employed by radionavigation systems such as GPS make the assumption that the signal phase varies as though the signal is propagated spherically from the transmitter. Any large variations from this assumption in the received phase would incur large errors in the calculated receiver location when pseudoranges from the transmitters are employed for receiver location calculations for the system under study (unless a more complicated pseudorange model were used). Thus, variation from spherical propagation in received phases and the best-fit phase center are studied.

Given K receiver locations on Earth, the observed phases can be calculated using Eq. (4.24) to form a vector of received phases as follows:

$$\underline{z} = \begin{bmatrix} \theta_R(\underline{r}_{R1}) \\ \theta_R(\underline{r}_{R2}) \\ \vdots \\ \theta_R(\underline{r}_{R(K-1)}) \\ \theta_R(\underline{r}_{RK}) \end{bmatrix} \tag{4.25}$$

The expected phase for the k^{th} receiver location, $\underline{r}_{Rk}$, assuming a spherical propagation from a phase center of $\underline{r}_C$ with a nominal phase of θ_0 at the phase center, is given by the following equation:

$$h_k(\underline{r}_C, \theta_0) = \theta_0 - k|\underline{r}_C - \underline{r}_{Rk}| \tag{4.26}$$

The nonlinear least-squares problem is to find the phase center and nominal phase that minimize the following cost function:

$$J(\underline{r}_C, \theta_0) = \frac{1}{2}[\underline{z} - \underline{h}(\underline{r}_C, \theta_0)]^T[\underline{z} - \underline{h}(\underline{r}_C, \theta_0)] \tag{4.27}$$

where

$$\underline{h}(\underline{r}_C, \theta_0) = \begin{bmatrix} h_1(\underline{r}_C, \theta_0) \\ h_2(\underline{r}_C, \theta_0) \\ \vdots \\ h_{K-1}(\underline{r}_C, \theta_0) \\ h_K(\underline{r}_C, \theta_0) \end{bmatrix} \tag{4.28}$$

Finding an optimal solution to this problem is straightforward using Gauss-Newton (GN) solution techniques. A good initial guess for the phase center is $\underline{r}_0$, the physical center of the reflector sphere.

Once an optimal solution to the two variables, $\hat{\underline{r}}_c$ and $\hat{\theta}_0$, are found, the deviation from a spherical propagation at each receiver location is obtained through the residual:

$$\delta\theta_{Rk} = \theta_R(\underline{r}_k) - h_k(\hat{\underline{r}}_c, \hat{\theta}_0) \tag{4.29}$$

For simplicity, delays due to propagation through the ionosphere and the neutral atmosphere are ignored in this discussion. The effects of the ionosphere and the neutral atmosphere on the phase are left for a future study.

4.4 Simulation Results

This section discusses the results from various scenarios that are considered to analyze the feasibility of the system. The first subsection discusses the simulation setup with a detailed description of the scenarios. The second subsection explores the antenna array and the expected gain. The third subsection presents the expected power density on ground for a variety of reflector altitudes and transmitter-reflector geometries. The fourth subsection presents the results for deviation from spherical propagation of the signal phase at a range of receiver locations.

4.4.1 Simulation Setup

The frequency for the signal is set at 3.75 GHz, with a corresponding wavelength of 8 cm. Three reflector sizes, a radius of 10, 15, and 20 m, are considered. This range of sphere radii results in a range of kR of 785 to 1571. As a result, the scattering cross section given in Eq. (4.23) is valid for all the considered radii.

Three orbital altitudes are considered. The first altitude is at low Earth orbit (LEO), with a value of 2000 km. The second and third altitudes are at medium Earth orbit, with values of 10000 and 20200 km. The last altitude corresponds to the GPS altitude, with an orbital period of 12 hours. There is a trade-off between the received power density and the ground coverage as the reflector orbital altitude varies, and these three altitudes are chosen to study this variation.

For each considered altitude, the reflector is placed in orbit with latitude and longitude of 0 degrees. When the transmitter array is placed on the same latitude and longitude, the reflector is at zenith. The effects of location of the reflector relative to the transmitter are analyzed by moving the transmitter array to different locations on Earth. For each reflector altitude and for each transmitter location, a range of receiver locations are considered. Since the ground coverage depends on the altitude, the range of considered receiver latitude and longitude values depend on the altitude. For the first altitude, second altitude and third altitude, the receiver latitude and longitude have a range of, respectively, -23.8 to 23.8 degrees, -44.5 to 44.5 degrees, and -52.5 to 52.5 degrees. These values result in a maximum co-elevation of about 82 degrees for all altitudes at the corners of the receiver grid. The spacing in receiver latitude and longitude values is set to 5 degrees.

Antenna arrays with side lengths of 1 km, 2 km, or 4 km, are used for the calcula-

tions. The largest S band array is the Space Fence radar system currently under construction. It has a side length of about 25 meters [50]. Thus, the array sizes considered for this study might be unfeasible for the current technology.

The distance between each element is set to 0.9λ. This value is kept below 1λ to prevent the appearance of a grating lobe in the array pattern. The presence of grating lobes leads to a significantly decreased array gain, which defeats the purpose of having a large array [45]. The 0.9λ distance between elements gives 13887, 27777, and 55555 elements in each array direction, for each of the respective array side lengths. The total power radiated by the antenna array is set to 50 kW. Each element is considered to be an ideal hemispherical radiator with the following radiation pattern:

$$f(\theta,\phi) = \begin{cases} 1, & \text{if } \theta \leq \frac{\pi}{2} \\ 0, & \text{otherwise} \end{cases} \tag{4.30}$$

This results in the following simplification of Eq. (4.8) for the final gain equation:

$$G(\theta,\phi) = \begin{cases} 4\pi \frac{F^2(\theta,\phi)}{\int_0^{2\pi}\int_0^{\pi/2} F^2(\bar{\theta},\bar{\phi})\sin\bar{\theta}\, d\bar{\theta}\, d\bar{\phi}}, & \text{if } \theta \leq \frac{\pi}{2} \\ 0, & \text{otherwise} \end{cases} \tag{4.31}$$

The integral in the denominator is calculated numerically. In practice, no such radiator exists and the effect of the element radiation pattern on the transmitter gain should be considered in a further study.

4.4.2 Antenna Array Gain

For the given antenna array specifications in the previous subsection with a side length of 1 km, the antenna gain when the main beam is steered at the zenith is calculated as 93 dB. The arrays with a side length of 2 km and 4 km have an antenna gain 6 dB and 12 dB more in the zenith direction, respectively. Figure 4.6 shows the gain near the main beam of the array. The first null beam width is 1.6×10^{-4} radians. This small beam width requires the system to have very good ground tracking of reflector locations. A tracking error around 3×10^{-5} radians would lead to a loss of 2.1 dB in the power received by the reflector.

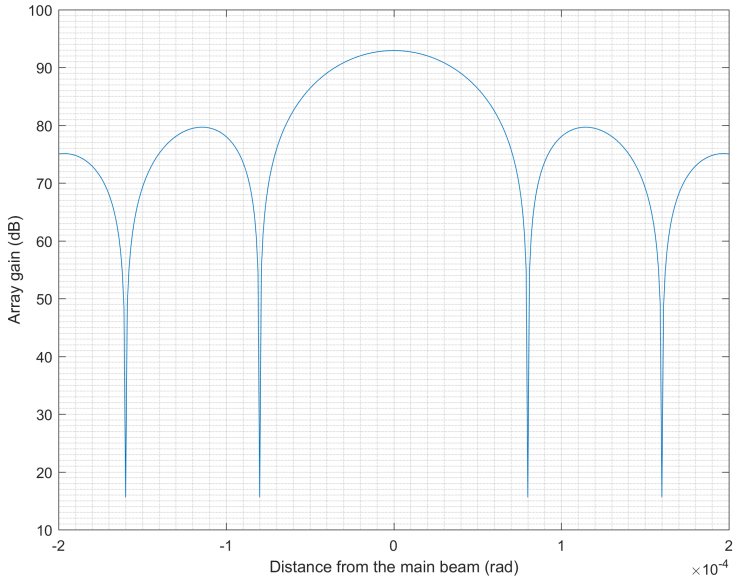

Figure 4.6: *Array gain - zoomed near the main beam for a steering direction of* $\hat{\theta} = 0$

The gain in the main beam direction decreases as the main beam is steered from the zenith as shown in Figure 4.7. The gain is around 93 dB when the main beam is directed towards the zenith. At a co-elevation of 35 degrees, the peak antenna gain is reduced by about 1 dB compared to when the main beam is towards the zenith. At a co-elevation of 70 degrees, the antenna gain drops down to 88.3 dB. This represents an

effective radiated power in this reflector direction of about one third the effective power radiated if the array is steered towards the zenith. This acceptable level of power loss validates the use of the antenna array as a way to direct the radiated power towards the reflector.

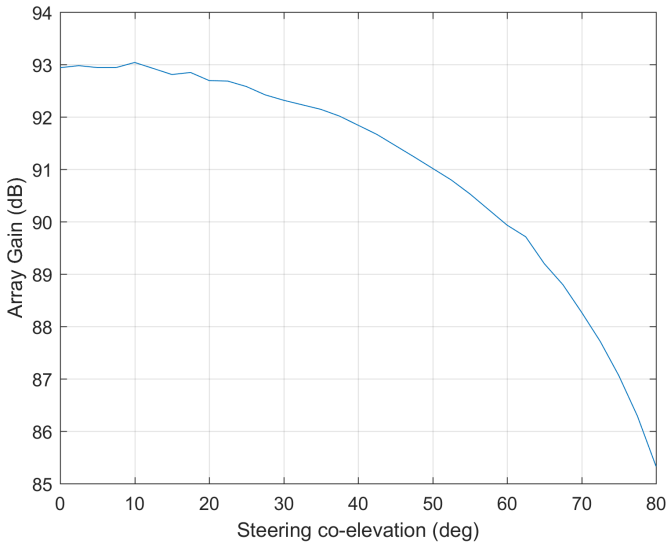

Figure 4.7: *Array gain as a function of steering co-elevation*

Figures 4.8 and 4.9 show the array gain as a function of deviation from the steering direction in the co-elevation and azimuth directions, respectively, for a steering direction of 35 deg co-elevation. The distance between the first nulls are larger in both directions compared to when the main beam is aimed towards the zenith. The first null beam width is 2×10^{-4} radians in the co-elevation direction and 2.8×10^{-4} radians in the azimuth direction.

Figures 4.10 and 4.11 show the array gain as a function of deviation from the steering direction in the co-elevation and azimuth directions, respectively, for a steering direction of 70 deg co-elevation. Unlike the 35 deg case where the first null beam width is larger in both co-elevation and azimuth directions compared to the zenith case, the main beam's increase in width occurs mostly in the co-elevation direction for the 70 deg co-

elevation case. The distance between the first nulls expands to 4.7×10^{-4} radians in the co-elevation direction. The first null beam width is 1.9×10^{-4} radians in the azimuth direction.

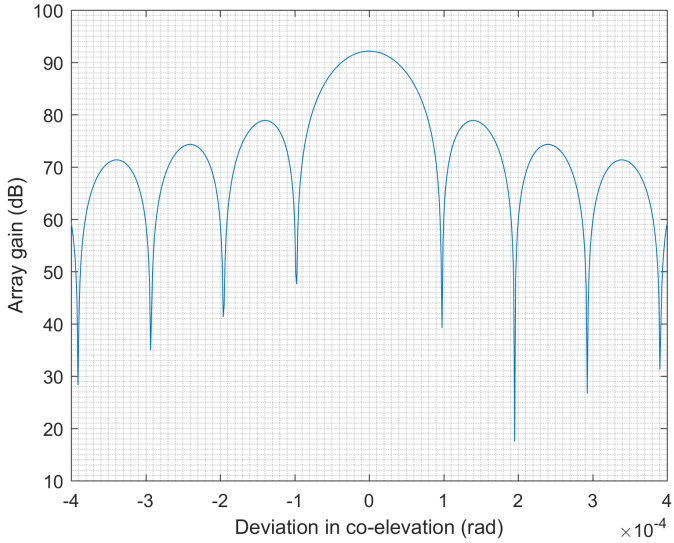

Figure 4.8: *Array gain for deviations in the co-elevation near the main beam for a steering direction of* $\hat{\theta} = 35$ *deg*

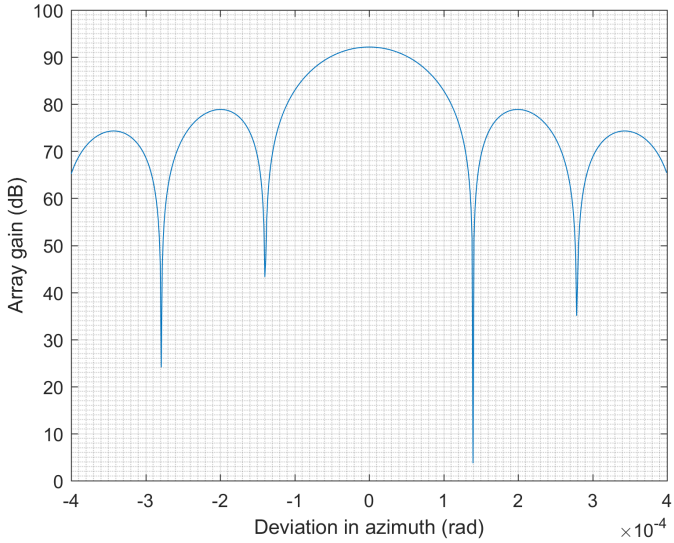

Figure 4.9: *Array gain for deviations in the azimuth near the main beam for a steering direction of* $\hat{\theta} = 35$ *deg*

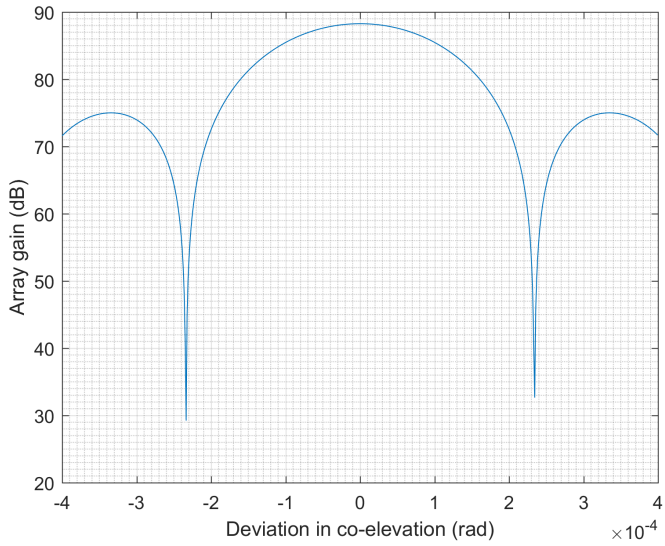

Figure 4.10: *Array gain for deviations in the co-elevation near the main beam for a steering direction of* $\hat{\theta} = 70$ *deg*

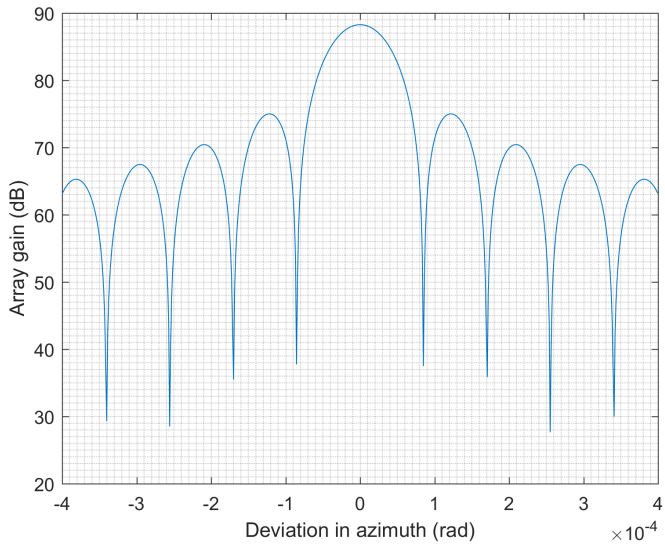

Figure 4.11: *Array gain for deviations in the azimuth near the main beam for a steering direction of* $\hat{\theta} = 70$ *deg*

4.4.3 Received Power Density

Received power density varies as a function of the reflector altitude, reflector radius, the position of the transmitter array relative to the reflector, the transmitter array size, and the receiver location relative to the reflector.

Figure 4.12 shows the power density distribution on the surface of Earth for a reflector altitude of 20200 m, a reflector radius of 20 m, and a transmitter array side length of 1 km. Each receiver location is colored according to its received power density. A colorbar on the right displays the mapping of power density values to the presented colors. The transmitter array is located at a latitude of 0 deg. and longitude of 0 deg. As a result, the reflector lies at the zenith of the antenna array and the gain of the array attains its maximum value. The received power density is largest around the receiver locations that are closest to the reflector, i.e. latitude and longitude of 0 deg. The largest observed power density is -143.2 dBW/m^2. The power density decreases as the receiver location moves away from the reflector as expected. Near the edges of reflector coverage on the ground (latitude of $\pm$52.5 deg., longitude of $\pm$52.5 deg.) the power density attains its lowest value of around -145 dBW/m^2.

For comparison, received power density for GPS ranges from -131 to -133 dBW/m^2 [51]. Due to the lower collecting area of a hemispherical gain pattern patch antenna for a signal with a wavelength of 0.08 m compared to the GPS L1 wavelength of 0.19 m, the power densities on the ground for this wavelength must be 7.53 dB higher than the GPS power densities in order to get the same signal-to-noise ratio in a receiver. Therefore, the GPS-equivalent power density range for the example case discussed above is -151 to -152.5 dBW/m^2. The power density range for this case is significantly below the range needed to give GPS-like carrier-to-noise ratios at the output of hemispherical patch antennas.

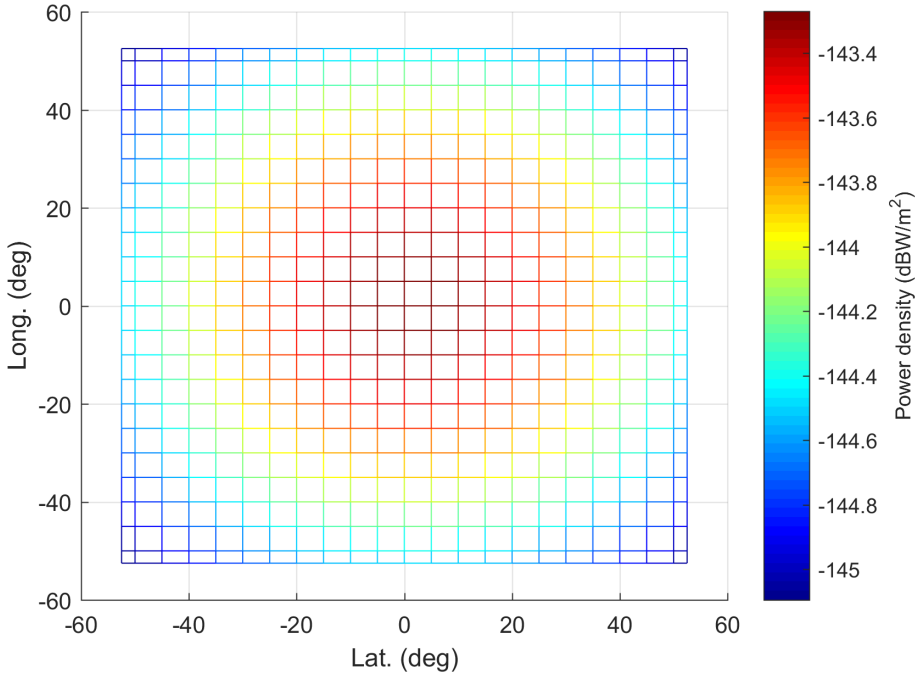

Figure 4.12: *Received power density for an altitude of 20200 km, reflector radius of 20 m, the transmitter array located at a latitude of 0 deg and a longitude of 0 deg, and a 1 km transmitter array size*

The effect of reflector radius on the received power density is straightforward. For a given combination of reflector altitude and transmitter location, the power density at any receiver location is proportional to the reflector radius squared, as determined by Eq. (4.23). Thus, the largest power density results are obtained from the reflector with a radius of 20 m. Going with a larger reflector radius is a straightforward choice if the received power density on ground needs to be increased. Alternatively, one could transmit more power or could increase the size of the transmitter phased array.

Table 4.1 presents the observed power density ranges for various transmitter array locations. The reflector radius is 20 m, and the transmitter array size is 1 km for these results. The first two columns describe the latitude and the longitude of the transmitter array, respectively. The third, fourth, and fifth columns, are, respectively, the range of GPS-equivalent power density values for a reflector altitude of 2000, 10000, and 20200

Transmitter Lat. (deg)	Transmitter Long. (deg)	Range of GPS-equivalent Power Density Values (dBW/m^2) for a reflector radius of 20 m, and a transmitter array size of 1 km		
		2000 km	10000 km	20200 km
0	0	-110.5 to -118	-138.5 to -142	-151 to -152.5
10	10	-115 to -122	-142 to -145	-152 to -154
20	20	-118 to -125	-143 to -146	-153 to -155.5
30	30	-	-144 to -147	-154 to -156
40	40	-	-147 to -150.5	-154 to -156
50	50	-	-	-155 to -157

Table 4.1: Dependence of received power density on the transmitter location and reflector altitude for a signal wavelength of 0.08 m

km, over all the receiver locations. The term "GPS-equivalant" indicates that the actual power densities have been decreased by 7.53 dB before entry into this table in order to make them directly comparable with the typical L1 C/A code GPS power density range of -131 to -133 dBW/m^2. Thus, the column for reflectors at a 2000 km altitude is the only one that can equal or exceed GPS-like carrier-to-noise density ratios. An entry with the symbol - means that this combination of transmitter location and reflector altitude has not been tested because the transmitter array does not have a clear line-of-sight to the reflector with that particular combination. The pattern observed in Figure 4.12 is present in all the transmitter-location/reflector-altitude pairs. The upper and the lower ends of the power density range are observed at a receiver location of (0,0) latitude-longitude pair and a receiver location at the edge of coverage, respectively.

The power density on the ground depends strongly on the reflector altitude. The reflector with the lowest altitude produces the largest power density values. This is expected because the decreased distance between the transmitters and the reflector for the lowest altitude leads to reduced power losses through propagation in space. For each altitude, as the reflector moves away from the zenith, a decrease in power density is observed. This is a combined result of increased distance between the transmitter array

and the reflector, and the reduced antenna gain as the main beam moves away from the zenith. The power density values for the reflector at 2000 km altitude is about 20 and 30 dB larger than the values for the reflector at 10000 km and 20000 km, respectively.

If navigation performance similar to GPS is desired, an altitude of 10000 km has too little power density for a GPS-like carrier-to-noise ratio, about 5.5 to 17.5 dB too little power density. While a LEO altitude results in much higher power density levels, it also leads to a significant reduction in coverage. Conversely, the GPS altitude offers the best coverage among the considered values, but it leads to power density level at least 20 dB below those typical for GPS users. Thus, none of these designs appears to be practical.

The use of a transmitter array with a side length of 4 km may be needed at an altitude of 10000 km. Such an array has a 12 dB gain over the array considered for Table 4.1. This gain of a 4 km array would make the 10000 km altitude case nearly match GPS-like carrier-to-noise ratio performance.

Table 4.2 presents the observed power density ranges for various transmitter array locations. The reflector radius is again 20 m for these results. The wavelength of the signal is set to the GPS L1 carrier wavelength, 0.19 m. The array side length is increased

Transmitter Lat. (deg)	Transmitter Long. (deg)	Range Power Density Values (dBW/m^2) for a reflector radius of 20 m and a transmitter array size of 2.5 km		
		2000 km	10000 km	20200 km
0	0	-102.5 to -110	-130.5 to -134	-143 to -144.5
10	10	-107.5 to -115	-134 to -137	-144 to -146
20	20	-111 to -118	-136 to -139	-145 to -147.5
30	30	-	-137 to -140.4	-146 to -148
40	40	-	-138 to -141	-146.5 to -149
50	50	-	-	-148 to -150

Table 4.2: Dependence of received power density on the transmitter location and reflector altitude for a signal wavelength of 0.19 m.

from 1000 m to 2500 m for this set of simulations in order to keep the number of elements in the array similar to the array used for Table 4.1. A similar column structure to Table 4.1 is used in Table 4.2. The power density ranges for this set are higher due to two effects: a) the lack of an equivalent power loss from a lower collecting area for the receiver antenna and b) maintenance of the gain of the transmitter antenna array for the larger wavelength through an increase of its size. Specifically, the power density ranges observed for an altitude of 10000 km are comparable to the GPS power density range or somewhat below. If the large array size is a concern, a similar power level density range at this altitude can be obtained by decreasing the array size while increasing the transmitter power or the reflector size.

4.4.4 Deviation from Spherical Propagation

The deviation in the modeled phase from that of spherical propagation from a phase center is calculated for all transmitter-location/reflector-altitude pairs according to the analysis associated with Eqs. (4.27-4.29). The set of points at which phase deviations are calculated are the same 5 deg by 5 deg grid points considered for the power density results.

Figure 4.13 shows the results of the phase deviation for an example case. The reflector radius is 20 meters. The transmitter is located at a latitude of 10 deg. and a longitude of 10 deg. The reflector altitude is 10000 km. Each receiver location is colored according to its phase deviation from the best-fit spherical wave front. A colorbar on the right displays the mapping of phase deviation values to the presented colors. The phase deviation ranges from -29 to +8 degrees. This range represents a pseudorange error of significantly less than one carrier wavelength for this case. The optimal fit of

the phase center lies 10.16 meters away from the center of the reflector in the direction of the transmitter. In general, the results show that the calculated phase center is close to the point $R/2$ away from the reflector center in the direction of the transmitter for all tested transmitter-location/reflector-altitude pairs, though the exact distance varies from case to case, up to 2 m, 48 cm, and 18 cm, respectively for altitudes of 2000, 10000, and 20200 km.

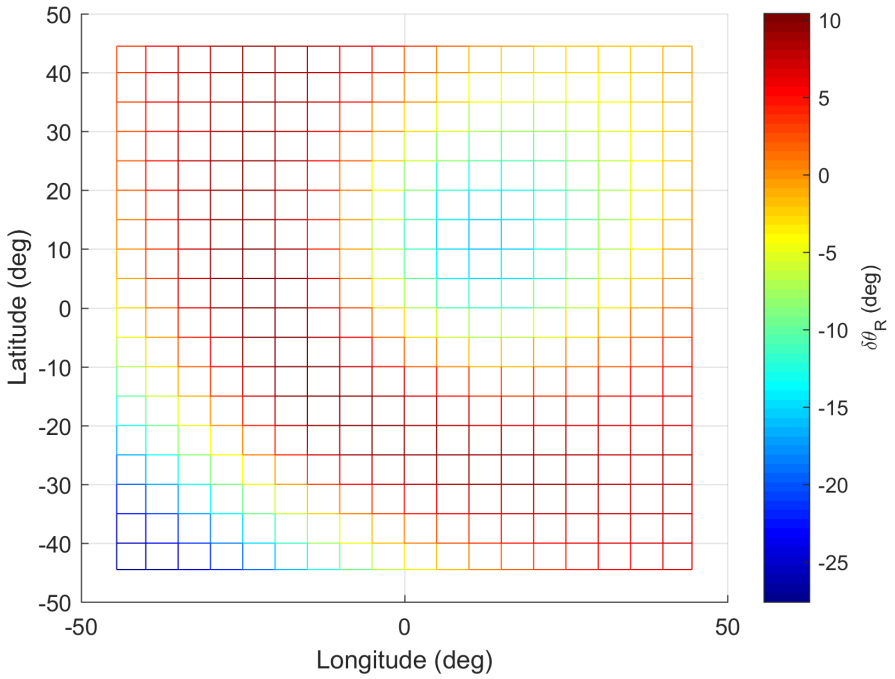

Figure 4.13: *Phase deviation from spherical propagation for an altitude of 10000 km, reflector radius of 20 m, transmitter array size 1 km, and the transmitter array located at a latitude of 10 deg and a longitude of 10 deg*

If the phase center is assumed to be at exactly $R/2$ away from the reflector center in the transmitter direction, a slightly modified form of Eqs. (4.27-4.29) can be used to calculate a new expected phase at each receiver location. This alternate method of determining the phase center fixes $\underline{r}_C$ and solves only for an optimal θ_0. Since θ_0 enters the phase calculations linearly, finding an optimal value for θ_0 is trivial. This alternate optimal value for θ_0 can be used along with the fixed phase center to calculate an alter-

nate value for the phase deviation that are expected to be larger than the original values because of the assumed phase center used.

Figure 4.14 shows the phase deviation results for such calculations for the same example case presented in Figure 4.13. Each receiver location is again colored according to its phase deviation. A colorbar on the right displays the mapping of phase deviation values to the presented colors. The phase deviation range increases to a range of -91 to 25 degrees. As expected, the phase deviation increases as the phase center used in the calculation is changed from a calculated one to an assumed one. Nevertheless, the maximum phase error for this phase center assumption implies a maximum pseudorange error of about one quarter the wavelength, 2 cm.

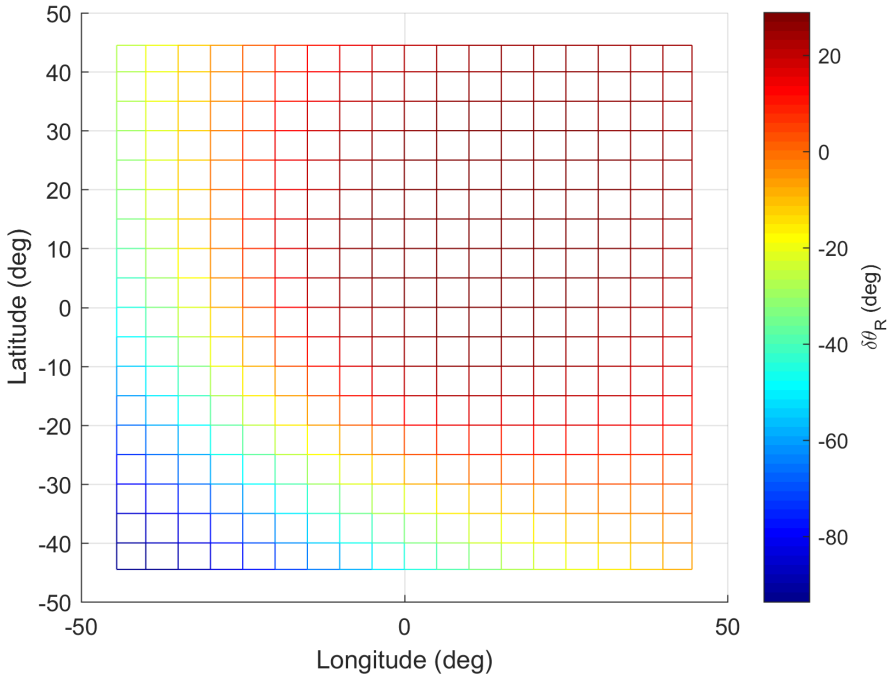

Figure 4.14: *Alternate phase deviation from spherical propagation for an altitude of 10000 km, reflector radius of 20 m, transmitter array size 1 km, and the transmitter array located at a latitude of 10 deg and a longitude of 10 deg*

For a given transmitter-location/reflector-altitude pair, a bigger reflector radius leads to increased phase deviation from spherical propagation. A reflector radius of 10 m

shows the lowest phase errors, and a reflector radius of 20 m present the largest phase errors. This is expected because as the reflector radius decreases, reflection points for various receiver locations move closer on the sphere and a single phase center captures the observed phases more accurately. In the limiting case of a 0-radius reflector, i.e. a point, all reflection points are the same and there is no deviation from a spherical propagation from a single point. Thus, as the radius increases and moves away from this limiting case, observed phase deviation increases.

Figure 4.15 shows the maximum absolute phase deviation and RMS phase deviation as a function of reflector radius for an example case. The considered reflector radii are 10, 15, 20, 30, and 40 m. The transmitter is located at a latitude of 20 deg. and a longitude of 20 deg. The reflector altitude is 10000 km. The maximum absolute deviation over the receiver location grid for each reflector radius is shown by a red x. The RMS phase deviation for each reflector radius calculated over the receiver grid is depicted with a blue star. The red and blue lines represent the best-fit linear curves to the data points. Both the maximum absolute deviation and the RMS deviation show a strong linear dependency on the reflector radius when both the phase center and nominal phase are optimized.

Table 4.3 catalogs the phase deviation results for various transmitter array locations. The reflector radius is 20 m for these results. A similar column structure to Table 4.1 is used. The first two columns describe the latitude and the longitude of the transmitter array, respectively. The third, fourth, and fifth columns, are, respectively, the maximum observed phase deviation for a reflector altitude of 2000, 10000, and 20200 km, over all the receiver locations. The first number in each entry of the third to fifth columns is the calculated maximum phase deviation when the phase center is optimized as described in Eqs. (4.27-4.29). The second number in each entry is the calculated maximum phase

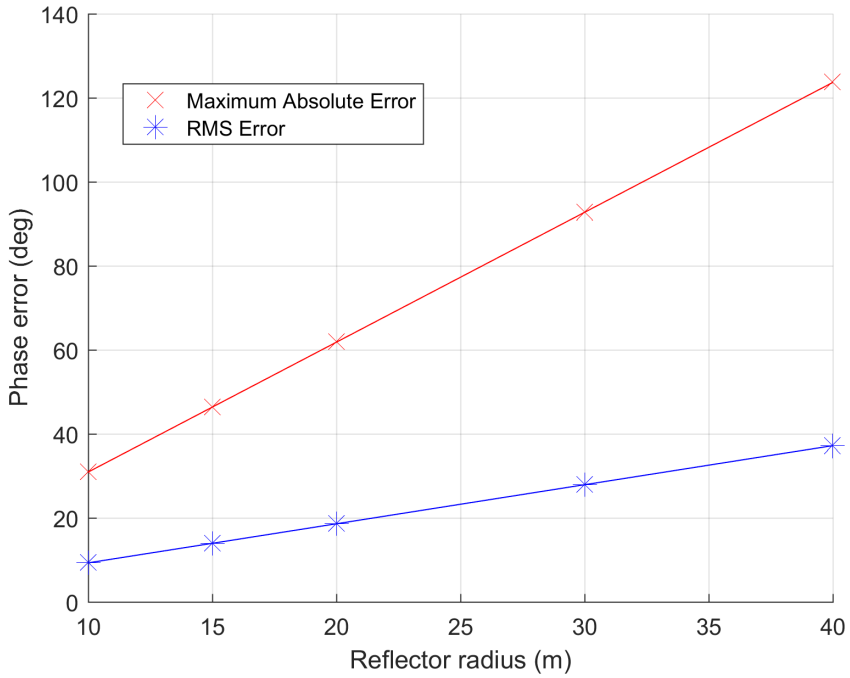

Figure 4.15: *Phase deviation from spherical propagation as a function of reflector radius for an altitude of 10000 km, with the transmitter array located at a latitude of 20 deg and a longitude of 20 deg*

deviation when the phase center is assumed to be exactly $R/2$ away from the reflector center, as described previously in this subsection. Overall, there is an increase in phase deviation as the reflector moves away from the transmitter zenith for all altitudes. The best results are observed for the reflector located at an altitude of 20200 km. At this altitude, the maximum observed phase deviations of 14.2 and 53.9 degrees for the exactly optimized phase and for the assumed $R/2$ phase center, respectively, imply pseudorange errors well below the signal wavelength. Similarly, the observed phase deviations for the reflector at an altitude of 10000 km would result in a maximum pseudorange error of about one wavelength if the phase center is approximated and less if the optimized center is used. For both of these altitudes, the low phase deviation results justify a phase center of $R/2$ away from the reflector center in the transmitter direction as a good approximation.

Transmitter Lat. (deg)	Transmitter Long. (deg)	Maximum phase deviation from spherical propagation (deg) for a reflector radius of 20 m, and a transmitter array size of 1 km		
		2000 km	10000 km	20200 km
0	0	156 / 325	6 / 19	0.9 / 2.6
10	10	1360 / 4300	29 / 91	3.1 / 10.3
20	20	2190 / 7120	62 / 203	6.6 / 22.2
30	30	-	90 / 311	10.2 / 36.0
40	40	-	105 / 379	12.9 / 47.4
50	50	-	-	14.2 / 53.9

Table 4.3: Dependence of phase deviation on the transmitter location and reflector altitude

This approximation fails for the reflector in LEO. The maximum phase deviation values are below one cycle for a reflector at the zenith. As the reflector moves away from the zenith, the maximum phase deviation increases significantly above one cycle. For a transmitter array located such that the reflector is at an elevation of about 75 degrees, given by the third row in this table, a maximum phase deviation of about 20 cycles is observed. Such a phase deviation would translate to a pseudorange error on the order of 1.5 m.

An accurate phase model is required for high precision applications such as CDGPS. Given the large phase deviations observed for the proposed system, one possibility to achieve accurate pseudorange and beat carrier measurements is to broadcast a non-spherical wave-front model that can be used to calculate the phase deviations from a spherical wave-front model. The best form for such a model and how to use such a model in navigation calculations are two topics that are left for future study.

When also considering the power levels observed in the previous subsection for each altitude, an altitude of 10000 km appears to be a good choice if enough transmission power or large enough transmitter or reflector dimensions can be applied so that there will be a sufficient power density on the ground. The large phase deviation observed in

LEO rules it out as a suitable choice. While there is some improvement in this aspect as the altitude moves from 10000 km to 20000 km, the poor power density levels observed at an altitude of 20000 km make it a poor choice, too. Thus, the altitude of 10000 km appears to have acceptable phase deviation values and the possibility of adequate power density levels per this first analysis.

A combination of higher transmitted power, a larger reflector, or a larger phased-array dimension for the transmitter would make a higher altitude workable. Conversely, a lower altitude might be acceptable with a sophisticated wave-front model that accounts for the phase deviations. The exact form of such a wave-front model and whether a pre-calibrated version of it could be created and stored in a receiver are left for future study.

4.5 Summary and Conclusions

This paper has developed and presented a preliminary study on a novel radionavigation system based on ground transmitters and passive orbiting spherical reflectors. The signal utilized by an example version of the system has a wavelength of 8 cm. A rectangular antenna array for the transmitter is designed to achieve high transmitter gain in the direction of reflector. This antenna array achieves a gain of 93 to 88 dB depending on the co-elevation of the reflector.

The simulation results indicate that a reflector altitude of 10000 km with a transmitter power of 50 kW and array dimension of 1 km offers received power density levels 5 to 17 dB weaker than GPS power density levels that yield an equivalent carrier-to-noise density ratio at the output of a hemispherical patch antenna. GPS-like power density levels can be achievable by increasing the transmitter power and the array size. Observed phase deviation values at this altitude seem promising for a spherical propagation as-

sumption. This altitude offers a good trade-off between ground coverage and received power density levels. While a LEO reflector offers improved power density levels, its significantly reduced ground coverage and significantly increased phase deviation from a spherical wave front compared to the 10000-m altitude reflector indicates that it is a more problematic choice for the proposed system.

Calculations show that the phase center can be assumed to be at a point half of the reflector radius away from the reflector center in the direction of the transmitter without causing large pseudorange errors for an altitude of 10000 km.

The results show that decreasing the altitude leads to higher power density levels at the cost of increased phase deviation from a spherical wave front model. Similarly, an increased reflector size increases both the power density and the phase deviation. For any given reflector altitude and reflector size, increasing the array size or the transmitter power is a way to achieve higher power density without causing larger phase deviations.

The results demonstrated by this study reinforce the feasibility of a passive reflector based radionavigation system whose broadcast signal can be altered easily at the ground transmission level. These results merit further study that investigates the pseudorange equation for this system, a navigation solution dependent on such pseudorange equations, reflector constellation design, and more realistic power level calculations.

CHAPTER 5

SUMMARY AND CONCLUSIONS

Three studies have been conducted as part of either providing increased GPS robustness or alternatives to GPS. These studies have been motivated by a perceived need to strengthen the integrity of GPS or to provide a back-up in case GPS is compromised.

The first study of this dissertation has analyzed a new method for Alternative Position, Navigation, and Timing (APNT) for aircraft based on Distance Measuring Equipment (DME) carrier phase. An Extended Kalman Filter that processes time series of DME carrier phases has been developed. Likely filter performance has been assessed through a truth-model simulation. A steady-state accuracy level better than 0.025 nautical miles is achievable with this system. Typical convergence times range from 80 seconds to 900 seconds. The navigation filter uses primarily passive measurements, thereby avoiding the potential for overloading the active two-way ranging function of the existing aircraft navigation DME system. Aircraft altitude has been found to have a minor effect on filter performance. Filter convergence speed and steady-state accuracy have been found to improve with increased aircraft speed. Observed convergence issues in the cases of poor geometric diversity or low aircraft speed can be mitigated with the use of intermittent absolute range measurements. The results suggest potential usefulness of the method as part of an APNT solution for aircraft navigation over CONUS and similar airspaces that have DME networks.

This dissertation's second study has developed a method to estimate multipath with the use of a special antenna array. A maximum likelihood batch estimator that includes a novel iterative search on the number of multipath signals has been developed. The method is also applicable to anti-spoofing systems. The truth-model simulation results have shown successful estimation with up to two multipath signals. Typical direct-signal

direction-of-arrival accuracies have been found to be on the order of 0.4 deg RMS when estimating multipath, but they would be on the order of 10 deg RMS when ignoring multipath by not using this new method. Pseudorange accuracies are on the order of 0.004 chips and 0.1 chips, respectively, when estimating multipath using the new system or when ignoring multipath.

This dissertation's third study has developed a novel radionavigation system based on passive reflector satellites and ground transmitters. A large rectangular phased-array transmission antenna is used in order to achieve high antenna gains for the system, thereby focusing a significant amount of power on the passive reflector satellite, which takes the form of a spherical balloon or similar structure with a radius that might be as large as 20 m.

A reflector altitude of 10000 km and radius of 20 m have been found to offer good power density levels when transmitting an 0.08 m wavelength signal from a 4km-by-4km ground-based phased array at a 50 kwatt power level. Analysis has shown that such a system yields an acceptably small phase deviation from a spherical propagation model. The results have demonstrated the feasibility of this proposed alternative radionavigation system whose broadcast signal can be altered easily at the ground transmitter, thereby providing system robustness through the ability to rapidly adapt the nature of the transmitted signal.

BIBLIOGRAPHY

[1] Peterson, S., "Iran Hijacked US Drone, Says Iranian Engineer", Available from: http://www.csmonitor.com/World/Middle-East/2011/1215/Exclusive-Iran-hijacked-US-drone-says-Iranian-engineer-Video, 2011.

[2] Humphreys, T.E., Ledvina, B.M., Psiaki, M.L., O'Hanlon, B.W., and Kintner, P. M., Jr., "Assessing the Spoofing Threat: Development of a Portable GPS Civilian Spoofer", *Proc. ION GNSS 2008*, Savannah, GA, Sept. 2008, pp. 2314-2325.

[3] Humphreys, T.E., Ledvina, B.M., Psiaki, M.L., O'Hanlon, B.W., and Kintner, P. M., Jr., "Assessing the Spoofing Threat", *GPS World*, Vol. 20, No. 1, January 2009, pp. 28-38.

[4] Shepard, D. P., Bhatti, J. A., and Humphreys, T. E., "Drone hack: Spoofing attack demonstration on a civilian unmanned aerial vehicle," *GPS World*, Vol. 23, Aug. 2012, pp. 30–33.

[5] Narins, M., Enge, P., Peterson, B., Lo, S., Chen, Y.-H., Akos, D., and Lombardi, M., "The Need for a Robust Precise Time and Frequency Alternative to Global Navigation Satellite Systems", *Proc. ION GNSS 2012*, Nashville, TN, Sept. 17-21, 2012, pp. 2057-2062.

[6] Lo, S., Peterson, B., Akos, D., Narins, M., Loh, R., and Enge, P., "Alternative Position Navigation & Timing (APNT) Based on Existing DME and UAT Ground Signals", *Proc. ION GNSS 2011*, Portland, OR, Sept. 19-23, 2011, pp. 3309-3317.

[7] Li, K., and Pelgrum, W., "Flight Test Performance of Enhanced DME (eDME)", *Proc. ION ITM 2012*, Newport Beach, CA, Jan. 30 - Feb. 1, 2012, pp. 131-141.

[8] Li, K., and Pelgrum, W., "Flight Test Evaluation of Enhanced DME (eDME) Performance Enhancements", *Proc. ION GNSS 2012*, Nashville, TN, Sept. 17-21, 2012, pp. 803-811.

[9] Li, K., and Pelgrum, W., "Robust DME Carrier Phase Tracking Under Flight Dynamics", *Proc. ION ITM 2013*, San Diego, CA, Jan. 27-30, 2013, pp. 696-708.

[10] Naab-Levy, A., Li, K., and Pelgrum, W., "DME/N Error Budget Allocation and DME-Next Proof-of-Concept Flight Test and Performance Evaluation", *Proc. ION Pacific PNT 2013*, Honolulu, HI, April 23-25, 2013, pp. 434-450.

[11] Department of Transportation, Federal Aviation Administration, "Concept of Operations for NextGen Alternative Positioning, Navigation, and Timing", FAA, March 1, 2012.

[12] Brown, R. G. and Hwang, P. Y. C., *Introduction to Random Signals and Applied Kalman Filtering*, Wiley, New York, 3rd ed., Nov. 1997, pp. 428-432.

[13] Bar-Shalom, Y., Li, R. X., and Kirubarajan, T., *Estimation with Applications to Tracking and Navigation*, John Wiley & Sons, New York, NY, 2001, pp. 200-217, 303-307, 311-316, pp. 381-394.

[14] Bierman, G. J., *Factorization Methods for Discrete Sequential Estimation*, Academic, New York, NY, 1977, pp. 68-81.

[15] Vig, J.R., "Introduction to Quartz Frequency Standards", Report No. SLCET-TR-92-1, US Army Laboratory Command, Electronics Technology and Devices Laboratory, March 1992.

[16] Harris, M., Murphy, T., Lilley, R. W., and Erikson, R. H., "Performance of Current Distance Measuring Equipment and Implications on Alternative Position Navigation and Timing for Aviation", *Proc. ION GNSS 2012*, Nashville, TN, Sept. 17-21, 2012, pp. 2091-2103.

[17] Van Nee, R.D.J., Siereveld. J., Fenton, P.C., and Townsend, B.R., "The Multipath Estimating Delay Lock Loop Approaching Theoretical Accuracy Limits", *Proc. IEEE Position, Location, and Navigation Symp.*, Las Vegas, Nevada, April 1994.

[18] Sokhandan, N., Curran, J. T., Broumandan, A., and Lachapelle, G., "An advanced GNSS code multipath detection and estimation algorithm", *GPS solutions*, Vol. 20, No. 4, Oct. 2016, pp. 627-640.

[19] Psiaki, M.L., Ertan, T., O'Hanlon, B.W., and Powell, S.P. "GNSS Multipath Mitigation using High-Frequency Antenna Motion", *Navigation*, Vol. 62, No. 1, Spring 2015 , pp. 1-22.

[20] Closas, P., and Fernandez-Prades, C., "A Statistical Multipath Detector for Antenna Array Based GNSS Receivers", *IEEE Transactions on Wireless Communications*, Vol. 10, No. 3, March 2011, pp. 916-929.

[21] Daneshmand, S., Broumandan, A., Sokhandan, N., and Lachapelle, G., "GNSS Multipath Mitigation with a Moving Antenna Array", *IEEE Transactions on Aerospace and Electronic Systems*, Vol. 49, No. 1, Jan. 2013, pp. 693-698.

[22] Chen, X., and Morton, Y., "Iterative subspace alternating projection method for GNSS multipath DOA estimation", *IET Radar, Sonar & Navigation*, Vol. 10, No. 7, Sept. 2016, pp. 1260-1269.

[23] Xu, D., Hu, N., Ye, Z., and Bao, M., "The estimate for DOAs of signals using sparse recovery method", *2012 IEEE International Conference on Acoustics, Speech and Signal Processing (ICASSP)*, Kyoto, 2012, pp. 2573-2576.

[24] Hyder, M. M., and Mahata, K., "Direction-of-Arrival Estimation Using a Mixed $\ell_{2,0}$ Norm Approximation", *IEEE Transactions on Signal Processing*, Vol. 58, No. 9, Sept. 2010, pp. 4646-4655.

[25] Yin, J., and Chen, T., "Direction-of-Arrival Estimation Using a Sparse Representation of Array Covariance Vectors", *IEEE Transactions on Signal Processing*, Vol. 59, No. 9, Sept. 2011, pp. 4489-4493.

[26] Fuchs, J. J., "On the use of the global matched filter for DOA estimation in the presence of correlated waveforms", *2008 42nd Asilomar Conference on Signals, Systems and Computers*, Pacific Grove, CA, 2008, pp. 269-273.

[27] Fuchs, J. J., "On the application of the global matched filter to DOA estimation with uniform circular arrays", *IEEE Transactions on Signal Processing*, Vol. 49, No. 4, April 2001, pp. 702-709.

[28] Antreich, F., Nossek, J.A., and Utschick, W., "Maximum likelihood delay estimation in a navigation receiver for aeronautical applications", *Aerospace Science and Technology*, Vol. 12, No. 3, April 2008, pp. 256-267.

[29] Gill, P.E., Murray, W., and Wright, M.H., *Practical Optimization*, Academic Press, New York, NY, 1981, pp. 133-140.

[30] "Vulnerability assessment of the transportation infrastructure relying on the Global Positioning System", Tech. rep., John A. Volpe National Transportation Systems Center, 2001.

[31] Warner, J. S., and Johnston, R. G., "A simple demonstration that the Global Positioning System (GPS) is vulnerable to spoofing", *The Journal of Security Administration*, Vol. 25, 2002, pp. 19-28.

[32] Kerns, A. J., Shepard, D. P., Bhatti, J. A., and Humphreys, T. E., "Unmanned Aircraft Capture and Control Via GPS Spoofing", *Journal of Field Robotics*, Vol. 31, No. 4, 2014, pp. 617-636.

[33] Bhatti, J. A., and Humphreys, T. E., "Hostile Control of Ships via False GPS Signals: Demonstration and Detection", *Navigation*, Vol. 64, No. 1, Spring 2017, pp. 51-66.

[34] Bauernfeind, R., Kraus, T., Dötterböck, D., Eissfeller, B., Löhnert, E., and Wittmann, E., "Car Jammers: Interference Analysis", *GPS World*, Vol. 22, No. 10, October 2011, pp. 28–35.

[35] Mitch, R.H., Dougherty R.C., Psiaki, M.L., Powell, S.P., O'Hanlon, B.W., Bhatti, J.A., and Humphreys, T.E., "Know Your Enemy: Signal Characteristics of Civil GPS Jammers", *GPS World*, Vol. 23, No. 1, Jan. 2012, pp. 64-71.

[36] Grant, A., Williams, P., Ward, N., and Basket, S., "GPS Jamming and the Impact on Maritime Navigation", *The Journal of Navigation*, Vol. 62, No. 2, 2009, pp. 173-187.

[37] Montgomery, P. Y., Humphreys, T. E., and Ledvina, B. M.,"A multi-antenna defense: Receiver-autonomous GPS spoofing detection", *Inside GNSS*, Vol. 4, No. 2, Mar./Apr. 2009, pp. 40-46.

[38] Lo, S. et al., "Signal authentication: A secure civil GNSS for today", *Inside GNSS*, Vol. 4, No. 5, Sept./Oct. 2009, pp. 30-39.

[39] Psiaki, M. L., et al., "GPS Spoofing Detection via Dual-Receiver Correlation of Military Signals", *IEEE Transactions on Aerospace and Electronic Systems*, Vol. 49, No. 4, 2013, pp. 2250-2267.

[40] White, N.,Maybeck, P., and De Vilbiss, S., "Detection of interference/jamming and spoofing in a DGPS-aided inertial system", *IEEE Transactions on Aerospace and Electronic Systems*, Vol. 34, No. 4, 1998, pp. 1208-1217.

[41] Humphreys, T. E., "Detection Strategy for Cryptographic GNSS Anti-Spoofing", *IEEE Transactions on Aerospace and Electronic Systems*, Vol. 49, No. 2, 2013, pp. 1073-1090.

[42] Butrica, A. J., *Beyond The Ionosphere: Fifty Years of Satellite Communication*, National Aeronautics and Space Administration NASA History Office, Washington, D.C., 1997, Chapter 5.

[43] Hansen, J. R., *Spacecraft Revolution: NASA Langley Research Center From Sputnik to Apollo*, National Aeronautics and Space Administration, 1995, pp. 153-196.

[44] Haupt, R. L., *Antenna Arrays: A computational approach*, John Wiley & Sons, Wiley Online Library, 2010, pp. 55-63.

[45] Haupt, R. L., *Antenna Arrays: A computational approach*, John Wiley & Sons, Wiley Online Library, 2010, pp. 78-82.

[46] Glaeser, G., "Reflections on Spheres and Cylinders of Revolution", *Journal for Geometry and Graphics*, Vol. 3, No. 2, 1999, pp. 121-139.

[47] Kuenzer, C., Dech, S., and Wagner, W., *Remote Sensing Time Series: Revealing Land Surface Dynamics*, Cham: Springer International Publishing, 2015, pp. 236-237.

[48] Osipov, A. V., and Tretyakov, S.A., *Modern Electromagnetic Scattering Theory with Applications*, John Wiley & Sons, Wiley Online Library, 2017, pp. 481-483.

[49] Osipov, A. V., and Tretyakov, S.A., *Modern Electromagnetic Scattering Theory with Applications*, John Wiley & Sons, Wiley Online Library, 2017, pp. 101, 464, 481.

[50] General Dynamics Mission Systems, "A Look Inside Space Fence's 7,000 Square-Foot Radar Array", Available from: https://gdmissionsystems.com/Articles/2017/05/02/in-the-news-5-2017-a-look-inside-space-fences-radar-array-structure, 2017.

[51] Misra, P., and Enge, P., *Global Positioning System: Signals, Measurements, and Performance*, Ganga-Jamuna Press, Lincoln, Massachusetts, 2011, pp. 393-394.